Journal of Materials Chemistry A

ROYAL SOCIETY OF CHEMISTRY

REVIEW

View Article Online
View Journal | View Issue

Cite this: J. Mater. Chem. A, 2023, 11, 8599

Graphitic carbon nitride (g-C_3N_4) based heterogeneous single atom catalysts: synthesis, characterisation and catalytic applications

Suja P,[ac] Jubi John,[bc] T. P. D. Rajan,[ac] Gopinathan M Anilkumar,[d] Takeo Yamaguchi,[d] Suresh C. Pillai[e] and U. S. Hareesh*[ac]

Received 15th December 2022
Accepted 17th March 2023

DOI: 10.1039/d2ta09776a

rsc.li/materials-a

Graphitic carbon nitride (g-C_3N_4), the well-known visible light active, two-dimensional organic semiconductor is gaining further prominence as a potential matrix for developing heterogeneous single atom catalysts. g-C_3N_4 by virtue of its abundant and periodically separated nitrogen atoms effectively stabilises single atoms of metal through the electron lone pairs of nitrogen acting as anchoring sites. Herein, the synthetic strategies adopted for the development of g-C_3N_4 based single atom catalysts (SACs) are summarised in detail for an understanding of the state-of-the-art designing of g-C_3N_4 SACs. Advanced characterisation techniques like extended X-ray absorption fine structure (EXAFS), X-ray absorption near-edge structure (XANES), electron energy-loss spectroscopy (EELS), X-ray photoelectron spectroscopy, and aberration-corrected high-angle annular dark-field scanning transmission electron microscopy (HAADF-STEM) offer valuable inputs to determine the electronic and geometric structure of g-C_3N_4 based SACs are discussed. Furthermore, the experimental and computational efforts carried out in demonstrating the potential applications of g-C_3N_4 SACs in the field of photocatalysis, organic reaction catalysis and electrocatalysis are reviewed. The challenges associated with the practical utility of g-C_3N_4 based SACs and their future perspectives in heterogeneous catalysis are outlined.

[a]Materials Science and Technology Division, CSIR-National Institute for Interdisciplinary Science and Technology, Thiruvananthapuram-695019, India. E-mail: hareesh@niist.res.in

[b]Chemicals Science and Technology Division, CSIR-National Institute for Interdisciplinary Science and Technology, Thiruvananthapuram-695019, India

[c]Academy of Scientific and Innovative Research (AcSIR), Ghaziabad-201002, India

[d]Laboratory for Chemistry and Life Sciences, Tokyo Institute of Technology, R1-17, 4259 Nagatsuta, Midori-Ku, Yokohama, 226-8503, Japan

[e]Nanotechnology and Bio-Engineering Research Group and Health and Bio-Medical Research Centre (HEAL), Atlantic Technological University, ATU Sligo, Ash Lane, Sligo, F91 YW50, Sligo, Ireland

Suja P is currently a UGC-Senior Research Fellow at CSIR-National Institute for Interdisciplinary Science and Technology (CSIR-NIIST), Thiruvananthapuram. She received her B.Sc. in Chemistry from NSS college, Ottapalam and M.Sc. in Chemistry from Sri Vyasa NSS College, Wadakkancherry. She is currently pursuing her doctoral research on the design and development of g-C_3N_4 based single atom catalysts and semiconductor heterostructures for photocatalytic applications and for organic reaction catalysis. She has authored 2 patents, 1 research article, and 1 book chapter.

Dr Jubi John obtained his PhD in synthetic organic chemistry from CSIR-NIIST under the supervision of Dr K. V. Radhakrishnan. Soon after he joined as a CEA-Eurotalents postdoctoral fellow with Dr Eric Doris at CEA Saclay, France. In 2011, he joined as an Alexander von Humboldt fellow with Prof. Henning Hopf at TU Braunschweig, Germany and from 2013, with Prof. Wim Dehaen at the KU Leuven, Belgium. He then joined CSIR-NIIST in 2015 and is presently working as a senior scientist at the same institute. His research interests include development of novel synthetic methodologies, homogenous and heterogeneous catalyzed organic transformations and new antiviral drug candidates.

1 Introduction

Heterogeneous catalysts comprising metal nanoparticles on supports are widely employed for accelerating the kinetics of industrially important reactions. Nevertheless, the full potential of such systems is hitherto unexploited as the atoms exposed only on the metal nanoparticle surface are active and the atomic utilisation of metal is low. Moreover, the predominant use of precious metals like Pt, Rh imparts exorbitant costs for heterogeneous catalysts. Single Atom Catalysts (SACs) or Atomically Dispersed Metal Catalysts (ADMCs) refer to an incipient class of materials where active centers of metals are individually dispersed on appropriate support through coordination with atoms like nitrogen, oxygen, sulphur, *etc.* The partial positive charges on metal sites due to decreased electron density offer modified interactions thereby enhancing the rate of conversion of substrate into product. Furthermore, metal atoms in SACs/ADMCs are spatially isolated to influence the adsorption characteristics of reactive intermediates, thereby preventing the unwanted side reactions that proceed through adjacent metal sites. The development of SACs and ADMCs provides the most ideal strategy for creating catalysts that are

Dr T. P. D. Rajan is currently a Senior Principal Scientist in Materials Science and Technology Division of CSIR – National Institute for Interdisciplinary Science and Technology (NIIST), Thiruvananthapuram. He obtained B.Sc. and M.Sc. in Chemistry, M.Tech. in Metallurgy from NITK, Surathkal and PhD in Metallurgical Engineering from CSIR-NIIST. His research interests are composite materials, light metals, surface technology and nanomaterials. He had published 146 research papers, 10 book chapters and filed 3 patents. He is recipient of Award for Excellence in Corrosion Science and Technology (NACE), IIM Nalco Gold Medal, IIF Industrial Research Award, INAE Innovation Award and IIM Metallography Awards.

Dr Gopinathan M Anilkumar is currently a visiting professor at the Institute of Innovative Research (IIR), Tokyo Institute of Technology, Japan. He is employed as a senior research manager at the R&D Center of Noritake Co., Ltd., Aichi, Japan. Dr Anilkumar obtained his PhD in Chemistry from Mahatma Gandhi University, Kerala for the work carried out at CSIR-NIIST, India. He was a post-doctoral researcher at the Korea Advanced Institute of Science and Technology (KAIST), Korea (S), and the University of Tokyo, Japan. He is currently engaged in the development of advanced materials for fuel cells and water electrolyzers. He has authored more than 70 peer-reviewed research papers and holds 25 granted patents.

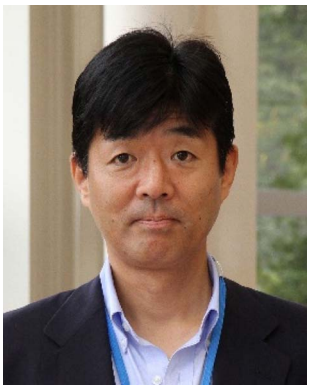

Prof. Takeo Yamaguchi is a Professor at the Laboratory for Chemistry and Life Sciences, Institute of Innovative Research (IIR), Tokyo Institute of Technology, Japan. He also serves as the Director of the Tokyo Tech Academy for Convergence of Materials and Informatics (TAC-MI). Prof. Yamaguchi received his Doctor of Engineering degree from the Department of Chemical Engineering, The University of Tokyo, followed by post-doctoral research at the University of Colorado at Boulder, USA. He also holds several positions in various scientific societies, such as Vice President of the membrane society of Japan, Council member of the Aseanian Membrane Society (AMS), and a steering committee member of the World Association of Membrane Societies. He has authored more than 230 publications and holds more than 30 granted patents. His research interests include the systematic design of energy materials and systems for fuel cells and water electrolysis, stimuli-responsive membranes inspired by biosystems, and the utilization of computational techniques for the efficient design of materials.

Suresh C. Pillai obtained his PhD from Trinity College Dublin and completed his postdoctoral research at California Institute of Technology (Caltech, USA). He currently heads the Nanotechnology and Bio-Engineering Research Group at the Institute of Technology Sligo, Ireland. His research interests include the synthesis of nanomaterials for energy and environmental applications. He is the recipient of several awards including the Boyle-Higgins Award 2019, Linus-Pauling Lecture Award 2020 etc. Suresh is also a recipient of the 'Industrial Technologies Award 2011' for licensing functional coatings to Irish companies. He was also the recipient of the 'Hothouse Commercialisation Award 2009' from the Minister of Science, Technology and Innovation and also the recipient of the 'Enterprise Ireland Research Commercialization Award 2009'. He has also been nominated for the 'One to Watch' award 2009 for commercialising R&D work (Enterprise Ireland).

cost-effective for a multitude of applications including photocatalysis, electrocatalysis and organic transformations.

One of the essential requirements for realisation of SACs is the effectiveness of coordination of metal centers with matrix/support atoms. The free energy of metal increases as it tends to manifest itself in the finest form and a strong coordination with support atoms is imperative to counter aggregation tendencies. In this context, 2D materials owing to their surface area and weak van der Waals forces possess significant advantages, to be employed as the matrices for SACs and ADMCs. Consequently, a host of supports like N-doped carbon, graphene, and high surface area metal oxides are explored. More recently, 2D layered g-C_3N_4, an organic semiconductor was established as an effective candidate for visible-light induced photocatalysis by virtue of its band gap of 2.7 eV. g-C_3N_4 is constructed of layered hexagonal building blocks of tri-*s*-triazine units and forms sheet-like pi conjugated structures composed of sp^2 C and sp^2 N.[1]

The abundant nitrogen atoms in g-C_3N_4 facilitate the anchoring of single metal atoms through the effective coordination between empty (or partially empty) orbitals of metal atoms with the electron lone pairs of nitrogen. g-C_3N_4 has thus been demonstrated to be an excellent host for the development of SACs, despite its below average surface area. Atomic level dispersion of metal species over g-C_3N_4 results in the development of 6 major varieties of catalyst systems (Fig. 1) depending upon the metal distribution and loading. The conventional terminology of g-C_3N_4 based single atom catalysts (SACs) refers to the ideal condition of uniformly dispersed, individual, isolated metal atoms coordinated to g-C_3N_4 matrix. In g-C_3N_4 based atomically dispersed metal catalysts (ADMCs), metal atoms are dispersed in the form of clusters containing dimers, trimers, *etc* along with isolated single metal atoms. More recently g-C_3N_4 based dual metal single atom catalysts emerged where two different metals are coordinated to the matrix as single atoms (DM-SACs). Ultra-high density single atom catalysts (UHD-SACs) refer to the atomic level dispersion of metal atoms at very high metal loading (>20 wt%) and with ultrahigh atom density (5–15 atoms nm^{-2} at a spacing of 0.2–0.5 nm).[2] Depending upon the positioning of single atoms on g-C_3N_4 matrix two more classifications are reported. In edge confined single atom catalysts (EC-SACs) the metal atoms are preferentially located at the edges of g-C_3N_4 sheets through unsaturated vacancies along the edges. On the other hand, in interlayer coordinated SACs (ILC-SACs), confinement of the single atoms occurs in between the layers of g-C_3N_4 through coordination with appropriate functional groups.

The chronology of developments leading to the establishment of SACs based on g-C_3N_4 is provided in the timeline below (Fig. 2).

In this review, we attempt to comprehensively analyse the developments based on g-C_3N_4 supported single atom catalysts (SACs) and cover its applications in the areas of photo, electro and thermal catalysis. A tutorial like description of the fundamental aspects related to the synthesis and characterisation of g-C_3N_4 SACs is included. DFT studies in the reported works are also incorporated primarily to throw light on the prospective experimental works that can be pursued. To the best of our knowledge, this review is the first attempt to cover all the applications thus far explored on g-C_3N_4 SACs.

Dr U. S. Hareesh is currently a Senior Principal Scientist at the Materials Science and Technology division of CSIR-National Institute for Interdisciplinary Science and Technology (CSIR-NIIST), Thiruvananthapuram. He obtained his PhD in Chemistry from Mahatma Gandhi University, Kerala for the work carried at CSIR-NIIST, India and Technical University of Hamburg-Harburg (TUHH), Germany. Subsequently, he worked as a visiting scientist at the Institute for New Materials, Saarbruecken, Germany and as a scientist at the Centre for Ceramic Processing, Advanced Research Centre International (ARCI), Hyderabad, India. He is currently engaged in the development of advanced functional materials for energy and environmental applications. He has authored more than 90 publications in peer reviewed journals, 10 granted patents and 5 book chapters. He is the recipient of the German Academic Exchange Service (DAAD) fellowship, Malaviya award of the Indian Ceramic Society and Technology award of ARCI, Hyderabad.

2 Graphitic carbon nitride as support for SACs

g-C_3N_4 consists of *s*-triazine or tri-*s*-triazine rings as the basic constituent units that offer uniformly placed, abundant nitrogen atoms to confine single metal atoms effectively and with high loading. The terminal tri-*s*-triazine unit of g-C_3N_4 comprises different types of nitrogen[12] as presented schematically in Fig. 3. The various N-species in g-C_3N_4 are demonstrated to be very effective for catalytic reactions as they impart H-bonding, tunable basicity, Lewis acidity. Strong metal–support interaction is essential to stabilise the well-dispersed metal species as isolated single metal atoms for imparting selectivity and catalytic activity. This will also prevent the diffusion and aggregation of single atoms at the time of synthesis as well as during the utilisation of SACs at various reaction conditions. This is primarily facilitated by the substantially greater surface energy of metal single atoms compared to their nanoclusters and nanoparticles.[13]

Synthesis of g-C_3N_4 is carried out by thermal decomposition and polymerisation of N-rich precursors like melamine, cyanamide, dicyandiamide, urea, thiourea and their mixtures at 550 °C in air,[14] as shown schematically in Fig. 4. The bulk material formed at 550 °C is similar irrespective of the atmosphere of firing but may differ in the degree of condensation and product yield. Generally, all the precursors first condense to melamine at 235 °C followed by a self-condensation leading to the formation

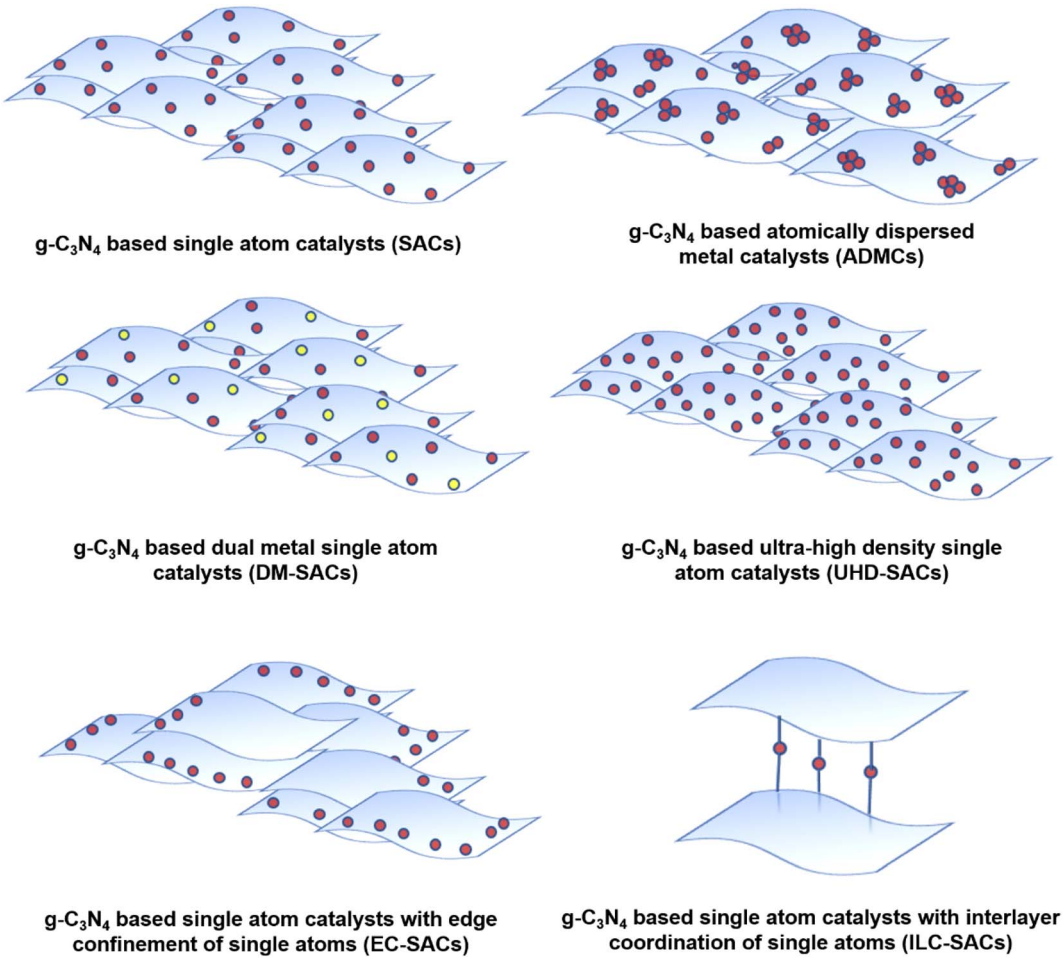

Fig. 1 Various configurations of metal atom dispersions over g-C_3N_4 matrix.

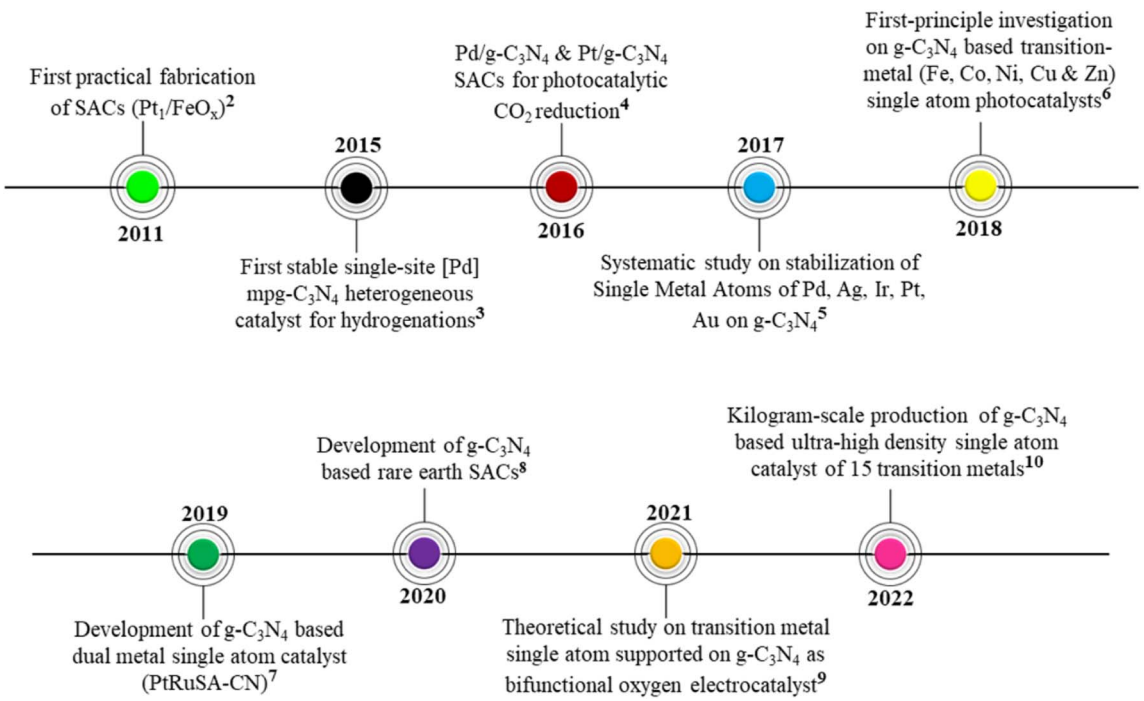

Fig. 2 Timeline representing the chronology of advancements in SACs based on g-C_3N_4.[3–11]

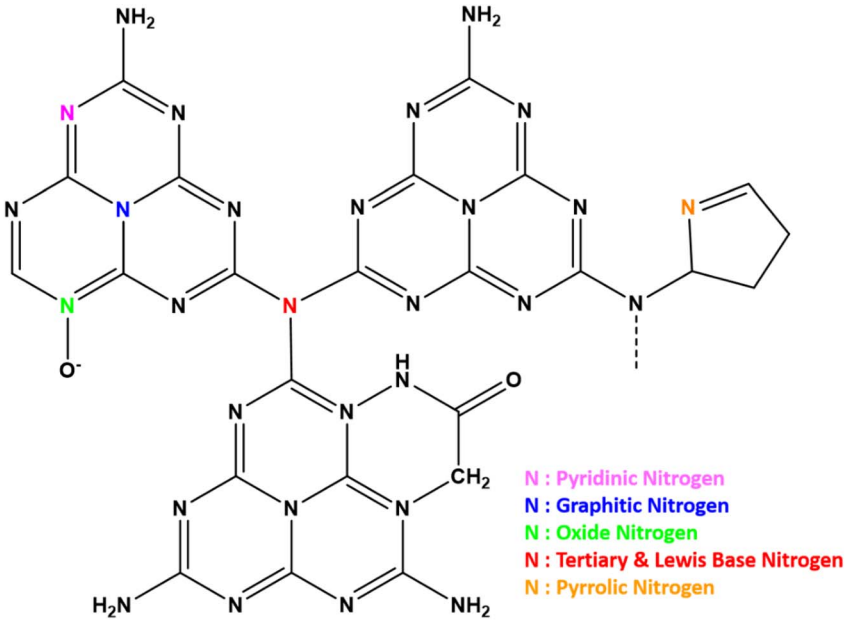

Fig. 3 Types of nitrogen functionalities possible in g-C_3N_4.

of a dimer called melam (N2-(4,6-diamino-1,3,5-triazin-2-yl)-1,3,5-triazine-2,4,6-triamine). Essentially melamine (triazine) based structures are formed up to a temperature of 350 °C. At 390 °C melam units are converted into tri-*s*-triazine units called melem by the rearrangement of melamine. Finally, the networked polymeric g-C_3N_4 is formed by the successive condensation of melem units at 520 °C. The material is unstable above 600 °C and complete decomposition to volatile components

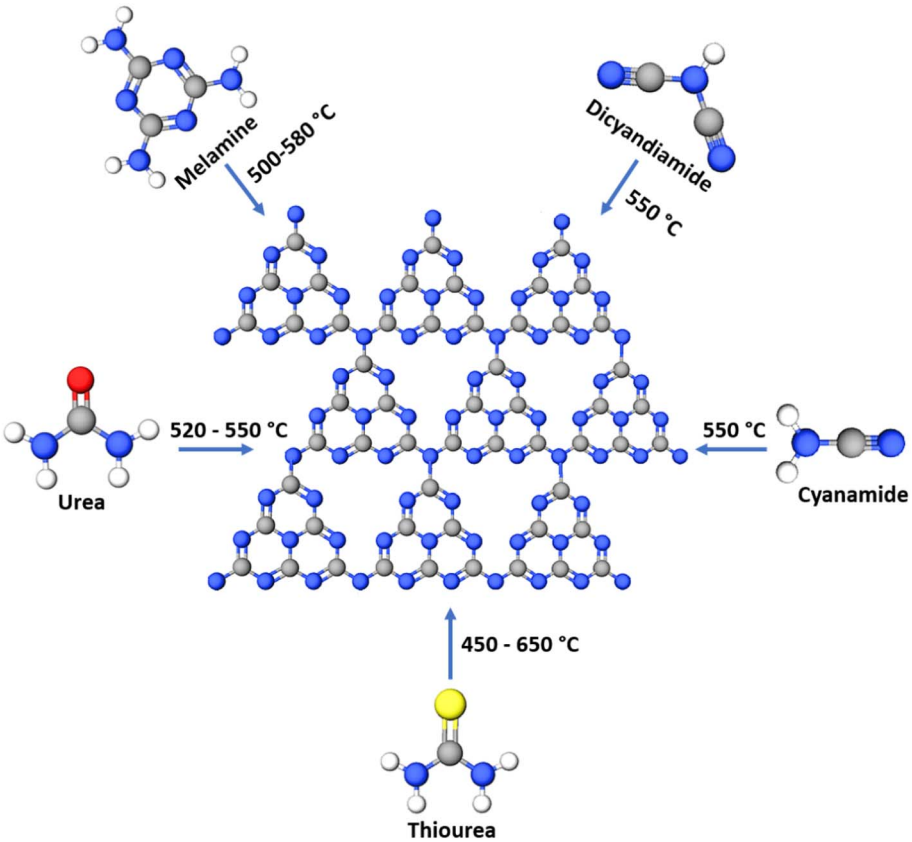

Fig. 4 Synthesis of g-C_3N_4 from various nitrogen abundant precursors.

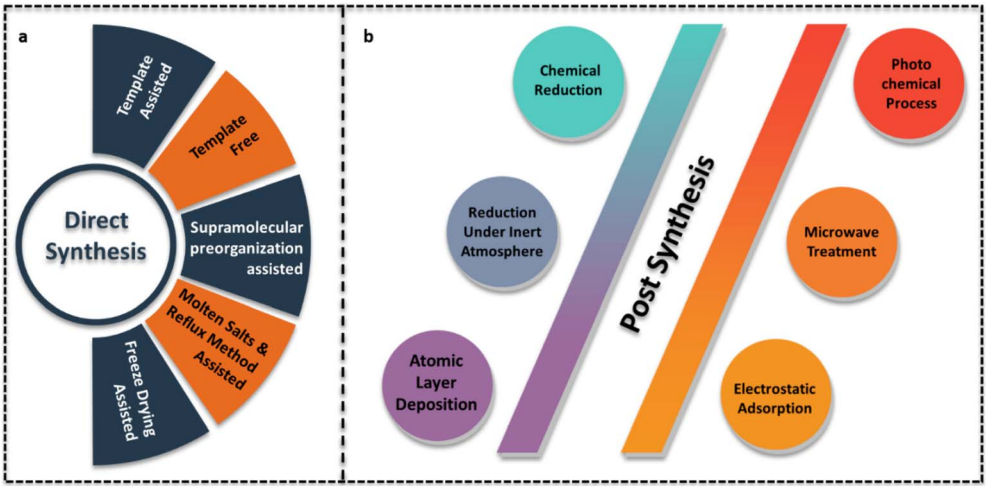

Fig. 5 Various strategies employed during (a) direct and (b) post synthesis of g-C_3N_4 SACs.

occurs at temperatures >700 °C in air.[15] Template assisted thermal polymerisation of g-C_3N_4 precursors results in the formation of mesoporous polymeric g-C_3N_4 (mpg-C_3N_4) with enhanced surface area. Thermal exfoliation of bulk g-C_3N_4 (BCN) leads to the formation of g-C_3N_4 nanosheets/exfoliated g-C_3N_4 (ECN) with improved surface area. All the 3 forms of g-C_3N_4 *i.e.*, BCN, mpg-C_3N_4, ECN can perform as a support for SACs.

3 Synthesis of g-C_3N_4 based single atom catalysts

Pérez-Ramírez *et al.* proposed direct and post-synthesis approaches for g-C_3N_4 based SACs. Direct synthesis involving the pyrolysis of the g-C_3N_4 precursors with metal salts is a bottom-up approach. During the polymerisation of g-C_3N_4 from precursors, single metal atoms are anchored on to the g-C_3N_4 support. Post synthesis is a strategy employed to disperse single atoms on synthesised g-C_3N_4 types like bulk g-C_3N_4, mpg-C_3N_4, ECN, *etc* which are prepared either through template free or template assisted synthesis strategy.[6] Fig. 5 depicts the multiple approaches involved in both the above categories for the preparation of g-C_3N_4 SACs.

3.1 Direct synthesis

3.1.1 Template free direct synthesis. Template free direct synthesis involves the pyrolysis of the mixture containing g-C_3N_4 precursor and a corresponding metal salt. Dong *et al.* demonstrated the synthesis of rare-earth La single-atoms dispersed

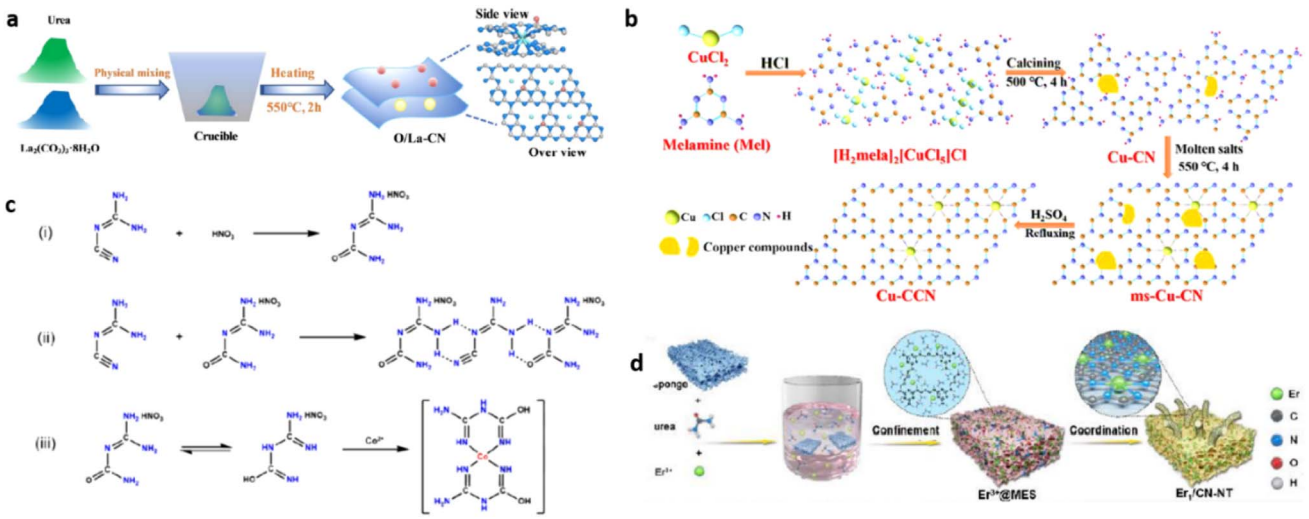

Fig. 6 (a) Template free direct synthesis of La single-atoms dispersed carbon nitride (O/La–CN). Reproduced with permission from ref. 16. Copyright 2020 American Chemical Society. (b) Direct synthesis of single Cu atoms supported crystalline g-C_3N_4 (Cu–CCN) through molten salts-reflux method. Reproduced with permission from ref. 18. Copyright 2020 American Chemical Society. (c) Mechanism of supramolecular preorganisation of g-C_3N_4 based cobalt SAC. Reproduced with permission from ref. 19. Copyright 2020 Elsevier. (d) Freeze drying assisted direct synthesis of erbium single atoms decorated g-C_3N_4 (Er_1/CN-NT). Reproduced with permission from ref. 9. Copyright 2020 John Wiley and Sons.

carbon nitride (O/La–CN) by the one-step calcination of $La_2(CO_3)_3$ and urea at 550 °C resulting in amorphous g-C_3N_4 with homogeneously dispersed La single atoms (Fig. 6(a)).[16]

3.1.2 Template assisted direct synthesis. Template assisted direct synthesis involves the pyrolysis of g-C_3N_4 precursor with metal salt in the presence of templates like silica, SBA-15, *etc.* to arrive at mpg-C_3N_4 as the support for single atoms. Dontsova *et al.* demonstrated the synthesis of single atom silver dispersed mpg-C_3N_4 (AgTCM-mpg-CN) through the pyrolysis of the precursor mix containing cyanamide and silver tricyanomethanide (AgTCM) in the presence of SiO_2 nanoparticles as the template leading to AgTCM-mpg-CN with enhanced surface area. The use of AgTCM as a reactive co-monomer facilitated silver doping as negative charges are introduced into the C_3N_4 framework which provided strong binding sites for Ag single atoms. The template assisted direct synthesis required the removal of the SiO_2 template using NH_4HF_2.[17]

3.1.3 Molten salts and reflux method assisted direct synthesis. Xiang *et al.* demonstrated the preparation of single Cu atoms dispersed over crystalline g-C_3N_4 through molten salt and reflux method assisted direct synthesis (Fig. 6(b)). Cu atoms are incorporated into the framework of melamine by mixing melamine and $CuCl_2$ in the presence of HCl forming $[H_2\text{-mela}]_2[CuCl_5]Cl$ (where 'mela' is depicted as melamine) comprising of negatively charged layers of $[CuCl_5]_n^{3n-}Cl^-$ ions are then removed from $[H_2mela]_2[CuCl_5]Cl$ during the second step of the synthetic procedure. Subsequent polymerisation of melamine formed g-C_3N_4 with heptazine basic units which on molten salt treatment with KCl and LiCl followed by sulphuric acid leaching led to the formation of crystalline g-C_3N_4 with atomically dispersed Cu atoms.[18]

3.1.4 Supramolecular preorganisation assisted direct synthesis. Chen *et al.* synthesised g-C_3N_4 with atomically dispersed cobalt through supramolecular preorganisation followed by calcination. The reaction of dicyandiamide with nitric acid led to the formation of dicyandiamidine nitrate precursor which self-assembled intermolecularly with dicyandiamide resulting in the formation of a crimped supramolecular precursor. The thermal treatment of supramolecular precursor together with cobalt chloride led to the formation of g-C_3N_4 matrix embedded with atomically dispersed Co species (Fig. 6(c)).[19]

3.1.5 Freeze drying assisted direct synthesis. Freeze drying assisted direct synthesis facilitates atom confinement and coordination (ACC) (Fig. 6(d)). Wang *et al.* employed this ACC strategy to synthesise high density rare-earth single-atom Er catalyst using g-C_3N_4 support. Melamine sponge soaked in an aqueous solution containing erbium salt ($Er(NO_3)_3\cdot 5H_2O$) and urea is frozen by liquid N_2 for an evenly distributed concentration of the precursors. The complete moisture removal from the frozen sponge is ensured by freeze drying, and the sample is annealed under N_2 to form erbium single atoms decorated g-C_3N_4 with tubular morphology (Er_1/CN-NT). The nitrogen atoms present in melamine sponge and urea enable the coordination of erbium atoms and the employment of ultralow temperatures of liquid N_2 and freeze drying facilitates the atomic confinement of Er forming the formation of low- and high-density Er_1/CN-NT.[9]

3.2 Post synthesis

Use of template like silica, SBA-15, *etc* during the pyrolysis of g-C_3N_4 precursors, forms mpg-C_3N_4 with enhanced surface area. Exfoliated g-C_3N_4 is obtained through thermal or chemical exfoliation. Post synthesis strategy involves the mixing of metal salts in g-C_3N_4 dispersion and its conversion to single metal atoms using techniques like chemical reduction, reduction under an inert atmosphere, photochemical reduction, microwave treatment, electrostatic adsorption, and atomic layer deposition (ALD).

3.2.1 Chemical reduction. Chemical reduction involves the usage of chemical reducing agents such as $NaBH_4$ for the deposition of metal as single atom. Pérez-Ramírez *et al.* demonstrated this post synthetic strategy for the incorporation of single metal atoms of Pt, Ir, and Pd on g-C_3N_4 of varying morphologies (Bulk g-C_3N_4, mpg-C_3N_4, ECN). A sequential wet deposition/wet impregnation–chemical reduction approach ($NaBH_4$) employing metal salts of Pd/Pt/Ir ($PdCl_2$, $H_2PtCl_6\cdot xH_2O$, $K_2IrCl_6\cdot 6H_2O$) yielded g-C_3N_4 SACs with a metal loading of 0.5 wt%.[6]

3.2.2 Microwave treatment. Li *et al.* showed the formation of single Co single atoms on mpg-C_3N_4 by microwave assisted thermal treatment of a precursor mix containing $CoCl_2$, g-C_3N_4, triethylamine (TEA). TEA enhanced the deposition of Co^{2+} with the increase of $CoCl_2$ content and cobalt loading up to 0.430 μmol mg^{-1} of mpg-C_3N_4 was achieved. However, a cobalt content of 0.016 μmol mg^{-1} was only achieved without TEA despite the use of large excess of $CoCl_2$.[20]

Similarly, Zbořil and co-workers successfully employed microwave heating assisted post synthesis strategy for the development of ruthenium single atom dispersed mesoporous g-C_3N_4 catalyst (Fig. 7(a)).[21]

3.2.3 Electrostatic adsorption. Liu *et al.* developed Au_1N_x/C_3N_4 SACs through the post synthesis strategy involving electrostatic adsorption (Fig. 7(b)). g-C_3N_4 derived from urea precursor is treated with ammonia solution to develop surface positive charges, which on subsequent reaction with $HAuCl_4$ forms Au_1N_x single-sites over g-C_3N_4.[22] In a similar approach, single atom Pt^{II}–C_3N_4 catalyst was also developed by the same group.[23]

3.2.4 Atomic layer deposition (ALD). ALD is also employed as a post synthetic strategy to develop g-C_3N_4 SACs. Yao *et al.* deposited Co single atoms over surface functionalised g-C_3N_4. Prior to Co ALD, phosphorous doping (phosphidation) using sodium hypophosphite as the non-metal, alters the surface functionalities as well as porous structure of the g-C_3N_4 matrix *via* CoP_4 center formation. ALD using cobalt bis(cyclopentadienyl) followed by O_3 treatment led to the formation of a single Co_1–N_4 site over the matrix with a cobalt loading of 1 wt%.[24]

3.2.5 Photochemical reduction. Guo *et al.* synthesised Pt single atoms on N-deficient g-C_3N_4 employing a photochemical process involving the mixing of H_2PtCl_6 with an aqueous dispersion of g-C_3N_4. Freezing under liquid N_2 temperature followed by photochemical reduction with UV light resulted in the formation of single atom Pt decorated nitrogen deficient g-C_3N_4. On the contrary, g-C_3N_4 loaded with Pt nanoparticles was formed when the reduction was conducted without liquid N_2 assisted freezing.[25]

3.2.6 Reduction under an inert atmosphere. Chen *et al.* successfully demonstrated the development of single atom Au

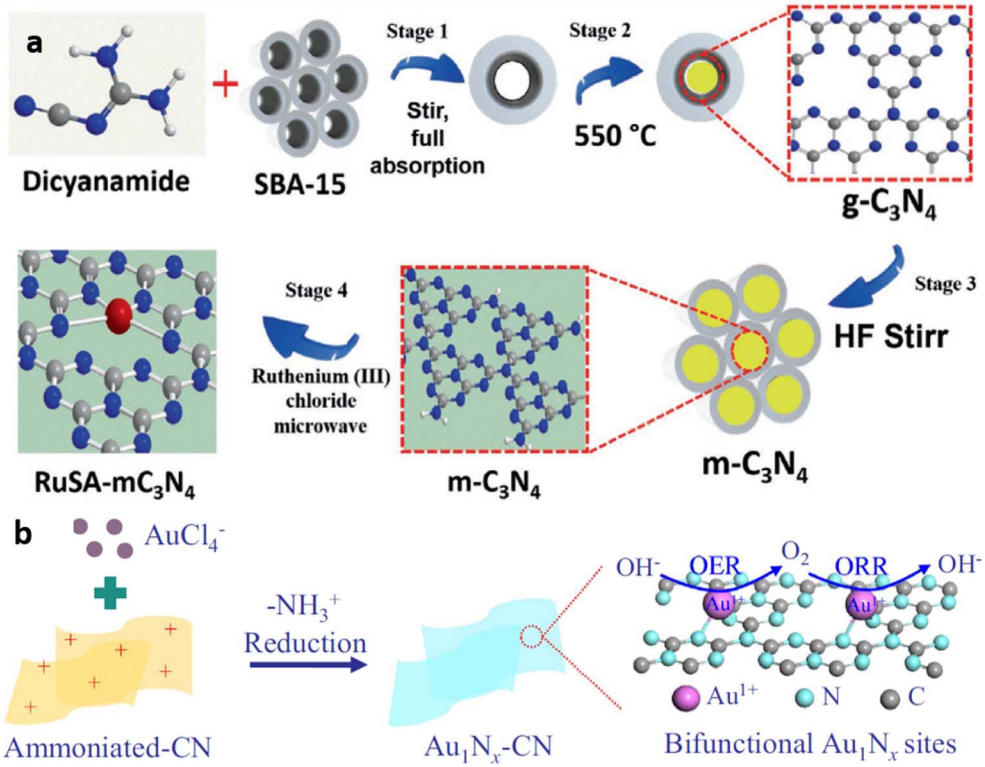

Fig. 7 (a) Schematic of microwave assisted post synthetic strategy for the development of ruthenium single atoms decorated mesoporous C_3N_4 (RuSA-mC_3N_4) catalyst. Reproduced with permission from ref. 21. Copyright 2021 John Wiley and Sons. (b) Schematic of electrostatic adsorption mediated post synthetic strategy for Au_1N_x single-site/C_3N_4 catalyst synthesis. Reproduced with permission from ref. 22. Copyright 2018 Elsevier.

supported on mpg-C_3N_4 with a metal loading of 0.0519 wt%. $HAuCl_4$ is added to an aqueous dispersion of mpg-C_3N_4 and the resulting product is annealed at the low temperature of 100 °C under an inert atmosphere of H_2/Ar. The Au ions are thus reduced to single Au atoms and the Au loading in the catalyst is regulated by changing the annealing temperature.[26]

Ultra-high density single atom catalysts (UHD-SACs) by atomic level dispersion of 15 transition metals on suitable supports having different structural and chemical characteristics were illustrated recently by Lu and co-workers. Consequently, UHD-SACs on supports like N doped carbon (NC), polymeric C_3N_4 (PCN) and metal oxide (CeO_2) were developed through a post synthetic strategy involving the impregnation of aqueous solutions of metal salts on supports followed by two-step annealing under inert atmosphere to realise a metal loading up to 23 wt%. The two-step annealing process facilitated the removal of ligands from metal precursors in a controlled manner and selectively coordinated metal ions to all the available anchoring sites present on the support surface to realise ultra-high metal loading. The first annealing step was done at temperatures (T_1) lower than the decomposition temperatures of the metal salts under an inert atmosphere. The unbound metal

Table 1 Common synthetic approaches for g-C_3N_4 based SACs

Synthesis	Techniques	Remarks
Direct synthesis	• Template free synthesis	• Effective stabilisation of single atoms as coordination occurs along with polymerisation of g-C_3N_4 precursors
	• Template assisted synthesis	• High & ultra-high metal loading can be realised
	• Molten salts & reflux method assisted synthesis	• Easily scalable & low cost
	• Supramolecular preorganisation assisted synthesis	• Necessarily involves high temperature pyrolysis (550–600 °C)
Post synthesis	• Chemical reduction	• Better control of the textural properties like surface area
	• Reduction under an inert atmosphere	• Low metal loading in general
	• Photochemical reduction	• Metal–support interaction is weak compared to direct synthesis
	• Electrostatic adsorption	• MW & ALD are hardware intense
	• Microwave treatment (MW)	
	• Atomic layer deposition (ALD)	

species were removed by washing to prevent the aggregation and sintering of the metal species in the subsequent annealing step. Further, the second stage of annealing at a higher temperature (T_2) completely removed the remaining ligands and transformed the chemisorbed metal species into highly stable UHD-SAC systems. The above two-step annealing strategy enabled the kilogram-scale production through robot assisted-automatic synthesis taking Ni UHD-SAC on PCN as a case study.[11]

Table 1 summarises the synthesis strategies with their attributes. In comparison, the direct synthesis route is more beneficial than post synthesis route to achieve g-C_3N_4 SACs with high metal content. Post synthetic methods suffer from the drawback of promoting aggregation leading to nanoparticle formation at high concentrations of the localised metal species. On the other hand, direct synthesis methodologies enable uniform distribution of single atoms but are susceptible to reduced atom efficiency owing to the entrapment of metal in the support matrices.

4 Analytical tools for understanding g-C_3N_4 based single atom catalysts

The atomically dispersed metal species over g-C_3N_4 matrix, act as a catalytically active centre for facilitating various catalytic reactions. It is imperative to cognise the atomic and electronic structure of the single atom sites of SACs to elucidate the mechanism governing its catalytic activity. Various analytical tools have thus been employed to substantiate the occurrence of metal species in single atom configuration, to determine its distribution over g-C_3N_4 matrix and its coordination environment. In this section, we examine the various characterisation techniques used for analysing g-C_3N_4 SACs and the elucidation of data from those techniques (Fig. 8).

4.1 XRD analysis

The detection limit of conventional X-ray powder diffraction for supported nanoparticles is often set at 2–2.5 nm size range, below which low signal to noise ratios make size detection challenging.[29] Absence of peaks in the XRD pattern of g-C_3N_4 based SACs merely rules out the existence of metal NPs and metal oxides, but not confirming the formation of metal single atoms. g-C_3N_4 exhibit two characteristic XRD diffraction peaks at 2θ values of 13.3° and 27.8° are attributed respectively to the in-planar structural packing of (100) crystallographic plane and the (002) lattice plane corresponding to the interplanar stacking of aromatic systems.[30] Due to the atomic level dispersion of single atoms over g-C_3N_4 matrix, the above characteristic XRD peaks diminish. For *e.g.*, Zhou and co-workers reported the complete

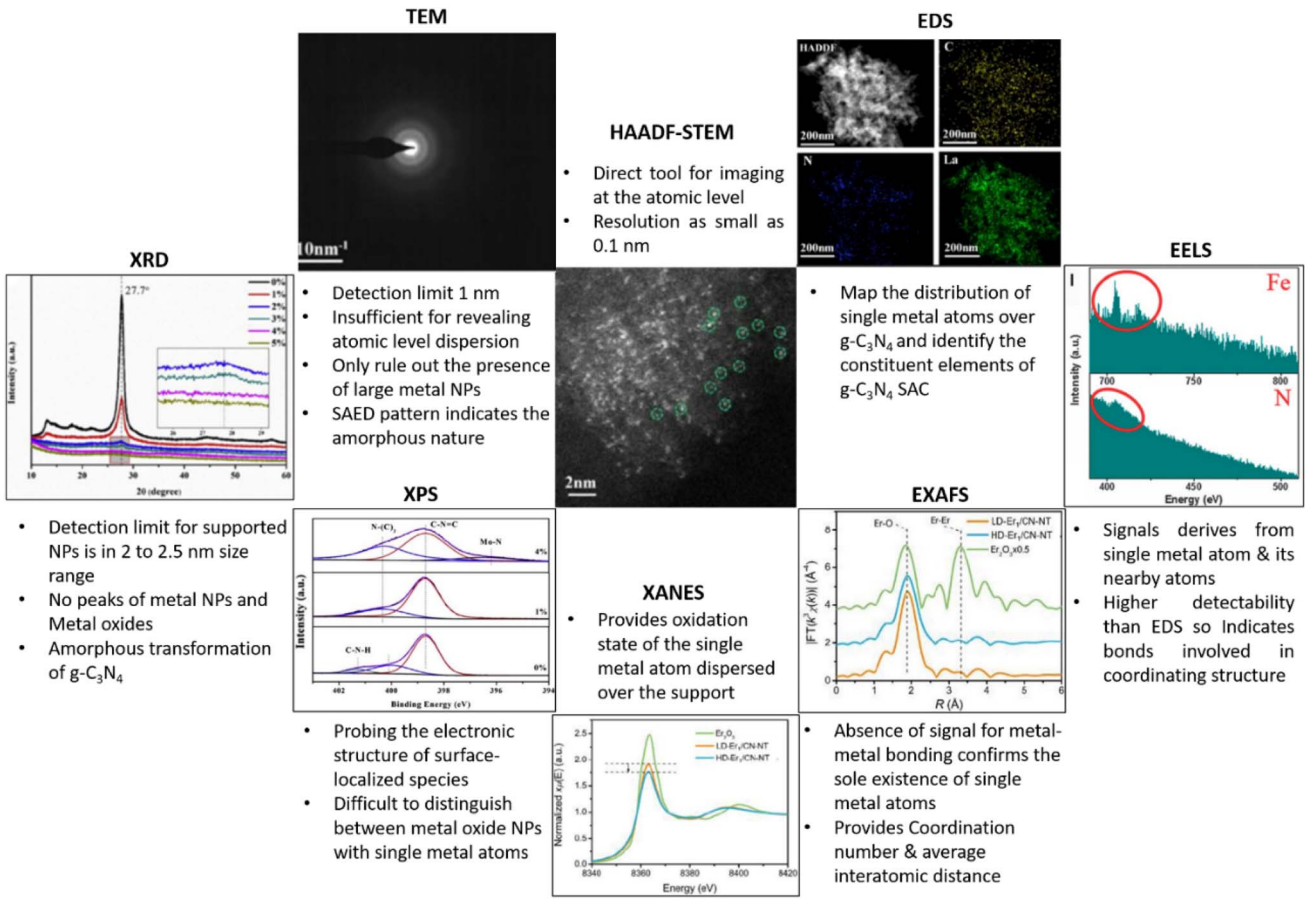

Fig. 8 Various analytical tools for the characterisation g-C_3N_4 based SACs. Reproduced with permission from ref. 9. Copyright 2020 John Wiley and Sons. Reproduced with permission from ref. 16. Copyright 2020 American Chemical Society. Reproduced with permission from ref. 27. Copyright 2019 Elsevier. Reproduced from ref. 28.

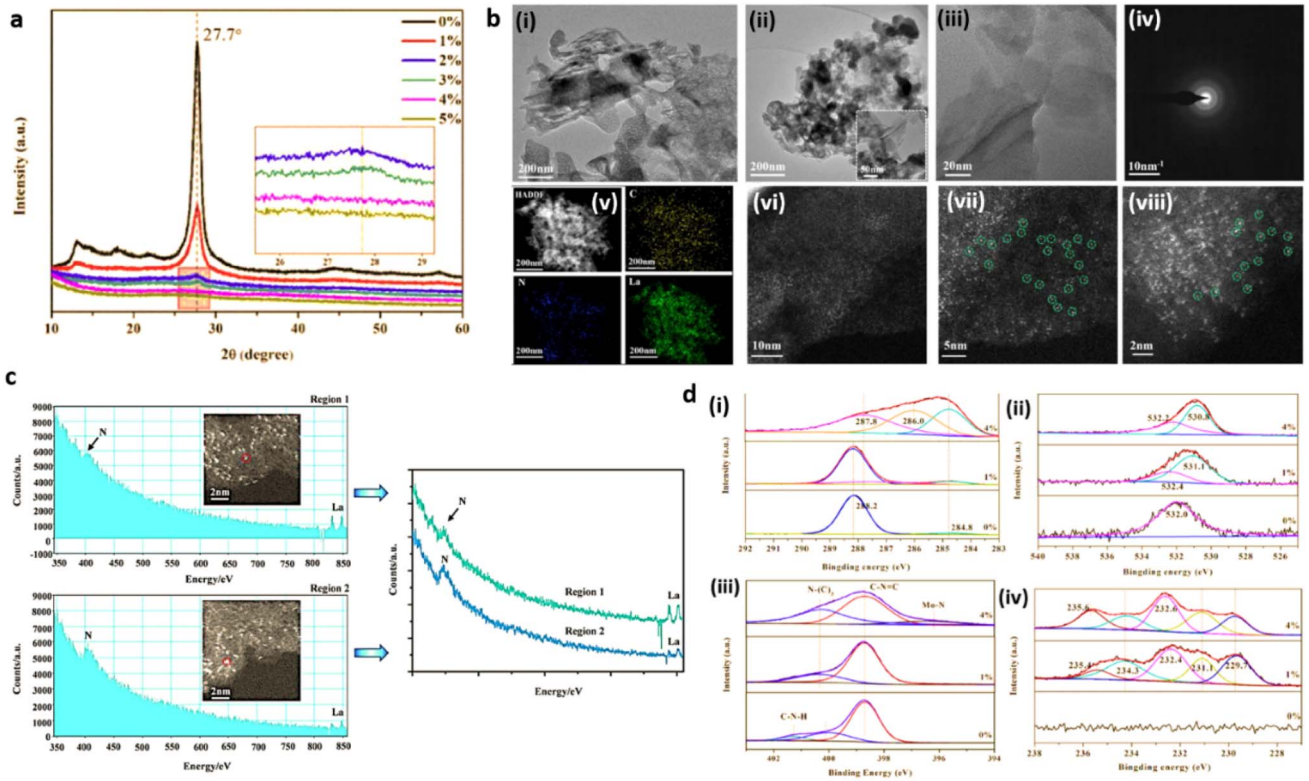

Fig. 9 (a) XRD patterns of g-C_3N_4 (0%) and Mo/C_3N_4 (1–5%). Reproduced with permission from ref. 27. Copyright 2019 Elsevier. (b) Morphological analysis of O/La–CN catalyst; (i and ii) TEM images, (iii) HAADF-STEM image of the thinner region, (iv) SAED pattern, (v) HAADF-STEM EDS mapping (yellow, blue, and green color represents carbon, nitrogen and lanthanum), (vi–viii) spherical aberration-corrected HAADF-STEM images, (c) EELS spectra of two separate labelled regions. Reproduced with permission from ref. 16. Copyright 2020 American Chemical Society. (d) XPS spectra; (i) C 1s, (ii) O 1s; (iii) N 1s, (iv) Mo 3d. Reproduced with permission from ref. 27. Copyright 2019 Elsevier.

disappearance of peaks when the Mo loading is increased to 4% (Fig. 9(a)). The long-range order of g-C_3N_4 is thus disturbed inducing the amorphous transformation of g-C_3N_4.[27]

4.2 Transmission electron microscopy (TEM)

Transmission electron microscopy (TEM) is extensively employed for the morphological and structural identification of material. However, the conventional TEM of nanoscale resolution is insufficient for imaging single-atoms as its normal detection limit is ≈1 nm. A combination of high-resolution TEM imaging and SAED imaging is commonly used to rule out the presence of large metal NPs in a given area of the SAC sample.[13,31] Nevertheless, the mentioned tools cannot be used to confirm the absence of NPs in the bulk sample. Additionally, the absence of lattice fringes and diffractions in HRTEM image and the selected area electron diffraction (SAED) pattern confirm the amorphous nature, as has been demonstrated by Dong *et al.* in g-C_3N_4 system with atomic level dispersion of La (O/La–CN) (Fig. 9(b)(i, ii) and (iv)).[16]

4.3 Aberration-corrected high-angle annular dark-field scanning transmission electron microscopy (HAADF-STEM)

Recent developments in the field of electron microscopy have led to the emergence of aberration-corrected high-angle annular dark-field imaging scanning TEM (HAADF-STEM), with a resolution as small as 0.1 nm providing atomic scale information.[32] Single metal atoms are identified on supports with the aid of HAADF-STEM with aberration correctors, provided the atomic number of the metal atom of interest is much higher than the constituent element of the supports. The single-atoms dispersed on the g-C_3N_4 matrix and its spatial distribution can be directly imaged using aberration corrected HAADF-STEM analysis.[33] For example, HAADF-STEM imaging and the associated analysis of rare-earth La single atoms on carbon nitride (O/La–CN) (Fig. 9(b)(iii) and (vi–viii)) revealed the existence of single La atoms over g-C_3N_4 matrix.[16]

4.4 Energy-dispersive X-ray spectroscopy (EDS) and electron energy-loss spectroscopy (EELS)

Energy-dispersive X-ray spectroscopy (EDS) and/or electron energy-loss spectroscopy (EELS) are always used in conjunction with STEM for validating the composition of the synthesised g-C_3N_4 SACs.[34,35] Energy-dispersive X-ray spectroscopy (EDS/EDX) together with HAADF-STEM is used to map the distribution of single metal atoms over g-C_3N_4 matrix and to identify the constituent elements. The energy-dispersive spectroscopy (EDS) mapping of O/La–CN confirmed the uniform distribution of La, N and C elements in the g-C_3N_4 framework (Fig. 9(b)(v)). EELS spectra derived from the positioning of an electron probe

directly over a single atom can deliver information about the coordination environment by nearest neighbouring atoms. EELS spectra of O/La–CN from two selected locations are compared in (Fig. 9(c)). The presence of N and La atoms in this location, with no evident O, suggests La–N coordination structure.[16]

HAADF-STEM in combination with EDS/EELS allows the direct visualisation of single atoms only in a limited area and cannot provide conclusive evidence for the absence of metal nanoparticles in the bulk of the material. So, it's critical to analyse microscopic observations in conjunction with spectroscopic tools that could provide overall information about SACs such as chemical and electronic structure, coordination environment of g-C_3N_4 based SACs. X-rays, owing to their short wavelength (0.01–1 nm), are the most suitable source for atomic scale structural information, X-ray Absorption Spectroscopy (XAS) is thus used to detect the detailed coordination environment of single atoms. Spectroscopic techniques, in comparison with microscopic tools, can better resolve elements of similar atomic weights (*e.g.*, N and C, Co and Mo) and can thus be utilised to derive qualitative and quantitative information about the valence state of single atoms.[36] *In situ* and operando characterisations are enabled in XAS as it can operate without ultrahigh vacuum requirements. Similarly, X-ray photoelectron spectroscopy (XPS) measurements can identify the variations in surface composition and valence state.[37]

4.5 X-ray photoelectron spectroscopy (XPS)

XPS is an essential characterisation tool for probing the electronic structure of surface-localised species and for determining the valence states of surface elements. Single metal atoms supported on 2D matrices normally possess partial (or full at times) positive charge due to the strong covalent coordination or ionic interaction with neighbouring surface atoms or ligands. The heterogeneity/homogeneity of single atom species is mostly identified through a singlet peak in the XPS analysis which indicates a unified positive charge for the metal elements.[38,39]

XPS analysis of a single Mo atom dispersed on g-C_3N_4 matrix (a-Mo/C_3N_4, where a = (0–4%)) revealed the amorphous transformation of g-C_3N_4 due to atomic level dispersion of Mo atoms over the matrix. The C 1s spectra of pure g-C_3N_4 exhibit peaks at 284.8 eV and 288.2 eV which are attributed to the adventitious C contamination and C–N bonds respectively. For a-Mo/C_3N_4, the peak at 284.8 eV related to the C–C bond has grown significantly, and the peak of the C–N bond has shifted to 287.8 eV. The "outward twisting of melon units" and the hydrogen bond cleavage of polymeric strands of melon units are responsible for these changes in the XPS spectra, confirming that g-C_3N_4 has undergone an amorphous transformation. The high-resolution N 1s XPS spectra of g-C_3N_4 displayed peaks corresponding to C–N–C bond and N–$(C)_3$ bond, and C–N–H bond at 398.7 eV, 400.1 eV, and 401.3 eV respectively. The dispersion of Mo single atoms induces the disappearance of C–N–H bond peak due to the above-mentioned H-bond cleavage. A new peak for a-Mo/C_3N_4 can be seen at 396.2 eV, which is derived from the Mo–N bond, demonstrating the creation of the Mo–N bond after the insertion of Mo atoms. The O 1s spectra of pure g-C_3N_4 have a peak at 532.0 eV due to the C–O bond, and a second peak at 531.1 eV appears due to the –OH bond during the formation of Mo single atoms from ammonium molybdate precursor. Furthermore, Mo(VI) and Mo(V) $3d_{3/2}$ orbitals are evidenced by peaks at 235.4 and 234.3 eV respectively, while Mo(VI), Mo(V), and Mo(IV) $3d_{5/2}$ orbitals are confirmed from peaks at 232.4, 231.1, and 229.7 eV, revealing the abundant valence state of Mo in a-Mo/C_3N_4 (Fig. 9(d)(i–iv)).[27]

4.6 X-ray absorption spectroscopy

X-ray Absorption Spectroscopy (XAS) is an element-specific technique for probing the local coordination environment by detecting fluctuations in the absorption of an ejected photoelectron due to multiple scattering pathways.[37,40] XAS analysis mainly consists of extended X-ray absorption fine structure (EXAFS) and X-ray absorption near-edge structure (XANES) analyses. The atoms surrounding the single atom produce outgoing and backscattered waves and their interference yields EXAFS spectra. EXAFS analysis of SAC provides essential information regarding the coordination number of single atom site(s) and its interatomic distance with backscatter atoms within its vicinity, in comparison with standard metal foil and metal oxides. The structural disorder and the type of neighbouring atoms present at a specific bond length are also deduced from EXAFS. The absence of signal corresponding to metal–metal interaction in EXAFS spectra rules out the formation of metal NPs and metal oxides.[38]

XANES analysis further helps in determining the oxidation state of the single metal atom dispersed over the support. XAS analysis techniques establish the identity of single metal atoms through EXAFS and derive quantitative data related to coordination. Further, XAS analysis proposes suitable geometric arrangements for single metal atoms through the curve-fitting of XANES data based on predictable coordination environments. Fig. 10(a–e) shows the XAS analysis details of low-density (2.5 wt% Er loading) and high-density (20.1 wt% Er loading) Er single atom anchored on g-C_3N_4 nanotubes (Er_1/CN-NT). Fourier transform-extended X-ray absorption fine structure (FT-EXAFS) reveals radial distance resolution (R-space) while wavelet transform-extended X-ray absorption fine structure (WT-EXAFS) can discriminate the backscattering atoms to provide resolution in both R-space and k-space. FT-EXAFS spectra, of LD-Er_1/CN-NT and HD-Er_1/CNNT samples, exhibited only one main peak at around 1.8 Å. The absence of a peak at about 3.5 Å, corresponding to Er–Er interaction for LD-Er_1/CN-NT and HD-Er_1/CNNT samples confirmed the formation of a single Er atom over CNNT without the formation of metallic crystalline Er species. WT-EXAFS plots also supplemented the above observation due to the presence of only one intensity maximum at around 4.0 $Å^{-1}$ corresponding to Er–N bond for the LD-Er_1/CN-NT and HD-Er_1/CN-NT samples.

The white line intensity reduction of Er L3-edge XANES spectra with the increase in Er loading from 2.5 wt% to 20.1 wt%, indicate a decrease in the oxidation state of Er in the

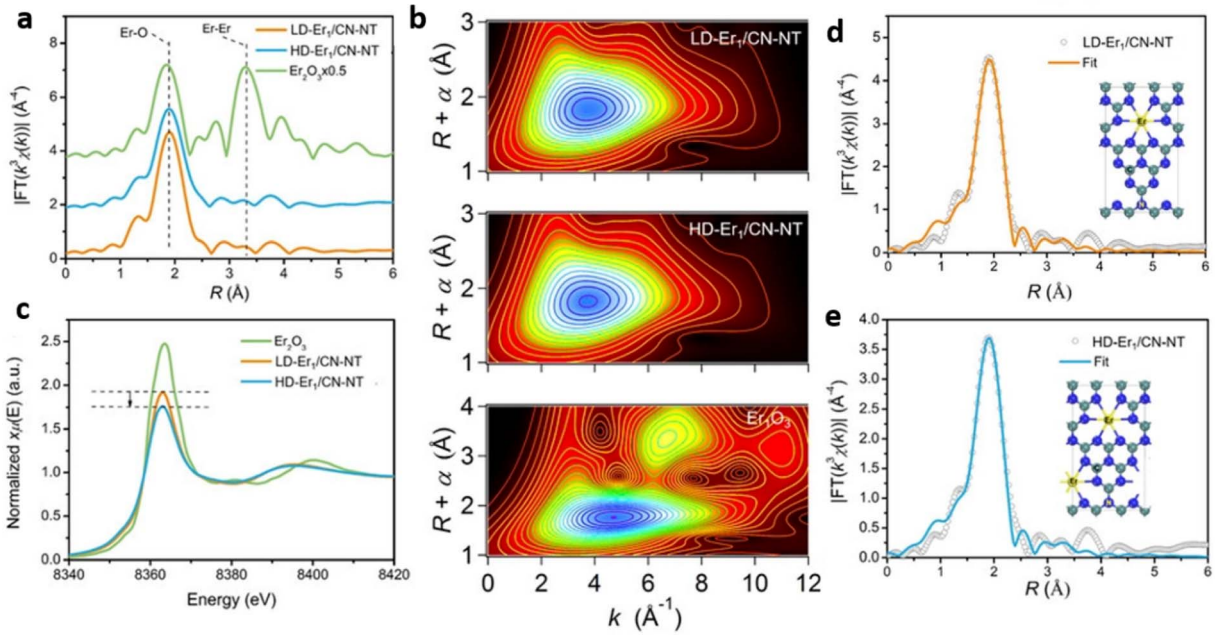

Fig. 10 (a) The k^3-weighted Fourier transform spectra from EXAFS for Er_2O_3, LD-Er_1/CN-NT, HD-Er_1/CN-NT in *R* space (b) wavelet transform (WT) contour plots of Er_2O_3, LD-Er_1/CN-NT, HD-Er_1/CN-NT (c), the normalised XANES spectra at the Er L_3 edge of Er_2O_3, LD-Er_1/CN-NT, HD-Er_1/CN-NT, The EXAFS *R* space fitting curves and corresponding model for (d) LD-Er_1/CN-NT and (e) HD-Er_1/CN-NT respectively Er, N, C atoms are represented by yellow, blue, green spheres respectively. Reproduced with permission from ref. 9. Copyright 2020 John Wiley and Sons.

order Er_2O_3 > LD-Er_1/CN-NT > HD-Er_1/CN-NT. In comparison to LD-Er_1/CN-NT, HD-Er_1/CN-NT has a flattened white-line peak at 8360 eV, implying an interaction between central and surrounding Er atoms resulting in the charge redistribution due to the shortening of spatial distance between neighbouring Er atoms. Quantitative least-squares EXAFS analysis demonstrated that both LD-Er_1/CN-NT, and HD-Er_1/CN-NT exhibited one main peak at around 1.8 Å arising from the first shell of Er–N scattering. EXAFS results also indicated that the single Er atoms have a first shell coordination number of six in both LD-Er_1/CN-NT and the HD-Er_1/CN-NT samples.[9]

5 Catalytic applications of single atom confining on g-C_3N_4 matrix

5.1 Photocatalysis

Visible light-driven semiconductor photocatalysis is widely pursued as an environmentally benign and sustainable solution for pollution control and energy production. Photocatalyst alters the kinetics of a chemical reaction upon light irradiation through the creation of highly effective reactive oxygen species (ROS) and has been demonstrated for applications like the degradation of organic pollutants in wastewater, creating self-cleaning surfaces, splitting water for hydrogen evolution, *etc.*[41] The photocatalyst possesses a favourable combination of electronic structure, excited-state life time, light absorption properties and charge transport characteristics.[42]

g-C_3N_4, because of its flexible indirect band edge positions, excellent thermal stability, resistance to acids and bases, and insolubility in common solvents like water, ethanol, acetone, *etc.*, is found suitable for a wide range of photocatalytic applications. These properties originate from the van der Waals force that holds together the stacked graphitic layers.[43,44] Nevertheless, the application of g-C_3N_4 is limited as it utilises only a small region of the visible spectra. A low specific surface area in the range of 10–30 $m^2\ g^{-1}$ for bulk g-C_3N_4 is also an impediment to widespread applications owing to the reduction in reactive sites. The high rate of recombination of excitons, poor light harvesting, and limited generation of radical species are the factors primarily responsible for its low catalytic efficiency during the redox reactions.[45]

The recombination process in g-C_3N_4 is perceived to be controlled by facilitating separation between photogenerated electron–hole pairs and various strategies such as heterostructure formation, incorporation of metal co-catalyst, impurity doping, *etc* are demonstrated thus far. Among them, the incorporation of a metal co-catalyst is a viable strategy to reduce exciton recombination as the metal Fermi level is positioned in between the band edge positions of C_3N_4. The transfer of photogenerated electrons from the conduction band (CB) to the metal enables the separation of the exciton pairs leading to improved photocatalytic efficiency.[43]

The usage of noble metals such as Au, Pt, Pd as co-catalyst is effective but is limited due to their high cost. Replacement of noble metals with cost-effective transition metals is an affordable solution for the applications of g-C_3N_4 based photocatalysts. However, very low atom utilisation efficiency, availability of minimal catalytically active species and poor selectivity of the metal nanoparticles are the bottlenecks for its practical application. Metal particles of appropriate sizes can

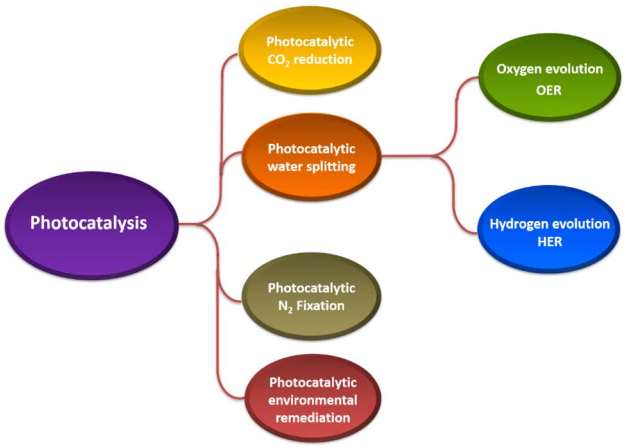

Fig. 11 Various reactions catalysed by g-C_3N_4 based SACs in the area of photocatalysis.

only act as catalytically active species while those with non-optimal sizes may facilitate various undesired secondary reactions which further reduce the catalytic efficiency of the catalyst. To overcome these limitations, g-C_3N_4 based catalysts with atomic level dispersion of metal are recently developed.[46]

SACs comprising of spatially isolated, individual metal atoms stabilised on C_3N_4 matrix, show unusual potential due to unsaturated coordination sites for realising maximum atom-utilisation efficiency. Consequently, C_3N_4 based on SACs and ADMCs with unique electronic structures serve as potential candidates for catalysing various reactions by virtue of their advantages such as remarkably high catalytic activity, reduced catalyst amount, and abundance of single active sites.[13]

The past few years have seen significant research efforts leading to the development of a research domain of g-C_3N_4 based single atom photocatalysts for various applications (Fig. 11).

Zhang *et al.* employed density functional theory (DFT) to study the improved photocatalytic activity of g-C_3N_4 based transition-metal (Fe, Co, Ni, Cu and Zn) single atom catalysts. To identify the adsorption sites of single atoms of various transition metals on multi-layered g-C_3N_4 sheets, a three-layer g-C_3N_4 structure was constructed by cleaving the (001) g-C_3N_4 surface. The structure comprising 24 N atoms and 18 C atoms and with the optimised lattice parameter values of $a = b = 7.13$ Å, $c = 21.54$ Å contained numerous six-fold cavities capable of trapping metal single atoms (Fig. 12).[7]

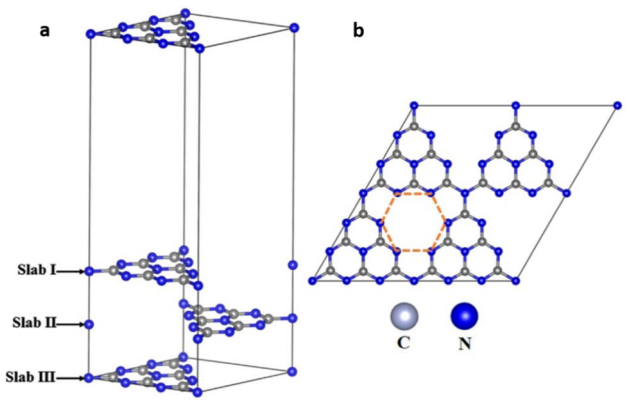

Fig. 12 (a) Schematic representation of three-layer g-C_3N_4 model, (b) 2 × 2 × 1 supercell monolayer g-C_3N_4. The highlighted ring composed of six numbers of bi-coordinated nitrogen atoms is referred to as six-fold cavity. Reproduced with permission from ref. 7. Copyright 2018 Elsevier.

Due to the presence of empty d orbitals in transition metals, single atoms of Fe, Co, and Ni were inserted into the layers of g-C_3N_4 sheets through strong coordination with their neighbouring C, N atoms. On the other hand, Cu and Zn atoms with completely filled d orbitals stay at the six-fold cavities present in the g-C_3N_4 surface through coordination with N atoms present at the edge of the cavities. The charge carrier transfer between the interlayers of g-C_3N_4 is reduced due to the high interlayer distance of 3.27 Å resulting in a high rate of exciton recombination. Incorporating single atoms of metal altered the interlayer spacing of g-C_3N_4. The loading of Fe, Co, and Ni single atoms significantly shortens the interlayer distance between slabs I and II. The value decreased from 3.27 to 2.25, 2.41 and 2.39 Å for Fe, Co and Ni respectively. The interlayer charge transfer was thus accelerated for aforementioned SACs. However, the incorporation of Cu and Zn atoms hardly affected the interlayer spacing with minimal reduction in values to 2.90 Å and 2.75 Å respectively. Similar reductions in the interlayer spacing between slab II and slab III were also observed in Fe/g-C_3N_4, Co/g-C_3N_4 and Ni/g-C_3N_4 with interlayer distances of 2.47 Å, 2.48 Å and 2.45 Å respectively. For Cu/g-C_3N_4 and Zn/g-C_3N_4, the interlayer spacing between slab II and III remains almost unchanged at 3.28 Å.[7]

The bond population is an effective measure of the nature of a chemical bond and a low value indicates that the ionic nature of the bond increases and the covalent nature decreases. The covalent nature of C–N bond in g-C_3N_4 is justified by its bond population value of >0.7. The bond population values for all the bonds between metal atoms and adjacent non-metal atoms (C or N) present in the catalysts are significantly lower than 0.7, which indicates greater electron delocalisation leading to accelerated charge transfer between g-C_3N_4 layers. The formations of Cu–N and Zn–N (metal–nitrogen bonds) in Cu/g-C_3N_4 and Zn/g-C_3N_4 are not sufficient to improve the charge transfer between layers while the presence of both metal–carbon and metal–nitrogen bonds in Fe/g-C_3N_4, Co/g-C_3N_4 and Ni/g-C_3N_4 systems exhibited enhanced charge transfer properties.[7]

5.1.1 Photocatalytic carbon dioxide reduction. The rational design of photocatalytic systems that are responsive to visible light holds great potential for the effective conversion of carbon dioxide (CO_2) to value-added feedstock, thereby combating the increased environmental issues created by uncontrolled emissions. The chemical reduction of CO_2 to simple C_1/C_2 chemicals such as CO, HCOOH, CH_4, HCHO, C_2H_5OH, CH_3OH, and other hydrocarbon compounds using renewable and inexhaustible solar energy mediated photocatalytic process has emerged as a possibility.[47] However, the high C=O dissociation energy of ~750 kJ mol^{-1} and the optically inert nature of CO_2 molecule in the wavelength range of 200–900 nm, render the reduction

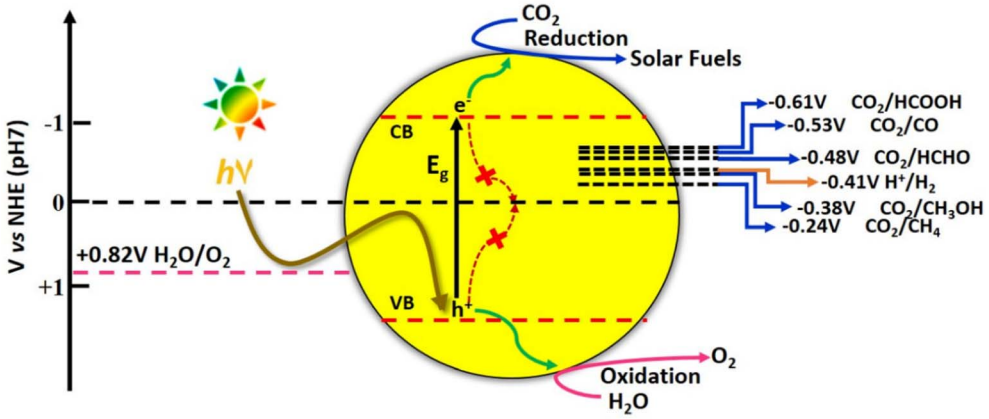

Fig. 13 Schematic illustration of photocatalytic carbon dioxide reduction.

process extremely difficult and complex with multiple proton and electron transfer pathways.[48] It is therefore imperative to develop photocatalytic systems with appropriate band structures that are responsive to solar radiation. The resulting photogenerated electrons facilitate the CO_2 reduction process to various value-added products. The one-electron reduction of CO_2 to $CO_2^{\bullet-}$ is thermodynamically unfavourable due to the highly negative reduction potential value of −1.90 V *vs.* NHE, at pH 7.0.[49] The multiple proton–electron assisted CO_2 reduction reactions occur at lower redox potential values as listed in Fig. 13.

However, the reaction pathways are all uphill reduction processes ($\Delta G > 0$) and the conversion efficiencies are not yet appreciable for the reduction of CO_2 to hydrocarbon fuels using H_2O as a reductant.[50] Moreover, due to the very close matching of redox potentials of possible products, the selectivity is very poor, particularly for C_2 products. Furthermore, the stability of the intermediate formed during multiple proton–electron transfer pathways involved in the reduction reaction determines the product selectivity.[51]

In the early emerging period of SACs, Du and co-workers explored the potency of Pd and Pt single metal atoms supported on g-C_3N_4 towards photocatalytic CO_2 reduction by density functional theory (DFT) calculations. Pd and Pt single atoms are stably confined into the six-fold cavity of g-C_3N_4 through the interaction of electron lone pairs present in the neighbouring pyridinic nitrogen atoms. The calculated binding energies for Pd and Pt were respectively −2.17 eV & −2.95 eV. In Pd/g-C_3N_4 & Pt/g-C_3N_4 systems, the noble metal atoms act as active sites, while the g-C_3N_4 matrix serves as a source of hydrogen which is generated through hydrogen evolution reaction. The evaluation of reaction pathways suggests HCOOH, with a reaction barrier of 0.66 eV, as the product expected for Pd/g-C_3N_4. On the other hand, Pt/g-C_3N_4 system was expected to reduce CO_2 to CH_4 with a reaction barrier of 1.16 eV. This study established the correlation between the metal and the product selectivity during the photoreduction process. The distribution of Pd or Pt metal as single atoms over g-C_3N_4 framework led to enhanced visible light absorption, thereby making it a potential candidate for visible light driven photocatalytic CO_2 reduction. This theoretical study paved the way for developing various g-C_3N_4 based SACs for CO_2 photoreduction reaction and its experimental validation.[5]

Li and co-workers synthesised visible light active non-noble metal Co^{2+}@C_3N_4 catalyst for CO_2 reduction by stabilising cobalt single atoms on g-C_3N_4 matrix through Co–N coordination. Photocatalysts containing single Co^{2+} sites on C_3N_4 exhibited excellent CO_2 reduction capacity and product selectivity towards CO formation. The effect of metal loadings on CO production and product selectivity was studied by varying cobalt content between 0.004 and 0.430 μmol Co^{2+} per 1 mg C_3N_4. A significant amount of CO formation was observed with cobalt loading lower than even 0.010 μmol mg^{-1}. The CO formation increased linearly until a cobalt loading of 0.128 μmol mg^{-1} was reached. Further increase in metal loading led to a slight decline in CO production due to the formation of inactive cobalt oxides. The product selectivity of the reduction reaction was however unaffected by the presence of dormant cobalt oxide formed at relatively high Co content.[52]

Zhou and co-workers successfully demonstrated the amorphous transformation of g-C_3N_4 by atomically dispersing Mo atoms over g-C_3N_4 matrix. The Mo–C and Mo–N bonds altered the long-range order of g-C_3N_4 and the retention of each melon unit led to a crystalline to an amorphous phase transition. This transformation to amorphous g-C_3N_4 enabled significant enhancement in its light absorption in the visible range with a strong band tail and an absorption edge up to 750 nm. Additionally, the newly formed Mo–C and Mo–N bonds enhanced the charge separation dynamics by acting as pathways for photogenerated excitons. The excellent photocatalytic CO_2 reduction capacity of Mo/C_3N_4 systems was attributed to the enhanced visible light activity of the catalyst along with the reduced recombination rate of photo excitons. Under visible light irradiation, Mo/C_3N_4 systems exhibited the CO and H_2 production rates of 18 and 37 μmol g^{-1} h^{-1} respectively which is 10.6- and 4-folds greater than that of crystalline g-C_3N_4.[27]

Wang *et al.* developed atomically dispersed rare earth erbium (Er) atoms on carbon nitride nanotubes for CO_2 reduction through a strategy involving "atom confinement and

coordination (ACC)". The methodology of confining Er precursor and urea on melamine sponge, achieved at liquid N_2 temperature, facilitated coordination between dispersed Er ions and N atoms of the g-C_3N_4 precursor. The ACC strategy helped to fine tune the metal content from 2.5 wt% to 20.1 wt% and could also be utilised for a variety of rare earth metals of lanthanide series. Photocatalytic CO_2 reduction by high-density Er single-atom catalyst (HD-Er_1/CN-NT) under simulated solar light produced CH_4 and CO at the rates of 2.5 μmol g^{-1} h^{-1} and 47.1 μmol g^{-1} h^{-1} respectively which is higher than that of low-density Er single-atom catalyst (LD-Er_1/CN-NT) and bare g-C_3N_4 nanotube catalyst (CN-NT). The presence of Er active sites in large numbers is presumed to be the cause for improved CO_2 conversion rates. Moreover, the availability of multiple basic sites for CO_2 adsorption, as corroborated by CO_2-TPD measurements, promoted enhanced reduction capacity in HD-Er_1/CN-NT samples. DFT calculations revealed that the gaseous CO formation has a low theoretical limiting potential (0.3 V) than CH_4 (0.39 V). Advantageously, the limiting potential for H_2 evolution reaction, calculated to be 0.82 V, was much greater than that of CO and CH_4. Hence unfavourable H_2 production could be successfully alleviated by Er atom catalysts.[9]

Another prominent school of thought practiced in SACs is on the synthesis of crystalline g-C_3N_4, primarily to overcome the demerits associated with the bulk morphology and excessive defects of amorphous g-C_3N_4. Xiang and co-workers reported the development of copper single atoms incorporated crystalline g-C_3N_4 nanorods (Cu–CCN) by molten salt and reflux method. The prepared Cu–CCN photocatalyst showed 100% CO selectivity with an improved generation rate of 3.086 μmol h^{-1} g^{-1} compared to 1.68 μmol h^{-1} g^{-1} and 0.895 μmol h^{-1} g^{-1} for crystalline and bulk counterparts. The CO_2 adsorption capacity of Cu–CCN samples was enhanced as single Cu atoms served as sorption sites for CO_2. Theoretical calculations revealed that the reduction of CO_2 to CH_4 is an entropy increasing process on Cu–CCN samples, while the reduction of CO_2 to CO is a process of decreasing entropy, thereby facilitating 100% product selectivity towards CO (Fig. 14(a)).[18]

In a noteworthy contribution, Cao *et al.* developed a g-C_3N_4 based photocatalyst with atomically fused-Cu atoms through C–Cu–N_2 four-center bond formation. An artificial enzyme like configuration, similar to hemocyanin, is created where the single atom copper exhibited a mixed valence state of Cu^+/Cu^0 at the oxidation potential of +1.5 V. Composition with 0.25 wt% copper produced CO, CH_3OH and CH_4 at the rates of 11.21, 1.75 and 0.61 μmol g^{-1} h^{-1} respectively. Further increase in copper content led to the decline of photocatalytic activity owing to the surplus metal sites acting as charge recombination centres. CO was the major product of CO_2 reduction, as the desorption of CO molecules was made easier at single Cu atom active centres.

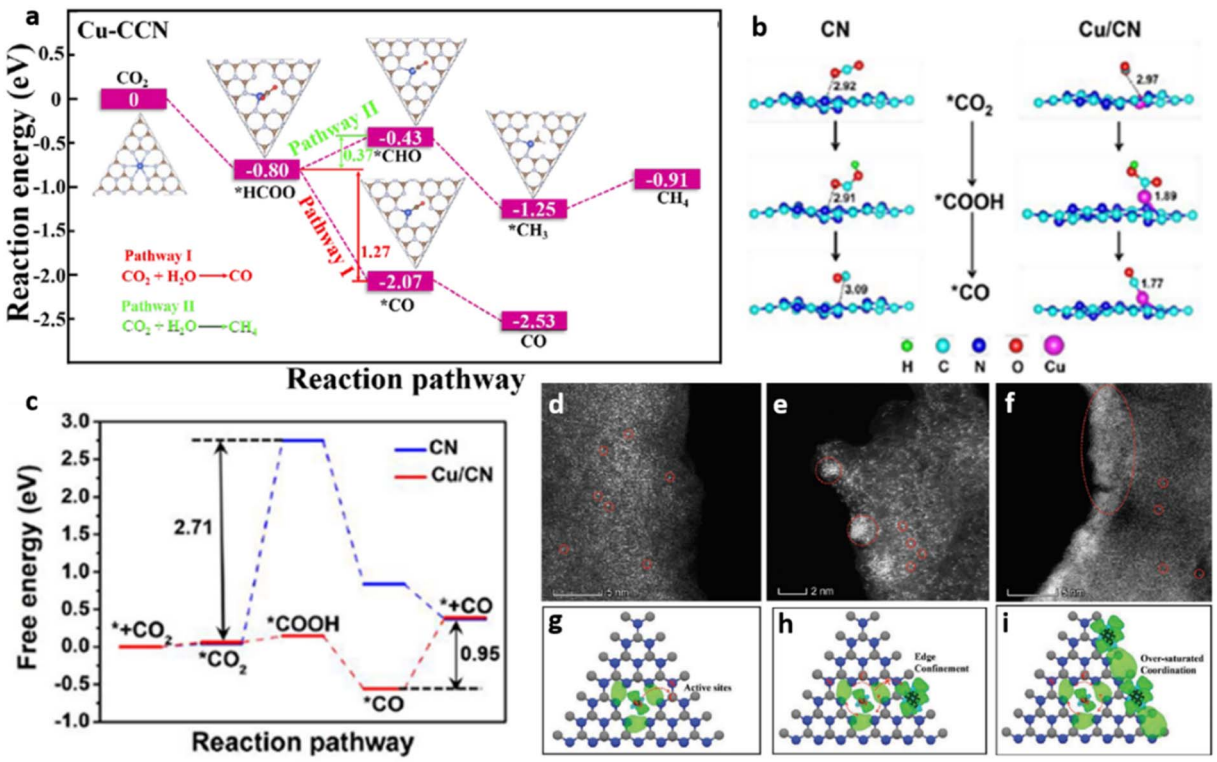

Fig. 14 (a) Schematic of the photocatalytic CO_2 reduction pathway on Cu–CCN derived from DFT calculation. Reproduced with permission from ref. 18. Copyright 2020 American Chemical Society. (b) Proposed structures and CO_2 reduction pathway corresponding to CN & Cu/CN photocatalyst (c) free energy diagram for the conversion of CO_2 to CO on CN and Cu/CN photocatalysts. Reproduced with permission from ref. 53. Copyright 2020 American Chemical Society. Aberration-corrected HAADF-STEM images of (d) Ni_1–CN, (e) Ni_5–CN, (f) and Ni_{10}–CN, models showing a difference in the charge distribution of (g) Ni_1–CN, (h) Ni_5–CN, and (i) Ni_{10}–CN. Reproduced with permission from ref. 54. Copyright 2020 John Wiley and Sons.

The DFT studies revealed that the terminal C–Cu–N_2 four-centre active sites present in g-C_3N_4 nanosheets served as a sink for photogenerated electrons while providing reactive binding sites for CO_2 activation. The proposed reaction pathway (Fig. 14(b)) followed the sequences of CO_2 adsorption followed by its hydrogenation to form *COOH. Subsequently, OH group dissociates from *COOH forming adsorbed *CO followed by the desorption of CO molecule from the catalyst surface. The enhanced CO_2 reduction performance of Cu/CN system over CN is attributed to the low free energy change (ΔG) of 0.95 eV associated with the rate limiting step (desorption of CO) on Cu/CN compared to a large ΔG of 2.71 eV associated with rate limiting step (hydrogenation of adsorbed *CO_2) on bare CN (Fig. 14(c)).[53]

In a recent contribution, Dong *et al.* converted CO_2 to CO efficiently by employing single-atoms of La on C_3N_4 by creating La–N charge bridges for efficient electron transport. The photocatalyst (O/La–CN), synthesised by one-step calcination involving the precursors of urea and lanthanum carbonate, exhibited complete amorphisation characterised by the absence of XRD peaks of g-C_3N_4. O/La–CN exhibited 80.3% selectivity at the high yielding rate of 92 μmol g^{-1} h^{-1} for CO. The La–N bridge, formed by the combination of various electronic states originating from 4f and 5d orbitals of La and the p–d orbital hybridisation, facilitated the CO_2 activation, COOH* formation and CO desorption steps.[16]

The Ni-anchored g-C_3N_4 photocatalyst was designed by anchoring single atoms of Ni on a few-layer g-C_3N_4 synthesised through a self-limiting process. Such a few-layer g-C_3N_4 structure with high porosity offers ligands for trapping Ni atoms, thereby realising a high density of single atoms. The single Ni atoms were distributed on the edges of the g-C_3N_4 sheets through an "active unsaturated edge confinement strategy" providing maximum atom-utilisation efficiency for high CO_2 adsorption capacity. The highly unsaturated Ni–N coordination offered pathways for the electron transfer from g-C_3N_4 to single Ni atoms realising improved photocatalytic activity for CO_2 conversion to CO. The prepared photocatalysts contained 2.54, 7.95, and 12.18 wt% of Ni content respectively for Ni_1–CN, Ni_5–CN, and Ni_{10}–CN compositions. The Ni_5–CN composition produced 8.6 μmol g^{-1} of CO and 0.5 μmol g^{-1} of CH_4 generation in the first 1 h, and was much higher than those of bare CN (CO: 1.1 μmol g^{-1} h^{-1}, CH_4: 0.1 μmol g^{-1} h^{-1}), and Nip + CN (CO: 2.7 μmol g^{-1} h^{-1}, CH_4: none), and $NiCl_2$+CN (CO: 3.3 μmol g^{-1} h^{-1}, CH_4: none) compositions (Fig. 14(d–i)).[54]

Combining experimental and computational studies, Hao *et al.* evaluated photocatalytic reduction of CO_2 to CO using water as a reductant and g-C_3N_4 containing single-atom Fe as a catalyst. The photo-physical and photo-chemical processes associated with CO_2 reduction mechanisms were analysed in detail. The reduction mechanism involved the activation of CO_2 molecules, formation of COOH radicals through water oxidation (proton transfer from H_2O to CO_2) and cleavage of C–O bond in COOH radicals. It is proposed that the activation process initiates through hydrogen-bonded complexes between CO_2, H_2O, and photocatalysts *i.e.*, g-C_3N_4 or Fe-g-C_3N_4. As represented in Fig. 14(j), there are two hydrogen bonds, namely HB-

Table 2 Summary of g-C_3N_4 SACs for photocatalytic carbon dioxide reduction

System	Single atom & loading	Synthesis method	Products & rate	Coordination site or structure & oxidation state	Ref.
Pd/g-C_3N_4 & Pt/g-C_3N_4	Pd, Pt	DFT study	HCOOH for Pd/g-C_3N_4 & CH_4 for Pt/g-C_3N_4	Nitrogen	5
Co^{2+}@C_3N_4	Co-0.128 μmol mg^{-1}	Microwave assisted post synthesis	CO 1.056 μmol mg^{-1} for 2 h	Nitrogen, +1	52
a-Mo/C_3N_4	Mo 3.3%	Template free direct synthesis	CO & H_2,18 & 37 μmol g^{-1} h^{-1}	Mo–C & Mo–N	27
Er_1/CN-NT	Er 18.4 wt%	Freeze drying assisted direct synthesis	CH_4 & CO 2.5 & 47.1 μmol g^{-1} h^{-1}	Er–N_3, +1	9
Cu–CCN	Cu atomic fraction 10.95%	Molten salts & reflux method (direct synthesis)	CO 3.086 μmol g^{-1} h^{-1}	Nitrogen	18
Cu/CN	Cu 0.25%	Supramolecular pre-organisation (direct synthesis)	CO, CH_3OH, CH_4 11.21, 1.75 & 0.61 μmol g^{-1} h^{-1}	C–Cu–N_2	53
O/La–CN	La	Template free direct synthesis	CO 92 μmol g^{-1} h^{-1}	La–N	16
Ni/C_3N_4	Ni 2.54 wt%	Template free direct synthesis	CO & CH_4 1.1 μmol g^{-1} h^{-1} & 0.1 μmol g^{-1} h^{-1}	Ni–N	54
Fe/C_3N_4	Fe 1.4 wt%	Post synthesis	CO 5.1 μmol g_{cat}^{-1} in 10 h	Fe–N	55
Ru/mpg-C_3N_4	Ru 0.4%	Microwave assisted post synthesis	CH_3OH 1500 μmol g^{-1} within 6 hours	Ru–N/C	56

1(H-bond between O atom of CO_2 and the H atom of H_2O) and HB-2 (H-bond between H atom of H_2O and the N atom of g-C_3N_4) formed when g-C_3N_4 is used as a catalyst. In the photocatalyst with single atom Fe, in addition to the formation of HB-1, CO_2 and H_2O molecules, are coordinated with Fe atom through Fe–C and Fe–O coordination bonds, resulting in a four-coordination structure for Fe (Fig. 14(k)).[55] Fe single atoms dispersed in g-C_3N_4 matrix serve as catalytically active centres and facilitate the activation of CO_2. The reaction barrier for the cleavage of the C–O bond in the COOH radical was reduced from 32.3 kcal mol^{-1} to 15.3 kcal mol^{-1}. The change of catalytically active sites from N atom to single atom Fe accelerates the photochemical processes, thereby enhancing the CO evolution rate from 2.7 μmol g_{cat}^{-1} and 5.1 μmol g_{cat}^{-1}.[55]

Zbořil and coworkers reported ruthenium-based SACs on mpg-C_3N_4 support for the efficient photocatalytic conversion of CO_2 using water as a reductant. Mesoporous C_3N_4, obtained through a silica template assisted pyrolysis of dicyanamide, is used as a matrix for the microwave assisted precipitation and dispersion of Ru single atoms. Catalyst with Ru loading as low as 0.4 wt% yielded methanol as the conversion product, at a yield of 1500 μmol g^{-1} within 6 h. Single atoms of Ru bonded to N/C sites facilitated enhanced electron transfer by virtue of increased charge density around it.[56]

SACs based on g-C_3N_4 support exhibited superior photocatalytic carbon dioxide reduction efficacy compared to conventional metal–semiconductor heterostructures and the developments are summarised below in Table 2.

5.1.2 Photocatalytic water splitting reaction. The energy demand of modern society is fulfilled by the consumption of non-renewable fossil fuels. However, it's fast depletion has necessitated the search for alternative sources of clean and sustainable energy. Hydrogen has thus become the focus of attention and among the myriad ways of generating it, the production and storage of hydrogen fuel through solar light driven water splitting has drawn considerable attention.[57] Water covers nearly 72 percent of the earth's surface and splitting it into H_2 and O_2 in a cost-effective, sustainable, and inexhaustible manner is an attractive proposition to realise the ever increasing energy demands.[58] Water splitting reaction proceeds as two half-reactions namely, photogenerated electrons mediated hydrogen evolution reaction (HER) and photogenerated holes mediated oxygen evolution reaction (OER).[59]

Fujishima and Honda introduced photocatalytic water splitting using TiO_2 photoelectrode under UV light irradiation[60] and since then, numerous studies on H_2 generation from photocatalytic water splitting using a variety of semiconductor photocatalysts have been conducted. The positive Gibbs free energy change (ΔG) of 237 kJ mol^{-1}, associated with the energetics of splitting water into H_2 and O_2, indicates it to be an uphill reaction pathway thermodynamically.[61]

The photocatalytic water splitting proceeds through the three steps (i) exciton generation on the absorbance of energy equivalent to the band gap energy of the semiconductor (ii) separation and migration of photogenerated excitons (e^- and h^+ pairs) to the semiconductor surface and (iii) electrons mediated reduction of H^+ ions to H_2 and holes mediated oxidation of H_2O to O_2 (Fig. 15). Among oxygen evolution and hydrogen evolution reactions (OER and HER), OER is the more complicated half-reaction as it involves the release of $4e^-$ from two H_2O molecules to form the double bond between two oxygen atoms.[62]

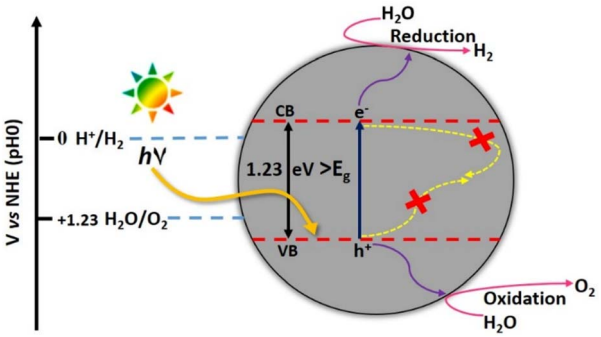

Fig. 15 Schematic diagram of photocatalytic water splitting.

The pre-requisite condition that a semiconductor must satisfy for facilitating the photocatalytic water splitting reaction, is that the valence band (VB) maxima should be more positive than the oxidation potential of water (+1.23 V *vs.* NHE) for OER, while the conduction band (CB) minima should be more negative with respect to the H^+ reduction potential (0 V *vs.* NHE). The formation of water by the recombination of H_2 and O_2 is a detrimental step to catalytic efficiency and should be prevented.[63]

Copolymerising silver tricyanomethanide (AgTCM) along with mesoporous g-C_3N_4 precursors was demonstrated to be advantageous for the synthesis of Ag/mpg-C_3N_4 SACs. The uniform dispersion of Ag species in the semiconductor matrix was realised by inducing negative charges to C and N of C_3N_4 matrix. This approach was demonstrated to be superior to the conventional impregnation-chemical reduction method that often results in the formation of metal nanoparticles. The AgTCM-mpg-CN catalysts with up to 10 wt% of well dispersed Ag species displayed much better performance for Pt assisted photocatalytic water reduction (39.5 μmol H_2 h^{-1} generation for 2 wt% AgTCM compared to a value of 9.8 μmol H_2 h^{-1} for mpg-CN).[17]

Wu *et al.* synthesised highly dispersed, isolated single Pt atoms anchored on g-C_3N_4 (Pt–CN) as a stable photocatalyst for HER. Achieving atomic level dispersions of Pt cocatalyst over g-C_3N_4 enhances the overall photocatalytic HER activity by facilitating the charge transfer as well as by providing an increased number of proton reduction sites. HAADF-STEM analysis revealed that >99% of Pt species are less than 0.2 nm in size corroborating the presence of isolated single atoms of Pt over g-C_3N_4 matrix. The cluster formation was avoided up to a Pt loading of 0.16 wt%. As the Pt loading was increased to 0.38 wt% Pt nanoparticle formation was observed. The Pt–CN with Pt loading of 0.16 wt% exhibited the highest HER activity with a turnover frequency (TOF) of 775 h^{-1}, compared to a TOF of 83 h^{-1} obtained for Pt-NPs-CN (Fig. 16(a and b)). Ultrafast transient absorption (TA) spectroscopy was employed to elucidate the unique role of Pt single atom in enhancing the HER activity. Average recovery life time values, a measure of the extent of

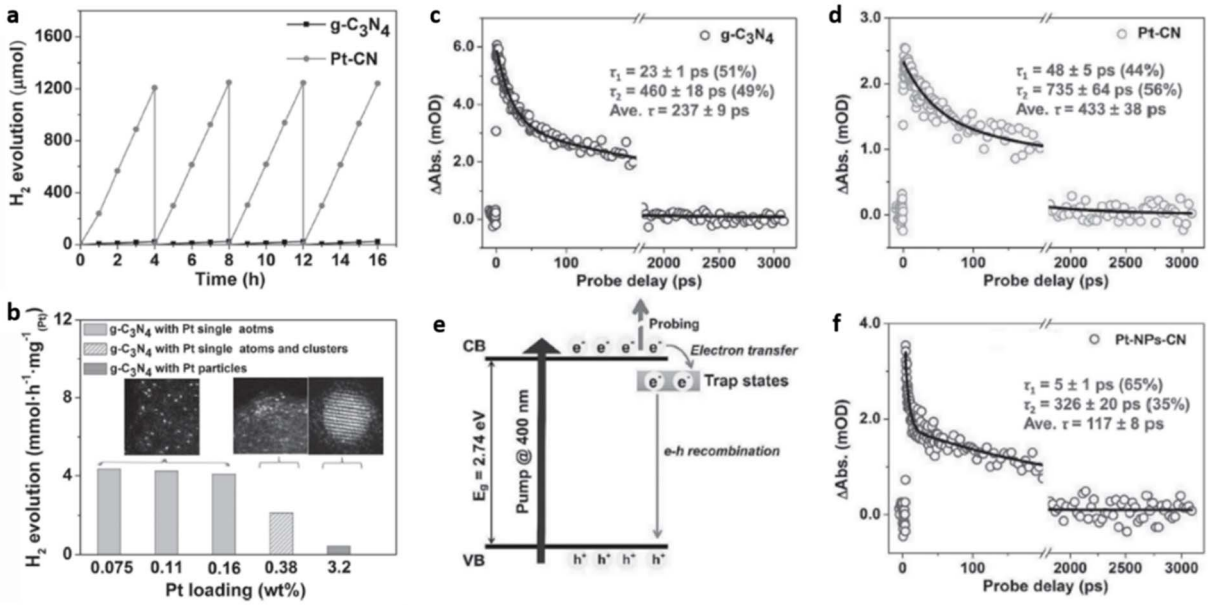

Fig. 16 (a) Photocatalytic H_2 evolution with time for g-C_3N_4 and Pt–CN, (b) photocatalytic H_2 evolution with varying Pt content (normalised per Pt atom), average recovery life time values in mOD (optical density) of (c) g-C_3N_4, (d) Pt–CN, (e) an illustration of the various mechanisms involved, (f) data on TA kinetics for Pt-NPs-CN. Reproduced with permission from ref. 64. Copyright 2016 John Wiley and Sons.

separation of photogenerated excitons, of g-C_3N_4, Pt–CN, and Pt-NPs-CN were found to be ≈237 ps, ≈433 ps, and ≈117 ps respectively (Fig. 16(c and d)). The two-fold and four-fold enhancement in average recovery lifetime for Pt–CN compared to bare g-C_3N_4 and Pt–NPs–CN was attributed to the incorporation of Pt single atoms in g-C_3N_4 framework. The incorporation of isolated single Pt atoms modifies the near band-edge electron trap states of g-C_3N_4 favouring the H^+ reduction process by photogenerated electrons (Fig. 16(e and f)).[64]

Yao *et al.* employed phosphidation followed by atomic-layer-deposition (ALD) to atomically disperse single-site Co atoms on g-C_3N_4 nanosheets (Co_1/PCN) for the photocatalytic HER reaction using triethanolamine (TEOA) as the sacrificial electron donor. The grafting of Co atoms over C_3N_4 nanosheet is achieved through the formation of a covalently bonded Co_1–N_4 structure. Co–N coordination is confirmed with the aid of XANES, EXAFS and XPS. Co_1/PCN exhibited XANES spectrum which is different in shape from that of cobalt oxides (CoO and Co_3O_4) presumably due to Co–C/N coordination. Similarly, a single peak observed at 1.58 Å in Fourier-transformed (FT) k^3-weighted $\chi(k)$ function of Co_1/PCN is close to Co–N bond present in the reference material (CoPc) ruling out the formation of Co–Co, Co–P and Co–O bonds. XPS spectrum of Co_1/PCN further confirmed the existence of Co–N bond with a Co $2p_{3/2}$ peak located at a significantly higher binding energy value of 781.1 eV compared to that of Co–O bond at 780 eV. Additionally, the presence of N vacancies in Co_1/PCN sample is substantiated by XPS analysis as the pyridinic N content observed in the high-resolution N 1s spectra is decreased. To understand the structural configuration of the Co single site in Co_1/PCN, various possible atomic configurations are proposed with specific deposition sites/coordination sites. Accordingly, Co single atoms may be at the corner and center of the six-N cavity (Co–N_2 and Co–N_6 respectively), top of the five-membered ring (Co N_3C_2), and unsaturated coordination site containing four in-plane N atoms (Co N_4). The Co–N bond length value of 2.02 Å obtained from EXAFS spectra ruled out the existence of Co–N_6 structure where the Co–N bond length value should be 2.40 Å. The experimental Co K-edge XANES spectra of Co_1/PCN exactly matched with calculated XANES spectra for Co–N_4 configuration which confirmed the formation of Co_1–N_4 structure (Fig. 17(a–d)). Co_1/PCN with a metal mass loading of 1.0% exhibited an improved H_2 production rate of 10.8 μmol h^{-1} which is approximately an order of magnitude higher than the PCN with a H_2 production rate of 1.0 μmol h^{-1} confirming the unique role of Co_1–N_4 site in improved activity (Fig. 17(e)). The coordinated nitrogen atom present in Co_1–N_4 structure enhanced the electron density around the Co atom. The energy barrier was lowered for the formation of Co hydride intermediate with 3H atom co-adsorbed configuration promoting H–H coupling for accelerated H_2 evolution (Fig. 17(f)).[24]

Wei *et al.* designed HER and OER phosphorus-doped g-C_3N_4 (PCN) photocatalysts with active Co_1-phosphide species. Co_1-phosphide/PCN composite photocatalyst was synthesised by the phosphidation of Co_1 oxo/C_3N_4 composite obtained through the pyrolysis of cobalt precursor and g-C_3N_4. The phosphidation of Co_1-Oxo/C_3N_4 using sodium hypophosphite altered the coordination environment around Co metal atoms from oxygen to phosphorus to form Co_1–P_4 structure. Co_1-phosphide/PCN photocatalyst with a Co mass loading of 0.4% exhibited superior photocatalytic activity than most of the g-C_3N_4 and oxynitride based materials. H_2 production rate of 410.3 μmol h^{-1} g^{-1} and O_2 production rate of 204.6 μmol h^{-1} g^{-1} were achieved without using noble metal co-catalysts, sacrificial reagents, or

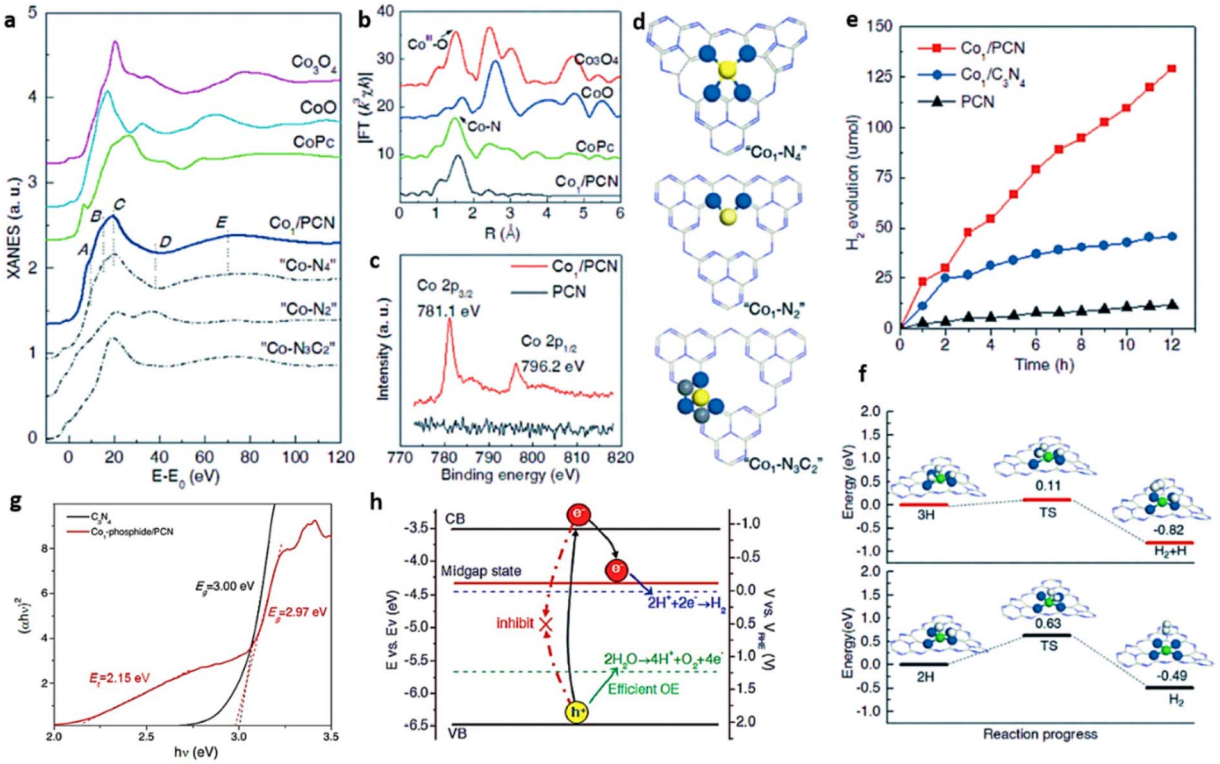

Fig. 17 (a) XANES (Co K-edge) spectra of Co_1/PCN in comparison with standards and possible atomic configurations (b) Fourier spectra of Co_1/PCN in comparison with standards (c) XPS Co 2p spectra of Co_1/PCN and C_3N_4, (d) model structures of "Co_1–N_4", "Co_1–N_2", "Co_1–N_3C_2" with blue, yellow and grey spheres representing N, Co and C atoms, respectively, (e) H_2 evolution with time under simulated solar irradiation, (f) energy diagram of Co_1–N_4 for H_2 evolution on single-sites with the transition state of the reaction TS-(H + H → H_2). N (blue), Co (green) and H (white) spheres. Reproduced with permission from ref. 24. Copyright 2017 John Wiley and Sons. (g) The Tauc plot of the g-C_3N_4 and Co_1 phosphide/PCN catalysts (h) electronic band structure of Co_1-phosphide/PCN catalyst. Reproduced with permission from ref. 65. Copyright 2017 John Wiley and Sons.

other additives and by employing pure water under simulated sunlight. The superior photocatalytic water splitting capacity of Co_1-phosphide/PCN can be attributed to the enhanced light absorption in UV to visible wavelength range and to the introduction of a new mid-gap state within the band structure of Co_1-phosphide/PCN. The band-gap energy (E_g) and transition energy (E_t) from VB to the mid-gap states for Co_1-phosphide/PCN system were estimated to be 2.97 and 2.15 eV, respectively (Fig. 17(g)). Enhanced light harvesting capacity of Co_1-phosphide/PCN was ascribed to the small energy gap between the mid-gap state and VB, favouring the excitation of an electron from VB to the mid-gap states (Fig. 17(h)).[65]

Zhong *et al.* prepared Pt single atoms dispersed on g-C_3N_4 nanosheets (Pt-SA-CN) by a copolymerisation strategy involving melamine, cyanuric acid and 2,4-diamino-6-methyl-1,3,5-triazine. Pt loading less than 0.3 wt% has been realised by the wet impregnation method using H_2PtCl_6. The immobilisation and atomic level dispersion of Pt atoms over g-C_3N_4 was established through Pt–N coordination bonds. Pt-SA-CN catalyst with a Pt loading of 0.20 wt% displayed enhanced H_2 production of 4875.0 μmol g^{-1} in 4 h. A correlation is established with the Pt single atom size on the metal loading and its corresponding photocatalytic activity. The size of Pt atoms in Pt-SA-CN with 0.2 and 0.3 wt% Pt loading was found to be 0.21 and 0.5 nm respectively and a subsequent reduction in the H_2 evolution was observed with increasing Pt size.[66]

Liu *et al.* successfully developed Pt^{II}–C_3N_4 single atom catalyst for efficient photocatalytic water splitting by employing high-valence metal single-atom confinement strategy. Pt^{II}–C_3N_4 exhibited H_2 evolution at the rate of 140 μmol g^{-1} h^{-1}, which is ~10 times higher compared to that of Pt NP–C_3N_4 (15 μmol g^{-1} h^{-1}). Upon visible light irradiation, the Pt^{II}–C_3N_4 system shows a quantum efficiency of 1.5% at 420 nm. Anchoring Pt^{II} single atoms on g-C_3N_4 matrix *via* Pt^{II}–N bond formation facilitated higher absorption of visible light and effectively suppressed exciton recombination. The E_g values for g-C_3N_4, Pt^{II}–C_3N_4, Pt nanoparticle-C_3N_4, derived from Tauc plot were found to be 2.77, 2.72, and 2.6 eV respectively. The flat band potential of Pt^{II}–C_3N_4 (−1.01 V *vs.* RHE) is appreciably shifted to a more positive value compared to Pt NP–C_3N_4 (−1.25 V) and g-C_3N_4 (−1.44 V) (Fig. 18(a)). Ultraviolet photoelectron spectra (UPS) revealed that the VB maxima for Pt^{II}–C_3N_4 were shifted downward by ~0.27 V compared to g-C_3N_4, which may be due to the hybridisation of 5d orbital of Pt^{II} & 2p orbital of N atom present in the g-C_3N_4 framework (Fig. 18(b)). The modified electronic band structure of Pt^{II}–C_3N_4 effectively promoted the overall photocatalytic water splitting reaction (Fig. 18(c)). Band structure calculations based on the first principles were performed to

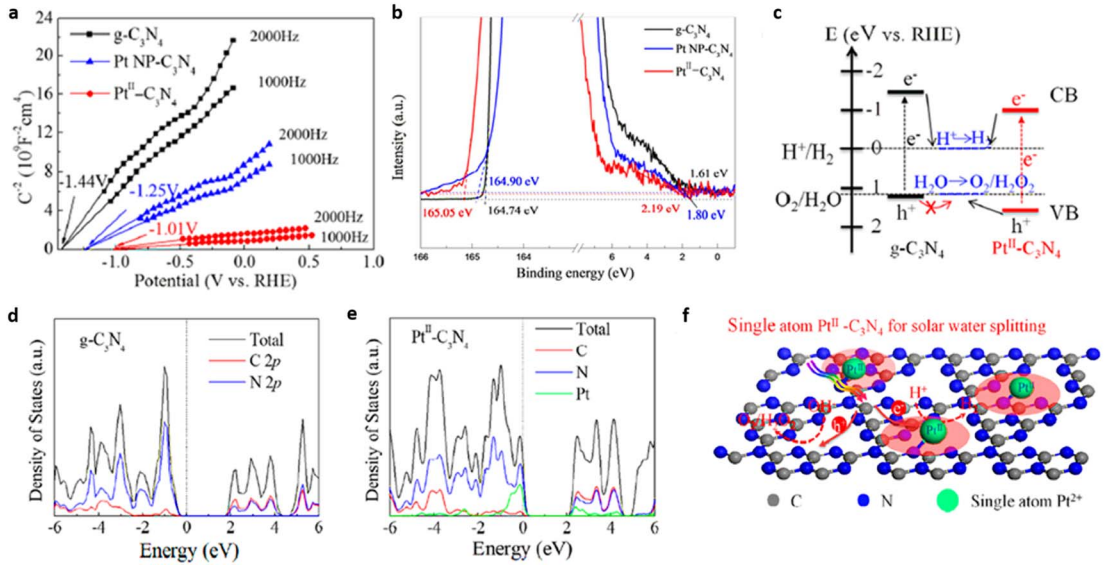

Fig. 18 (a) Mott–Schottky plot of Pt^{II}–C_3N_4 in comparison with g-C_3N_4 and Pt NP–C_3N_4, (b) UPS spectra of g-C_3N_4, Pt^{II}–C_3N_4 & Pt NP-C_3N_4, (c) schematic band structure alignment, DOS of (d) g-C_3N_4 and (e) Pt^{II}–C_3N_4, (f) mechanistic pathways (schematic) of the photocatalytic water splitting by Pt^{II}–C_3N_4. Reproduced with permission from ref. 23. Copyright 2018 American Chemical Society.

understand the correlation between the electronic structure of Pt^{II}–C_3N_4 photocatalyst and its improved charge carrier transfer kinetics. Electron density of state (DOS) analysis on g-C_3N_4 (Fig. 18(d)) revealed that the Fermi level (middle of the band gap) is devoid of mobile electrons but an intersection of the valence band and Fermi level is evident in the DOS of Pt^{II}–C_3N_4 photocatalyst (Fig. 18(e)). In addition, the strong electrophilic nature of the valence band of Pt^{II}–C_3N_4 formed through the hybridisation of Pt^{II} 5d and N 2p orbitals promotes the electron transfer to CB catalysing HER and leaving behind the holes at the VB to facilitate OER (Fig. 18(f)).[23]

g-C_3N_4 functionalised with amino groups at the edges were utilised to develop atomically dispersed Fe SACs for solar driven photocatalytic hydrogen generation. The spontaneous coordination of dicyandiamidine nitrate with Fe ions led to the formation of porous crimpled g-C_3N_4. The incorporation of Fe single atoms altered the band and electron structures enabling faster charge transfer kinetics realising hydrogen evolution rate of 3390 μmol h^{-1} g^{-1} at a quantum efficiency of 6.89% at 420 nm.[67]

A promising approach to optimise catalytically active sites is by tuning the reactive metal–support interaction (RMSI) which is conventionally realised by the high-temperature reactions (T > 550 °C) of reducible oxides. Guo *et al.* reported strong RMSI in Pt single atom containing g-C_3N_4 obtained by the *in situ* photocatalytic reduction of (H_2PtCl_6) at liquid nitrogen temperatures. The strong RMSI, induced by rich N vacancies in C_3N_4 provided a record single atom coverage density of 0.35 mg m^{-2} leading to 174.5 mmol g^{-1} h^{-1} of hydrogen evolution. Simulation studies indicated that RMSI stabilises single atoms of Pt through chemical bonds with two coordinated C (C_2C) formed by the N vacancies.[25]

A photoactive, single atom cobalt loaded g-C_3N_4 catalyst obtained through a supramolecular polycondensation process based on dicyandiamide is demonstrated for photocatalytic hydrogen evolution using TEOA as a sacrificial agent and 3 wt% Pt as cocatalyst. The synthesised Co@g-C_3N_4 composite exhibited improved photocatalytic hydrogen evolution at a rate of 2481 μmol h^{-1} g^{-1}. The incorporation of Co single atoms strengthened the reducing capability of the conduction band (CB) electrons due to a shift in the CB edge minima to a more negative value compared to that of g-C_3N_4 (0.83 V and −0.95 V *vs.* SCE respectively).[19]

Employing 2D confinement strategy, Quan *et al.* developed Pt single atoms confined on carbon nitride photocatalyst with ultrahigh Pt loading of 8.7 wt% for the H_2 evolution reaction. The photocatalytic performance of the synthesised samples was dependent on the location of the Pt atoms at either the surface or within the inner layers of g-C_3N_4 (Fig. 19(a–d)). The interlayer interactions altered the electronic structure by delocalising the charge density of the Pt atom which in turn facilitated the adsorption of protons and caused the reduction of the energy barrier for HER (Fig. 19(e and f)). The developed photocatalyst exhibited H2 evolution rate of 22.65 mmol g^{-1} h^{-1} with an apparent quantum yield (AQY) of 22.5% at 420 nm.[68]

C_3N_4 hollow spheres dispersed with single atoms of Cu were developed by a molecular assembly involving melamine (ME) and cyanuric acid (CA) with copper nitrate. Single atoms of Cu were either embedded within g-C_3N_4 sheets (Cu1@HCNS) or dispersed on its surface (Cu1/HCNS) as Cu_1N_3 species through Cu–N coordination. The copper single atoms embedded within the sheets were more effective in promoting interfacial charge transfer as well as tuning the electronic band structure. The Cu1@/HCNS exhibited improved HER activity (using 3 wt% Pt cocatalyst) with AQY of 7.1% which is 1.6, 2.7 35.4 times higher compared to Cu1/HCNS, HCNS, and bulk PCN respectively.[69]

Pd single atoms dispersed on ultrathin nanosheets of cyano group rich C_3N_4 (Pd/D_N-UCN), obtained by the copolymerisation of urea and NH_4Cl followed by wet impregnation was

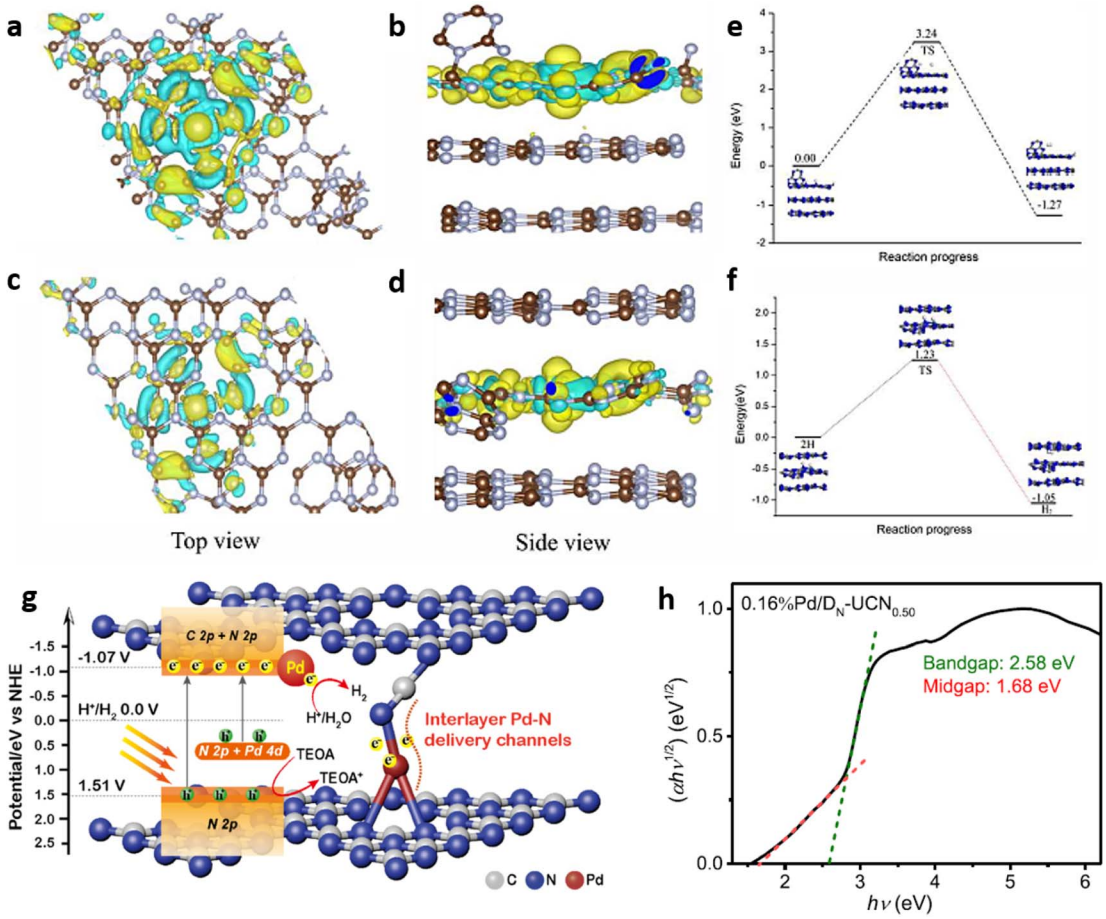

Fig. 19 Charge distributions (top and side view) on Pt single atoms (a and b) on C_3N_4 surface (SA-Pt/g-C_3N_4-Sur), (c and d) within the inner layer of C_3N_4 (SA-Pt/g-C_3N_4-In), energy profiles of HER over Pt atom (e) on C_3N_4 surface and (f) within the inner layer of C_3N_4. Reproduced with permission from ref. 68. Copyright 2020 Elsevier.[68] (g) Mechanism of charge separation, transfer and H_2 evolution in the photocatalyst 0.16%Pd/D_N-$UCN_{0.50}$, (h) Kubelka–Munk plot of 0.16%Pd/$D_N$$UCN_{0.50}$. Reproduced with permission from ref. 70. Copyright 2022 American Chemical Society.

demonstrated to possess improved photoinduced hydrogen evolution rate. Pd atom coordinated with one N of the cyano group and two sp^2 hybridised N atoms of the adjacent g-C_3N_4 layers was firmly stabilised in g-C_3N_4 interlayers inducing a mid-gap state in the band structure (Fig. 19(g and h)). SACs with 0.16 wt% of Pd (0.16%Pd/$D_N$$UCN_{0.50}$) produced noticeably higher hydrogen evolution rate, compared to Pd nanoparticle coordinated C_3N_4 based catalysts, at an apparent quantum yield of 15.8% at 400 nm light irradiation.[70]

A two-component synergistic photocatalyst with atomic dispersions of Co and nanoparticles of Pt–Co alloy on C_3N_4 nanosheets exhibited hydrogen production at the rate of 300.9 mmol h^{-1} g^{-1} during overall water splitting (OWS). The single Co atoms efficiently activated HER while the alloy particles of PtCo were active sites for OER. The synergistic combination enabled high atom utilisation and the presence of different reaction centres permitted the transport of reaction intermediates with efficient exciton separation.[71] The salient features of the reported works are summarised in Table 3.

5.1.3 Photocatalytic nitrogen fixation. Despite constituting more than 78% of the atmosphere, the dinitrogen molecule (N_2) is not directly utilised by most organisms owing to its attributes like strong N≡N bond with a bond energy of −941 kJ mol^{-1}, high ionisation potential, and non-polarity. Since nitrogen is indispensable for the sustenance of life, living organisms take N_2 in the form of ammonia or nitrates. This is mostly realised through 3 important pathways of biological nitrogen fixation by azobacteria, high energy nitrogen fixation by geochemical processes such as lightning and industrial nitrogen fixation through the well-known Haber–Bosch process. However, the contributions from biological and geochemical processes are extremely low and most of the demand is met from the energy intensive Haber–Bosch process that operates at both high temperatures (400–500 °C) and pressures (150–250 atm). Moreover, in the industrial synthesis of ammonia, 1.87 tons of CO_2 is released for every ton of NH_3 produced. Photocatalytic nitrogen fixation thus assumes larger significance and is hence pursued widely as a sustainable process for ammonia production in an environmentally benign manner.[72]

Photocatalytic nitrogen fixation proceeds by the rate determining step of N≡N bond cleavage through electron mediated activation at the reducing sites of semiconductor

Table 3 Summary of g-C_3N_4 SACs for photocatalytic water splitting

System	Single atom & loading	Synthesis method	HER rate	Coordination site or structure & oxidation state	Ref.
AgTCM-mpg-CN	Ag 2 wt%	Template assisted direct synthesis	39.5 μmol H_2 h^{-1}	C/N, +1	17
Pt-CN	Pt 0.16 wt%	Post synthesis-photo chemical reduction	318 μmol h^{-1}	N/C	64
Co_1/PCN	Co 1 wt%	Post synthesis-atomic layer deposition (ALD)	10.8 μmol h^{-1}	Co_1–N_4	24
Co-phosphide/PCN	Co 0.4 wt%	Post synthesis	H_2 410.3 μmol h^{-1} g^{-1}, O_2 204.6 μmol h^{-1} g^{-1}	Co_1–P_4	65
Pt-SA-CN	Pt 0.11 wt%	Post synthesis	4875.0 μmol g^{-1} in 4 h	Nitrogen	66
Pt/C_3N_4	Pt	Post synthesis-electrostatic deposition	140 μmol g^{-1} h^{-1}	Nitrogen, +2	23
Fe@g-C_3N_4	Fe 0.5 at%	Supramolecular preorganisation assisted direct synthesis	3390 μmol h^{-1} g^{-1}	Nitrogen, +2	67
Pt-SA-CN	Pt 1.72 wt%	Post synthesis -photo chemical reduction	3.02 mmol g^{-1} h^{-1}	Nitrogen, carbon	25
Co@g-C_3N_4	Co 0.305 wt%	Supramolecular preorganisation assisted direct synthesis	2481 μmol h^{-1} g^{-1}	Nitrogen oxidation state between +3 & +2	19
SA-Pt/g-C_3N_4	Pt 8.7 wt%	Post synthesis-photo chemical reduction	22 650 μmol g^{-1} h^{-1}	Pt–N_4 oxidation state <+2	68
Cu1/HCNS	Cu	Post synthesis	3261 μmol g^{-1} h^{-1}	Cu_1N_3, +1	69
Pd/D_N-UCN	Pd 0.16%	Post synthesis-Photochemical reduction	441.6 μmol in 4 h	Pd–N_3, +2	70
Co_{SAs}/PtCo@CNN	Co	Post synthesis-photo chemical reduction	300.9 μmol h^{-1} g^{-1}	Co(II)N_x, +2	71

photocatalysts. However, till date no reported photocatalyst possesses the appropriate electronic band structure to facilitate the one-electron transfer reduction of N_2. The defect type activation centers utilised by most semiconductors are not adequate to make the process efficient and commercially viable. In this context single atom photocatalysts by virtue of their abundant, defect-free surface-active sites for effective N_2 adsorption and activation, offer promise for efficient photocatalytic N_2 fixation.[13]

In one of the earlier works on 'single atom like' copper-doped g-C_3N_4 containing Cu(I)–N active sites, the charge density differences were used to simulate the electron transfer process between Cu^+ and N^2 molecules leading to electron depletion and accumulation on Cu^+ and N_2 respectively. Further successive electron transfer processes lead to NH^{4+} through high-energy intermediates like $-N_2^-$, $-N_2H$, or HN=NH, *etc.* DOS results confirmed the delocalisation of σg2p orbital (highest occupied molecular orbital (HOMO) of N_2) upon adsorption on Cu centres as well as the shifting of πg*2p orbital (lowest unoccupied molecular orbital (LUMO) of N_2) near to Fermi level. This led to a decrease in the electron states of the LUMO orbital from 6.9 eV for free N_2 to 1.0 eV for M_S–Cu–CN facilitating the activation of N_2 molecule and subsequent H^+ attack leading to the formation of NH_4^+.[73]

Wang and co-workers demonstrated, by first-principles calculations, the potential use of a metal-free photocatalyst with boron (B) single atoms decorated on g-C_3N_4 (B/g-C_3N_4) for efficient N_2 reduction. The sp^3 hybridised B with three half-filled and one empty orbital form two B–N bonds with g-C_3N_4 matrix (utilising two of the half-filled sp^3 orbitals), facilitating the atomic level distribution of B atoms. During the N_2 fixation process, one half-filled and the empty sp^3 orbitals remaining in the B atom interact with N_2 through the "acceptance–donation" process facilitating active sites for N_2 adsorption and subsequent reduction Fig. 20(a–f).[74] The high binding energies of −1.04 and −1.28 eV can thus be realised in B/g-C_3N_4 SACs through side-on and end-on bonding with N_2 respectively. Photoreduction of N_2 to NH_3 over B/g-C_3N_4 catalyst may follow any of the three typical mechanisms of distal, alternating, and enzymatic mechanisms (Fig. 20(g)). The low onset potential of 0.20 V obtained by B/g-C_3N_4 SACs supported the enzymatic pathway for N_2 reduction Fig. 20(h–j). This theoretical study also predicted low formation energy for B/g-C_3N_4 SACs, enhanced light absorption in the visible and infrared region, and high thermal stability up to1000K enabling sustainable NH_3 production through photocatalytic N_2 fixation. The B/g-C_3N_4 SACs showed enhanced visible light and infrared light absorbance, high thermal stability and ease of preparation enabling them to be effective for photocatalytic nitrogen reduction.[74]

Mo single-atoms on *in situ* formed g-C_3N_4 were prepared by the calcination of urea and $Na_2MoO_4 \cdot 2H_2O$ by establishing coordination with two N donors of g-C_3N_4 to form MoN_2 structures. The active sites for N_2 chemisorption provided by low-coordinated Mo centers in 3-Mo-PCN catalyst, with a metal loading of 0.346 wt%, facilitated high photocatalytic activity towards NH_3 evolution in pure water at a rate of 50.9 μmol g_{cat}^{-1}

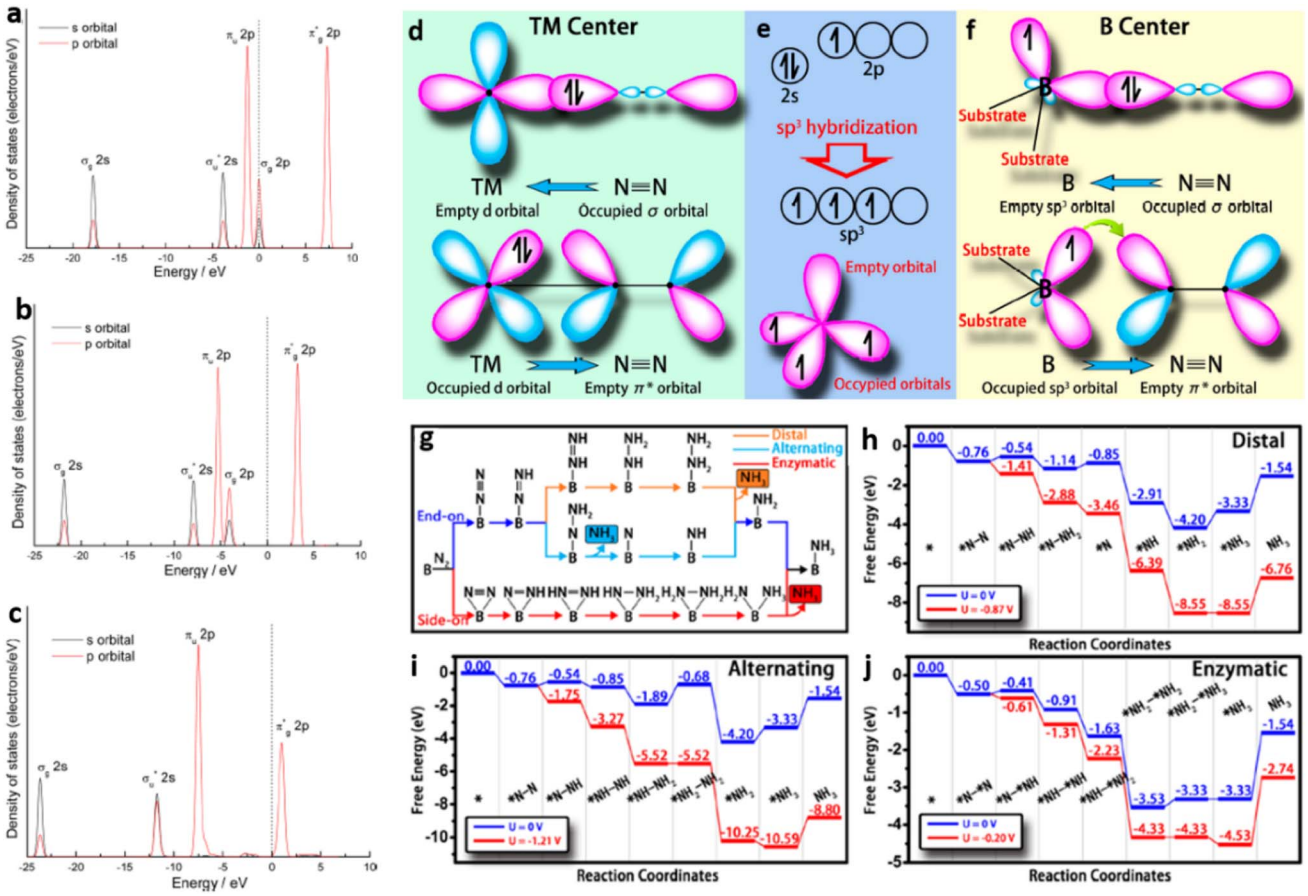

Fig. 20 (a) DOS of free N_2 molecule, (b) N_2 molecule adsorbed on pure GCN and (c) N_2 molecule adsorbed on M_S-Cu-CN. Reproduced with permission from ref. 73. Copyright 2017 American Chemical Society. (d) Illustration of N_2 bonding to transition metals, (e) formation of sp^3 orbitals in B atom, (f) N_2 binding to the B atom stabilised on g-C_3N_4, (g) distal, alternating, and enzymatic mechanisms for N_2 reduction, free energy diagrams for (h) distal, (i) alternating, (j) enzymatic pathways for N_2 reduction on B/g-C_3N_4. Reproduced with permission from ref. 74. Copyright 2018 American Chemical Society.

h^{-1}. The use of ethanol as an electron scavenger increased the rate to 830 μmol g_{cat}^{-1} h^{-1} at a quantum efficiency of 0.70% at 400 nm. DFT calculations supplemented experimental observations and predicted that coordinatively unsaturated Mo single atom centres strongly adsorb N_2 through an end-on configuration resulting in the elongation of the N≡N bond from 1.11 Å to 1.15 Å. The photogenerated electrons are thus transferred to the weakened N≡N bond providing efficient N_2 reduction at ambient conditions.[75]

Chen and co-workers successfully synthesised multifunctional single atom cobalt loaded g-C_3N_4 (Co@g-C_3N_4) photocatalyst for N_2 fixation reaction in a methanol/H_2O medium. Co@g-C_3N_4-1 with a metal loading of 0.305 wt% selectively reduced N_2 to NH_3 at the rate of 50.2 μmol h^{-1} and without any by-products like hydrazine hydrate and nitrates. In comparison bulk g-C_3N_4 and g-C_3N_4 obtained through the supramolecular route exhibited a production rate of 8.2 μmol h^{-1} and 19.5 μmol h^{-1} respectively.[19]

Single atoms of ruthenium (Ru) dispersed on the g-C_3N_4 surface were obtained by the pyrolysis of a precursor mix containing dicyandiamide and $RuCl_3 \cdot xH_2O$ in an argon atmosphere. SAC containing 0.05 atomic % of Ru exhibited photocatalytic nitrogen fixation at the rate of 2.26 mg L^{-1} g_{cat}^{-1} h^{-1} in pure water and without hole-scavengers. The rate was 1.5 times greater than that of pure g-C_3N_4 (Ru–CCN-0). The improved catalytic activity was ascribed to the high N_2 adsorption capacity combined with increased light absorbance in the spectral region of 200 to 800 nm owing to a redshift in the absorption edge of Ru–CCN-0.05 compared to that of Ru–CCN-0.[76] The SAC systems demonstrated for photocatalytic nitrogen fixation are listed in Table 4.

5.1.4 Photocatalytic environmental remediation. One of the potential methods that is perceived for wastewater and pollutant treatment is photocatalysis.[77] Irradiation of a photocatalyst with energy more than or equal to its band gap energy excites valence band (VB) electrons to the conduction band (CB) creating electron–hole pairs. The excitons then migrate to the catalyst surface without recombination, engaging in various redox reactions with H_2O, O_2, and organic contaminants leading to pollutant degradation.[78] During the process (Fig. 21), electrons from CB react with molecular oxygen forming superoxide radical ($O_2^{\bullet -}$) which is an extremely powerful oxidising

Table 4 Summary of g-C_3N_4 SACs for photocatalytic nitrogen fixation

System	Single atom & loading	Synthesis method	NH_3 evolution rate	Coordination site or structure & oxidation state	Ref.
M_S-Cu-CN	Cu 0.25 wt%	Direct synthesis	8.8 mg L^{-1} h^{-1} g_{cat}^{-1}	Cu(I)–N, +1	73
B/g-C_3N_4	B	DFT study	—	Nitrogen	74
Mo–PCN	Mo 0.346 wt%	Template free direct synthesis	50.9 μmol g_{cat}^{-1} h^{-1} in pure water & without using electron scavenger, 830 μmol g_{cat}^{-1} h^{-1} using ethanol as electron scavenger	Mo–N_2, oxidation state in between 0 & +4	75
Co@g-C_3N_4	Co 0.305 wt%	Chemical reduction assisted Post synthesis	50.2 μmol h^{-1}	Nitrogen, +2	19
Ru–CCN	Ru 0.34 wt%	Direct synthesis	2.26 mg L^{-1} g_{cat}^{-1} h^{-1} in pure water	Nitrogen	76

agent. On the other hand, holes from VB react with hydroxide ions (OH^-) or water (H_2O) forming hydroxyl radical ($OH^{\bullet}$) which is also an important non-selective oxidising agent.[79] The superoxide and hydroxide radicals degrade a variety of organic pollutants like dyes, antibiotics, *etc.* into CO_2, H_2O and inorganic ions. The feasibility of these redox reactions depends on the CB and VB positions of the photocatalyst. The necessary condition for oxidation warrants the VB potential to be more positive than the oxidation potential of the surface reaction to be accomplished.[80] Similarly reduction reaction proceeds when the CB potential is more negative with respect to the reduction potential of the surface reaction. These redox reactions form basic pathways for every photocatalytic environmental remediation.[81]

Reactions:

$$\text{photocatalyst} + h\nu \rightarrow e^- + h^+$$

$$h^+ + H_2O \rightarrow H^+ + OH^{\bullet}$$

$$O_2 + e^- \rightarrow O_2^{-\bullet}$$

$$O_2^{-\bullet} + H^+ \rightarrow HO_2$$

$$2HO_2 + 2H^+ \rightarrow H_2O_2 + 2OH^{\bullet}$$

$$OH^{\bullet}/H_2O_2/O_2^{-\bullet} + \text{pollutant} \rightarrow \text{degradation products}$$

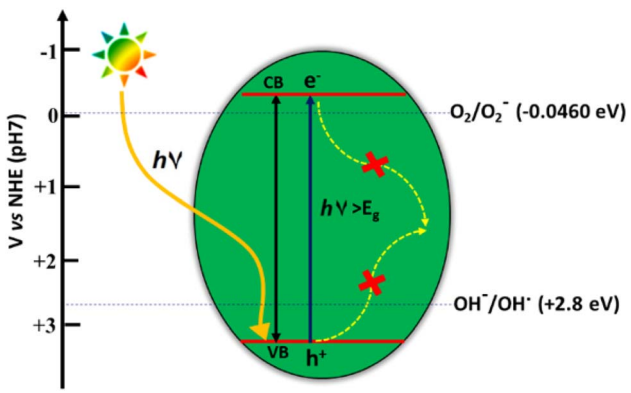

Fig. 21 Schematic of the photocatalytic process.

Zhao and co-workers developed single-atom Ag supported mpg-C_3N_4 (Ag/mpg-C_3N_4) by a method involving the co-condensation of dicyandiamide and silver tricyanomethanide (AgTCM) through a silica templating approach. The photocatalytic activity was demonstrated by peroxymonosulfate (PMS) mediated bisphenol A (BPA) degradation by 10% Ag/mpg-C_3N_4 catalyst, where in 100% activity was achieved within 1 h of visible light illumination. The improved catalytic activity was realised due to the synergistic effect of atomically dispersing Ag atoms on high surface area g-C_3N_4 leading to a reduction in band gap from 2.5 eV (mpg-C_3N_4) to 2.09 eV (10% Ag/mpg-C_3N_4).[82]

Single Pt atom catalyst on g-C_3N_4 described earlier[66] for photocatalytic HER has been successfully employed for the selective photocatalytic NO oxidation to NO_3^-. The oxidation proceeded progressively over 150 min with a removal ratio of 96.2% for Pt 0.2-SA-CN. In comparison, pure g-C_3N_4 and g-C_3N_4 with 0.1 and 0.3 wt% of single atom Pt (Pt 0.1-SA-CN, Pt 0.3-SA-CN) exhibited 78.9%, 84.7%, and 92.0% of NO removal respectively. Additionally, g-C_3N_4 with photo-deposited Pt nanoclusters of 4 nm size (Pt 0.2-VL-CN) samples exhibited 90.9% NO removal. The negative shift of CB and the increased generation of ROS (h^+, $^{\bullet}OH$ or $^{\bullet}O_2^-$) expedited the photo-induced catalytic activity.[66]

Liu *et al.* synthesised Ag loaded SAC on ultrathin g-C_3N_4 sheets (AgTCM/UCN) *via* co-polymerisation of dicyandiamide and silver tricyanomethanide (AgTCM) in the presence of NH_4Cl. AgTCM/UCN with 1 wt% Ag loading photocatalytically degraded 86.4% of sulfamethazine (SMT) in the presence of PMS during the 21 min of visible light irradiation. Aberration corrected HAADF-STEM analysis revealed that Ag single atoms of ~0.25 nm diameter were dispersed over the g-C_3N_4 matrix. The photodegradation of SMT was shown to proceed *via* any of the three pathways involving sulfonamide bond cleavage, SO_2 extrusion, and aniline oxidation.[83]

g-C_3N_4 based catalyst containing Fe single atoms and ultra-small clusters with Fe(II)–N_x active sites was prepared by pyrolysing a precursor mix containing melamine (MA) and iron imidazole complex (Fe-ICC). High Fe content up to 18.2 wt% was realised in a composition (I-FeN_x/g-C_3N_4-5) with an optimum ratio of MA/Fe-ICC to be 5. DFT calculations revealed that Fe single atoms preferably occupy the interlayers of g-C_3N_4 *via* bonding with nitrogen located above and below it and with

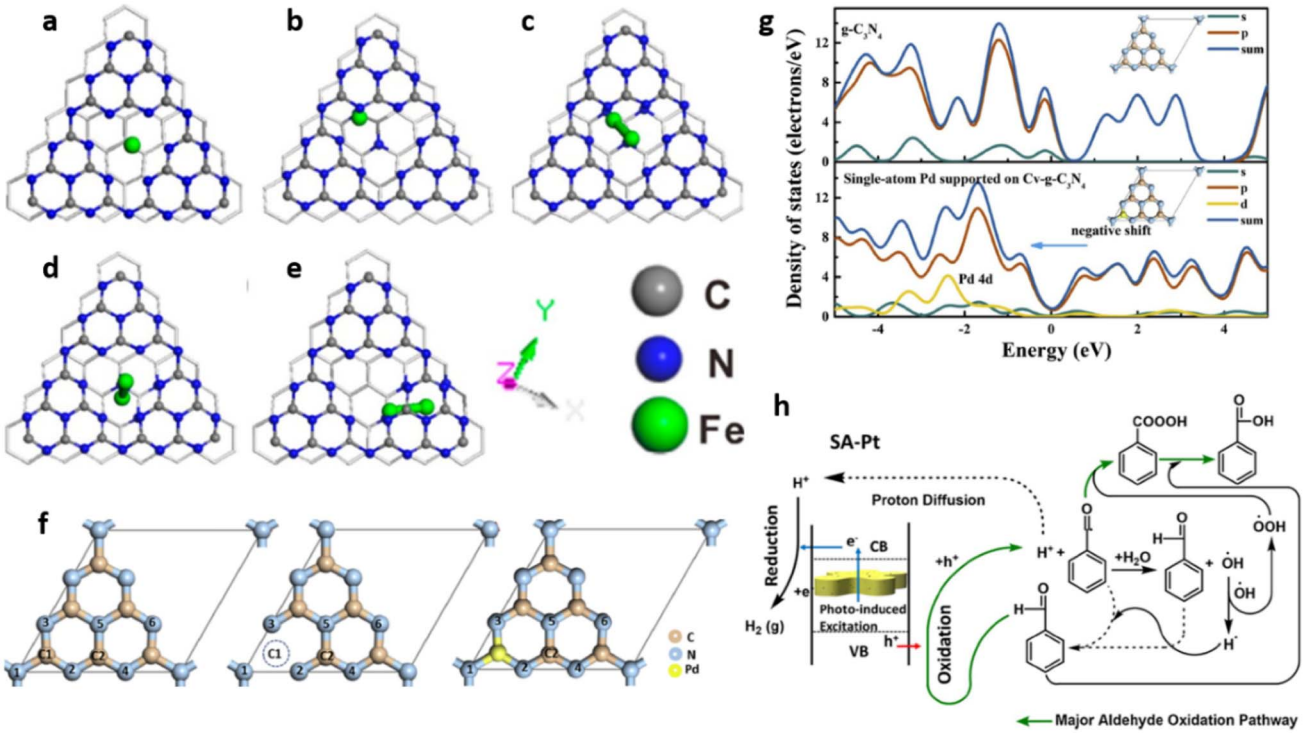

Fig. 22 Structures depicting possible locations for Fe single atom and cluster over g-C_3N_4; Fe single atom in (a) 6-fold cavity centre, (b) interlayer. Fe cluster sites in the interlayer (c), Site 1, (d) Site 2 (e) Site 3. Reproduced with permission from ref. 84. Copyright 2018 American Chemical Society. (f) The carbon vacancies and single atom site of Pd in g-C_3N_4 and (g) corresponding DOS. Reproduced with permission from ref. 90. Copyright 2021 Elsevier. (h) Schematic diagram representing the mechanism of benzaldehyde oxidation and associated H_2 evolution with photoinduced electron and hole transfer. Reproduced with permission from ref. 91. Copyright 2021 Elsevier.

a binding energy (BE) of −3.92 eV compared to a low BE of −2.77 eV in Fe atom at the center of the 6-fold cavity. Additionally, ultra-small Fe clusters (Fe_2 dimer as a model) are stable only at the interlayers with a BE of −2.50 to −2.83 eV. A high binding energy value (−3.92 eV) further revealed that Fe atoms remain isolated preferably over its cluster formation (Fig. 22(a–d)). The developed I-FeN_x/g-C_3N_4-5 catalyst are shown to exhibit rapid photo-fenton degradation (100% within 15 min at pH 7) of organic contaminants like methylene blue (MB), methyl orange (MO), rhodamine B (RhB), and phenol. The degradation process proceeds *via* the rapid generation of $HO^{\bullet}$ radicals from H_2O_2 at the Fe(II)–N_x active sites.[84]

Silver single-atom catalyst based on amorphous g-C_3N_4 was developed by Tong *et al.* through a supramolecular gel formation involving precursors of melamine and silver nitrate. The thermal polymerisation yielded a high density of silver atoms that selectively broke H-bonds of layered g-C_3N_4 inducing amorphisation. An optimised MA composition with Ag atomic ratio of 11.6% exhibited a narrow E_g value of 2.54 eV, improved visible light absorption, and accelerated charge transfer leading to the effective degradation of naproxen (NPX).[85]

Ammonia-assisted selective catalytic reduction (SCR-NH_3) is the conventional methodology to reduce NO emissions but suffers from the disadvantages of particulate formation, hardware corrosion and direct release of unreacted NH_3. Direct reduction of NO with CO, without NH_3 injection, is an environmentally benign approach to circumvent the disadvantages of the SCR-NH_3 process. Ni Single atoms on monolayer g- C_3N_4 (Ni-g-C_3N_4) were demonstrated to be an efficient and stable catalyst for the photocatalytic reduction of NO to N_2 at about 350 °C and space velocity of 15 000 h^{-1}. Ni-g-C_3N_4 adsorbed multiple numbers of NO molecules simultaneously and the N_2O intermediate was rapidly reduced to N_2 with an energy barrier of 0.50 eV. The oxidised catalyst was regenerated rapidly by CO through OR2 mechanism with an energy barrier of 0.16 eV.[86]

Zeng *et al.* employed an *in situ* growth process to develop single-atom cobalt based polymeric C_3N_4 (pCN) catalyst and demonstrated its catalytic efficacy for the degradation of oxytetracycline (OTC). The anchoring of single-atom Co on pCN was realised through Co–O and Co–N covalent bond formation. The catalyst with the cobalt loading of 1.28% (Co(1.28%)-pCN) displayed an excellent rate constant of 0.038 min^{-1} for OTC degradation which was nearly 4 times more than that of pCN.[87]

Gawande *et al.* evaluated the photodegradation of pharmaceutical pollutants utilising single-atom Ni dispersed on C_3N_4 nanosheets (saNi-*n*C_3N_4). The pyrrolic N mediated Ni–N coordination confirmed by spectrometric analyses, is responsible for the improved interfacial charge transfer *via* N–Ni–N bridges. Gemfibrozil, a model pollutant was degraded up to 75.9% in 30 minutes of visible light irradiation. The degradation efficiency of saNi-*n*C_3N_4 was better than the widely used TiO_2 photocatalyst.[88]

Chen *et al.* prepared single atoms of various transition metals (SA-TM, TM = Cr, Mn, Fe, Co, Cu) on g-C_3N_4 containing

Table 5 Summary of g-C_3N_4 SACs for photocatalytic environmental remediation

System	Single atom & loading	Synthesis method	Catalytic application, degradation % or rate & time	Coordination site or structure & oxidation state	Ref.
Ag/mpg-C_3N_4	Ag	Template assisted direct synthesis	PMS mediated bisphenol A degradation, 100%, 60 min	Nitrogen, 0	82
Pt–C_3N_4	Pt 0.2 wt%	Post synthesis reduction under an inert atmosphere	NO oxidation, 96.2%, 150 min	Nitrogen, +2	66
AgTCM/UCN	Ag 1 wt%	Template assisted direct synthesis	PMS mediated sulfamethazine degradation, 86.4%, 21 min	Nitrogen	83
I-FeN_x/g-C_3N_4	Fe 18.2 wt%	Template free direct synthesis	Photo-fenton degradation; methylene blue, methyl orange, rhodamine B, & phenol, 100%, 15 min	Fe–N_x, +2 (64.3%), +3 (35.7%)	84
MA (Ag/g-C_3N_4)	Ag 12.0%, (atomic ratio)	Direct synthesis	Degradation of naproxen, 1.92 × 10^{-1} min^{-1}	Carbon	85
Ni/g-C_3N_4	Ni	Post synthesis	Photocatalytic degradation of NO with 100% yield rate-15000 h^{-1}	Nitrogen	86
Co-pCN	Co 1.28%	Template free direct synthesis	Degradation of oxytetracycline, 75.7%, 40 min	Nitrogen, oxygen	87
saNi-*n*C_3N_4	Ni 8 wt%	Post synthesis- microwave treatment	Degradation of gemfibrozil, 75.9%, 30 min	Ni–N_x, +2	88
SA-TM/PN-g-C_3N_4	TM = Cr, Mn, Fe, Co, Cu	Direct synthesis	Degradation of bisphenol A, SA-Cr/PN-g-C_3N_4 exhibited highest activity: 98.8%, 70 min	Cr(II)–N_4, +2	89
Pd-Cv-CN	Pd	Post synthesis-photochemical reduction	NO oxidation, 56.3%, 30 min	Pd–N_3, +2	90
Pt/g-C_3N_4 (SA-Pt)	Pt 0.35 wt%	Post synthesis-photochemical reduction	Benzaldehyde oxidation: 70.8 mmol g_{Pt}^{-1} & H_2 production: 34 mmol g_{Pt}^{-1} in 3h	Nitrogen	91

abundant pyrrolic N (PN-g-C_3N_4) through an aqueous self-assembly process involving the precursor mix of xanthine, cyanuric acid, melamine. Transition metal ions were adsorbed on the self-assembled MCAXT through binding sites provided by imidazole groups and subsequent calcination in N_2 atmosphere formed SA-TM/PN-g-C_3N_4 catalysts that exhibited excellent performances for Heterogeneous Fenton-Like Reaction (HFLR). Cr dispersed SACs were found effective for visible light induced photocatalytic degradation of bisphenol A, in the pH range of 3.0–11.0 with outstanding cyclic stability. The enhanced charge carrier production as well as their separation along with the cycling of the Cr^{3+}/Cr^{2+} couple boosted the HFLR performance. Theoretical studies predicted that Cr(II)–N_4 active sites with its structure analogous to metalloporphyrin mimicked peroxidase nanozymes for the effective homolysis of peroxide O–O in H_2O_2.[89]

Wang *et al.* designed Pd SACs (Pd-Cv-CN) for photocatalytic NO conversion, by anchoring Pd atoms on carbon vacancies present in modified g-C_3N_4 (Cv-CN) *via* a photo-reduction process. The theoretical simulation predicted the possibility of isolated Pd–N_3 active site formation. The DOS plot of Pd-Cv-CN revealed a negative shift in the peak positions on the negative energy side due to the modification of 4d orbital of Pd (Fig. 22(g and f)). This has led to an increase in band levels and a decrease in the band gap for Pd-Cv-CN compared to that of g-C_3N_4. The developed Pd-Cv-CN effected 56.3% of NO conversion in 30 min illumination time, while pristine CN and Pd nano-Cv-CN converted only 12.7% and 46.0% of NO respectively.[90]

Polymeric g-C_3N_4 containing Pt dispersions in the form of single atoms SA-Pt (0.2 nm), nanoclusters CL-Pt (1 nm), and nanoparticles NP1–Pt and NP2–Pt (4 and 7 nm diameter respectively) was demonstrated for the simultaneous benzaldehyde oxidation to benzoic acid and photocatalytic hydrogen production. The catalytic efficiency was highest for Pt single atoms compared to nanoclusters and nanoparticles of Pt. For SA-Pt catalyst, the benzaldehyde conversion and H_2 evolution reached a value of 70.8 mmol g_{Pt}^{-1} and 34 mmol g_{Pt}^{-1} respectively in 3 h. Upon visible light excitation, SA-Pt catalyst promoted the transfer of photo-generated holes for benzaldehyde oxidation while CB electrons promoted the proton reduction leading to H_2 evolution (Fig. 22 (h)).[91] The SACs explored for photocatalytic environmental remediation with the applications demonstrated are presented in Table 5.

5.1.5 Photocatalytic H_2O_2 synthesis *via* oxygen reduction reaction (ORR). Semiconductor mediated photocatalytic H_2O_2 synthesis from oxygen and water is an attractive and environmentally benign process.[92] To realise appreciable efficiencies, both the $2e^-$ oxygen reduction reaction (ORR, eqn (1)) and $2e^-$ water oxidation reaction (WOR, eqn (2)) need to be catalysed.[93] However, the $2e^-$ WOR process occurs at high oxidation potentials (1.76 V *versus* NHE, normalised hydrogen electrode) owing to thermodynamic considerations and is therefore difficult by photocatalytic approaches.[94,95]

H_2O_2, being an excellent hole scavenging material is prone to oxidation at these potential values.[96] On the other hand, photosynthesis of H_2O_2 by $2e^-$ ORR pathway has been hitherto achieved albeit with a low efficiency of less than 8% for non-sacrificial H_2O_2 production eqn (3).[97] In order to enhance the efficiency of non-sacrificial H_2O_2 synthesis, concurrent promotion of both $2e^-$ ORR and $4e^-$ WOR eqn (4) is necessary.[98] O_2, generated *in situ* as a product of $4e^-$ WOR, is also a reactant for the $2e^-$ ORR and hence the rapid consumption of O_2 by ORR will accelerate the kinetics of WOR.[96] Therefore, the presence of active sites, in SACs with O_2 selectivity for the $2e^-$ ORR promotes artificial H_2O_2 synthesis *via* photocatalysis.[99]

$$2e^- \text{ ORR } O_2 + 2H^+ + 2e^- \rightarrow H_2O_2 \text{ (0.695 V } \textit{versus} \text{ NHE)} \quad (1)$$

$$2e^- \text{ WOR } 2H_2O \rightarrow H_2O_2 + 2H^+ + 2e^- \text{ (1.76 V } \textit{versus} \text{ NHE)} \quad (2)$$

$$\text{Non-sacrificial } H_2O_2 \text{ production } 2H_2O + O_2 \rightarrow 2H_2O_2 \quad (3)$$

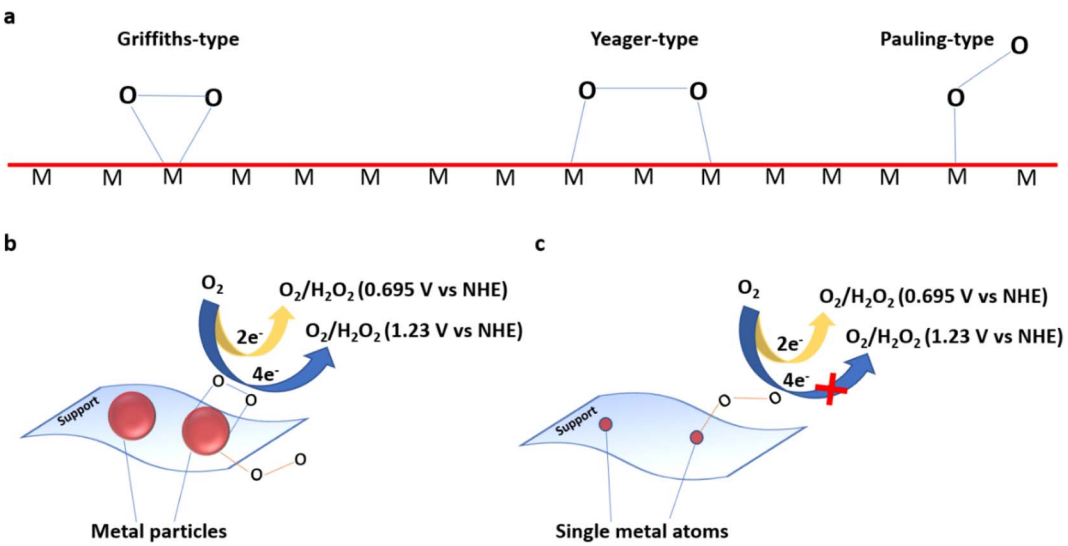

Fig. 23 (a) O_2 adsorption modes on a metal surface, ORR pathways on (b) metal nanoparticles and (c) single metal atom sites.

$$4e^- \text{ WOR } 2H_2O + 4h^+ \rightarrow O_2 + 4H^+ \text{ (1.23 V } \textit{versus} \text{ NHE)} \quad (4)$$

$$4e^- \text{ ORR } O_2 + 4H^+ + 4e^- \rightarrow 2H_2O \text{ (1.23 V } \textit{versus} \text{ NHE)} \quad (5)$$

The adsorption of O_2 on the metal surface occurs *via* end on Pauling-type and side on Griffiths and Yeager types (side-on) (Fig. 23(a)).[99,100] The Pauling type end-on O_2 adsorption minimises O–O bond fission and the 4e− ORR eqn (5) can be suppressed.[101] End-on and side-on adsorption of O_2 molecules occur on metal particles leading to O–O bond splitting. In SACs O_2 molecules adsorb on atomically dispersed sites through the end-on type, reducing the breaking of O–O bond (Fig. 23(b)).[102–106]

Single atom photocatalysts (SAPCs) with metals of d^{10} electronic configuration favour efficient charge separation through the formation of intermediate bands and form reactive centres with a high density of charge carriers.[56,107] Such SACs are considered as potential catalysts for the photocatalytic H_2O_2 synthesis through the $2e^-$ ORR.[108] Ohno *et al.* developed Sb dispersed g-C_3N_4 (Sb-SAPC) where single atoms of Sb enabled the photoreduction of O_2 through the 2 electron ORR, generating H_2O_2 at the rate of 12.4 mg L^{-1} in 120 min. The N atoms of C_3N_4 surrounding the Sb single atoms, on the other hand, enhanced the kinetics of water oxidation. The apparent quantum yield (ΦAQY, 17.6% at 420 nm) and conversion efficiency (solar to chemical), 0.61% were better than the best performing photocatalysts reported. The analysis of the products of photocatalysis suggested that the H_2O_2 generation was through the two-electron ORR pathway.[100,101]

In another noteworthy contribution, SACs with single atoms of (Fe, Ni, Co, In and Sn) were prepared through a wet-chemical synthetic route followed by thermal treatment. Invoking time dependent DFT (TDDFT) calculations, it was demonstrated that the inclusion of metal single atoms on melem units significantly altered the charge separation process. The adsorption energy ($E_{ab}X$) of melem was similar for single atoms of In and Sn suggesting lesser tendencies for charge recombination while Fe (2+ and 3+), Co and Ni (2+) increased the $E_{ab}X$ due to dominant recombination. Moreover, iso surfaces created due to the incorporation of In and Sn single atoms favoured the adsorption of oxygen accelerating oxygen reduction at the sites.[101] Table 6 lists the reported systems for photocatalytic H_2O_2 synthesis.

5.2 Thermal catalysis

Catalysts play a vital role in numerous industrial processes for the synthesis of chemicals.[102] The development of efficient catalysts that demonstrate product selectivity in appreciable yields is an essential requirement for the bulk synthesis of chemicals.[103] Consequently, the majority of industrial catalysts are based on noble metals on appropriate supports as they are capable of activating important molecules like CO, H_2, O_2, H_2O, *etc.* Nevertheless, the widespread practical application of noble metal-based catalysts in bulk manufacture is significantly hampered by the scarcity and exorbitant cost of precious metals.[104,105] Transition metal catalysed organic reactions, which can be classified under thermal catalysis are now actively employed in the fields of pharmaceutical synthesis, materials development, and biological sciences.[106] However, such catalyst systems suffer from shortcomings like poor selectivity, low utilisation efficiency, minimal catalytically active species and unwanted side reactions during their practical application.[107] SACs are currently receiving significant attention by virtue of their high conversion efficiency in thermal catalysis for organic transformations.[56] The beneficial aspects of both homogeneous and heterogeneous catalysts are integrated in SACs.[108]

SACs are shown to catalyse organic reactions efficiently owing to the presence of unsaturated metal centres, unique electronic structure and 100% atom utilisation efficiency. Electron transfer between metal single atoms and the coordinating atoms of the support induces positive charges (partial or full) on the metal atoms of SACs and offers an enhanced rate of conversion of substrate into product. Furthermore, metal atoms are spatially isolated in SACs due to which the reactive intermediates of the catalytic reactions are adsorbed differently to prevent undesirable side reactions for which the presence of adjacent metal sites is mandatory.[109] Development of SACs and ADMCs provides the most ideal strategy for creating cost-effective catalysts for organic transformations (Fig. 24).[110]

Single-site [Pd] mpg-C_3N_4 heterogeneous catalyst obtained by silica templated thermal condensation of cyanamide, was demonstrated as the first stable single-site heterogeneous catalyst for the hydrogenation of alkynes and nitroarenes. Atomically dispersed [Pd] mpg-C_3N_4 with 0.5 wt% of Pd and with an average particle size of 0.3–0.4 nm displayed excellent product selectivity (>90%) and significantly improved catalytic activity over conventional nanoparticle based heterogeneous catalysts. For 1-hexyne hydrogenation, the reaction rate at 30 °C and 1 bar pressure was 3 orders higher in magnitude than the conventional catalysts like Ag, Au, and CeO_2. The performance was further improved at 60 °C and 2 bar pressure where 100% selectivity for 1-hexene was realised. The [Pd] mpg-C_3N_4 single-site catalyst also displayed excellent chemoselectivity and

Table 6 Summary of g-C_3N_4 SACs for photocatalytic H_2O_2 synthesis *via* oxygen reduction reaction (ORR)

System	Single atom & loading	Synthesis method	H_2O_2 production rate & time	Coordination site or structure & oxidation state	Ref.
Sb-SAPC	Sb 10.9 wt%	Template free direct synthesis	12.4 mg L^{-1}, 120 min	Nitrogen, +3	100
M-SAPC	Fe, Ni, In, Co, Sn, 0.5–0.6 mmol per 1 g catalyst	Template free direct synthesis	In-SAPC & Sn-SAPC exhibited superior H_2O_2 production	Nitrogen, oxidation state of Fe is between II & III, and for Co, Ni, In & Sn is close to II, II, III & IV respectively	101

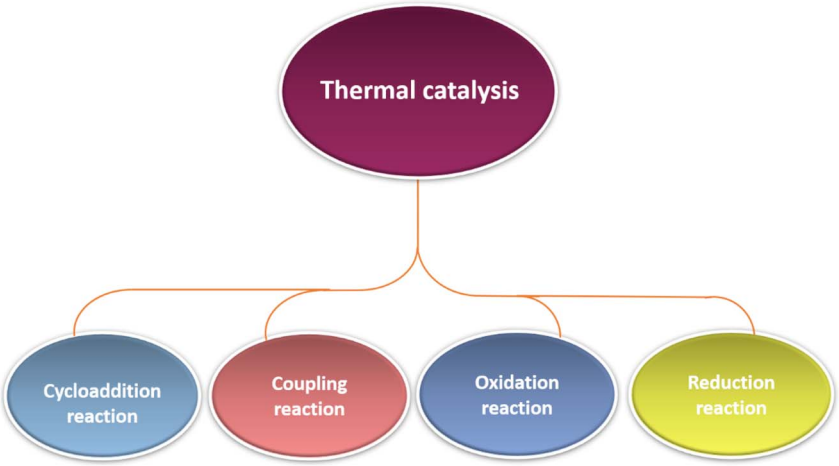

Fig. 24 Various reactions catalysed by g-C_3N_4 based SACs in the area of thermal catalysis.

stereoselectivity (*cis*/*trans* ratio >20) as has been shown in the hydrogenation reaction of 3-hexyne to *cis*-3-hexene and 2-methyl-3-butyn-2-ol to 2-methyl-3-buten-2-ol. [Pd] mpg-C_3N_4 catalyst is also capable of catalysing the hydrogenation reaction of nitrobenzene to aniline. The improved catalytic activity of [Pd] mpg-C_3N_4 single-site catalyst was rationalised by DFT calculations which confirmed hydrogen activation and alkyne adsorption on single-site Pd atoms. g-C_3N_4 as a matrix facilitates the homogeneous distribution of Pd atoms, promotes H_2 activation and inhibits CO poisoning of metal active sites.[4]

Dual functional catalyst Ag/mpg-C_3N_4 SAC as mentioned earlier for photocatalytic HER, was also demonstrated to be very effective for alkyne hydrogenation with near 100% selectivity for the conversion of 1-hexyne at a reaction rate exceeding 100 $mol_{alkyne}\ h^{-1}\ mol_{Ag}{}^{-1}$ at 303 K and 10 bar compared to the rates of 60 and 40 $mol_{alkyne}\ h^{-1}\ mol_{Ag}{}^{-1}$ for catalysts prepared by impregnation–reduction and spray deposition respectively.[17]

SAC with extremely low loading (519 ppm) of Au on mpg-C_3N_4 (Au_1/mpg-C_3N_4) demonstrated high turnover frequency (50 200 h^{-1}) for the oxidation of silane in the presence of water and oxygen. The coordination of Au^I with three N atoms or C atoms in the repeating tri-*s*-triazine units of g-C_3N_4 provides atomic level dispersion of highly active Au^I. In comparison with Au_1/mpg-C_3N_4, $HAuCl_4$ and Au nanoparticles showed inferior performance for the oxidation of diphenylmethylsilane with water. Au_1/mpg-C_3N_4 also displayed excellent catalytic activity for the oxidation of various organosilanes with greater than 95% yield. It was proposed that the Au^I single atoms activate the Si–H bond through oxidative insertion forming a Si–Au^{III}–H intermediate which further reacted with H_2O to form silanol and H_2 with the regeneration of the Au^I active sites (Fig. 25(a)).[26]

Single atom palladium catalysts (Pd-ECN) on C_3N_4, obtained by the thermal exfoliation, is demonstrated to outperform conventional catalysts (homogeneous and nanoparticle based heterogeneous systems) for the Suzuki coupling between bromobenzene and phenylboronic acid pinacol ester. The ECN matrix not only provides appropriate coordination of Pd atoms in catalyst formation but also participates in the catalytic process through adsorption, stabilisation and activation of substrates and intermediates. The Pd-ECN SACs displayed 63% conversion with 90% selectivity towards biphenyl. The rate of product formation increased linearly from 0.22 to 0.57 mmol product min^{-1} $g_{cat}{}^{-1}$ with the loading of Pd (from 0.25 to 0.66 wt%). However, as the concentration is increased to 1.25 wt%, the reaction rate is decreased to 0.32 mmol product min^{-1} $g_{cat}{}^{-1}$. The turnover frequency (TOF) varied between 558 and 549 h^{-1}, respectively, for (0.25 and 0.66 wt% Pd) but was reduced significantly to 163 h^{-1} as Pd content increased to 1.25 wt%.[111] The electron density around the N-sites of ECN matrix activated bromobenzene while the lattice flexibility of ECN facilitated multiple coordination patterns for enhanced stability. This mechanism is further verified by performing the reaction with single atom Pd on mesoporous C_3N_4 (Pd-MCN) which displayed less activity albeit high stability and selectivity. The mediocre catalytic performance of Pd-MCN is ascribed to the enhanced structural disorder present in MCN relative to ECN.[111]

Guo *et al.* designed SACs with neighbouring Pt and Ru (Pt–Ru) monomers in N deficient g-C_3N_4 (PtRuSA-CN620) by photoreduction at liquid nitrogen temperature. Conventionally the structure of g-C_3N_4 contains a C atom coordinated to three N atoms while a few N atoms (denoted as N_{2C} sites) are coordinated only with two C atoms. The creation of nitrogen vacancy leads to the formation of two neighbouring two-coordinated C atoms (denoted as C_{2C} sites) in the g-C_3N_4 framework. The structure simulation revealed that the creation of N vacancies in g-C_3N_4 increases the largest vertical dimension from 4.20 Å to 5.47 Å which facilitates the incorporation of Pt and Ru atoms of diameter 2.2 Å as two neighbouring monomers. During photoreduction, the photogenerated electrons concentrate on the N vacancies of CN, facilitating the reduction of noble metal ions into monomer atoms.[8]

Due to the electronegativity difference, C_{2C} sites are positively charged while N2C sites are negatively charged. During the photoreduction of Pt and Ru metal ions to Pt–Ru monomers, negatively charged $[PtCl_6]^{2-}$ ions preferentially get

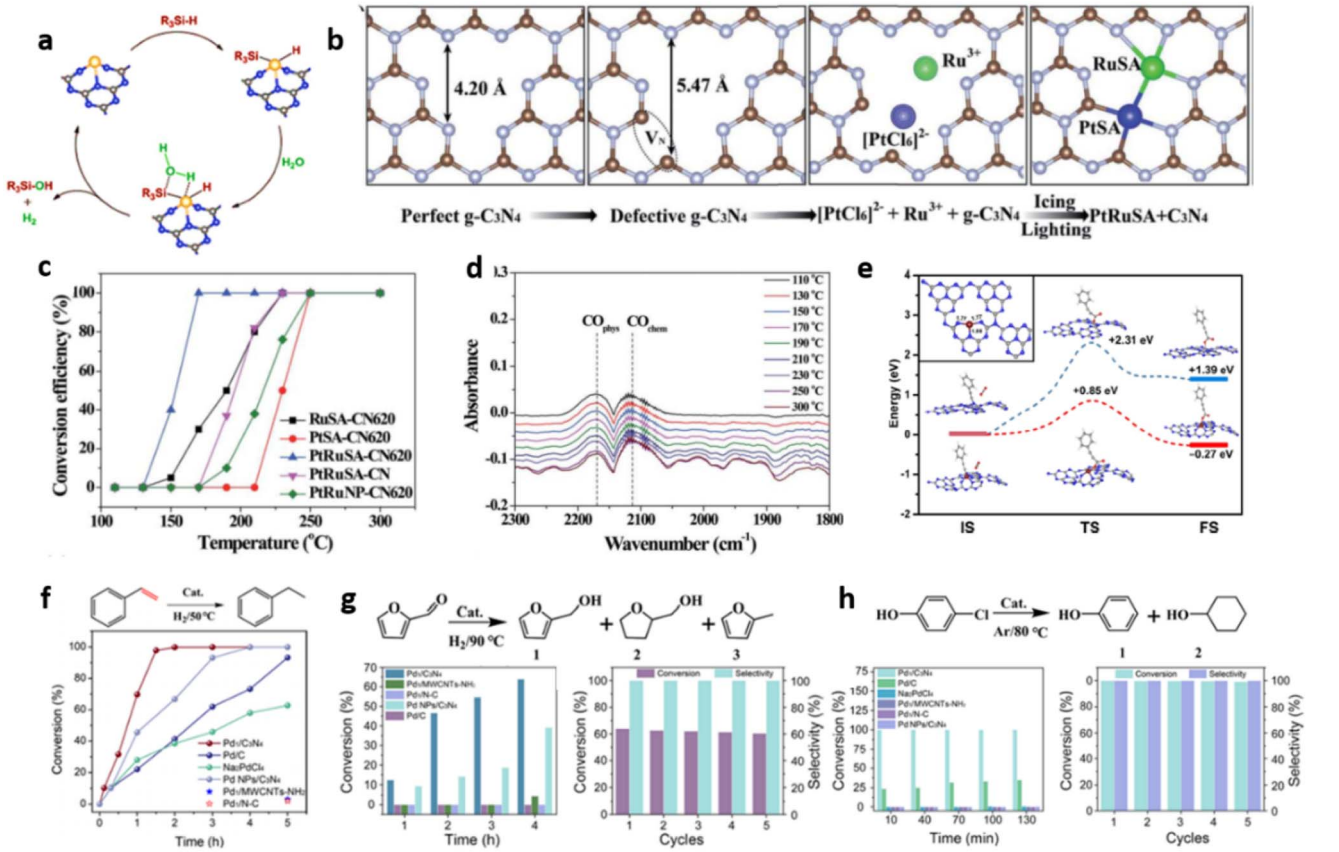

Fig. 25 (a) The plausible mechanism of $Au_1/mpg\text{-}C_3N_4$ catalysed water-based silane oxidation. Reproduced with permission from ref. 26. Copyright 2017 John Wiley and Sons. (b) Scheme for the synthesis of PtRuSA-CN620 by the photoreduction method, (c) CO conversion over synthesised catalysts at CO concentration of 1 vol%, (d) CO oxidation monitored by *in situ* infrared spectra using PtRuSA–CN620. Reproduced from ref. 8. Under the terms of Creative Commons License, published 2019 Royal Society of Chemistry. (e) Reaction profile for CO_2 insertion over Cu–CN-8.0 & CN catalysts (inset: the optimised structure of Cu–CN-8.0). Reproduced with permission from ref. 112. Copyright 2020 American Chemical Society. Reaction scheme and catalytic performance of Pd_1/C_3N_4 for (f) hydrogenation of styrene, (g) hydrogenation of furfural (h) hydrodechlorination of 4-chlorophenol. Reproduced with permission from ref. 113. Copyright 2020 American Chemical Society.

adsorbed on C_{2C} sites while the positively charged Ru^{3+} ions are adsorbed on N_{2C} sites to form C–Pt–Ru–N coordination in PtRuSA-CN620 (Fig. 25(b)). Pt–Ru monomers with the above coordination structure contains two Pt–C, one Pt–N and three Ru–N bonds with a more negative adsorption energy (E_{ads}) value of −9.40 eV. They are found to be more stable compared to Pt–Pt/Ru–Ru monomers, Pt–Ru monomers with C–Ru–Pt–N, N–Pt–Ru–N coordination structure, and isolated Pt/Ru atoms.[8]

The PtRuSA-CN620 catalyst with 0.45 wt% Ru and 0.51 wt% Pt exhibited 100% CO conversion into CO_2 at the lowest conversion temperature of 150 °C by Eley–Rideal (E–R) mechanism through preferential adsorption of O_2 followed by activation on the catalyst surface (Fig. 25(c)). The feeble IR absorption peaks for CO molecule at 2171 and 2111 cm^{-1} in the temperature range of 110 to 300 °C, ruled out the possibility of Langmuir–Hinshelwood (L–H) mechanistic pathway for CO oxidation in which both CO and O_2 adsorption take place on catalyst surface (Fig. 25(d)).[8]

Photocatalytic non-oxygenative coupling of amines to imines employing H_2O as an oxidant is a prospective approach, by virtue of its ease of handling, for the bulk synthesis of imines. Single atoms of copper (0.85 wt%) embedded within $g\text{-}C_3N_4$ sheets (Cu1@HCNS) exhibited superior benzylamine oxidation (BOR) to imine at the rate of 10 583 μmol g^{-1} h^{-1} and with 96% selectivity. The catalytic activity was found to be 3.8 and 2.5 times better than Cu single atoms on the surface of $g\text{-}C_3N_4$ (Cu1/HCNS) and hollow C_3N_4 spheres comprising of C_3N_4 nanosheets (HCNS) respectively. The BOR activity of Cu1@HCNS was much higher than the most performing precious metal Pt/MOF and was comparable with commonly employed Ni/CdS catalyst which is toxic and photocorrosive.[69]

$mpg\text{-}C_3N_4$ containing single-atom Cu (Cu–CN-*x*) up to 26.6 wt% was synthesized by a one-pot two step strategy using urea and $CuCl_2$. The first heat treatment at 180 °C led to the coordination and precondensation between urea derived N-containing species and Cu^{2+} ions through the formation of Cu–N bond. Subsequent calcination at 550 °C resulted in the confinement of Cu single atom in CN matrix through the replacement of one C atom and coordination with three N atoms. The synthesized Cu–CN-*x* (*x* indicates the Cu wt%) displayed excellent catalytic activity towards carboxylation of terminal alkynes, utilizing atmospheric CO_2. Cu–CN-8.0 aided

the carboxylation of phenylacetylene with 97% yield of phenylpropiolic acid and with highest TOF of 9.7 h^{-1}. The mechanism involves the formation of an alkynyl carboxylic intermediate *via* the addition of deprotonated phenylacetylene to CO_2. The reaction further proceeds through CO_2 insertion in copper acetylide to result in Cu(I)–propiolate complexes, leading to phenylpropiolic acid. DFT calculations supplemented the experimental observations as the above addition reaction on Cu–CN is exothermic in nature with a reaction energy of −0.27 eV and an energy barrier of +0.85 eV. On the contrary, pure CN was shown to be catalytically inactive due to the high endothermic reaction energy of +1.39 eV coupled with a high activation energy barrier of +2.31 eV (Fig. 25(e)).[112]

Atomically dispersed palladium on g-C_3N_4 (Pd_1/C_3N_4) was synthesised by confining them into the six-fold cavity *via* N-coordination employing a spatial confinement-reduction strategy involving urea and Na_2PdCl_4. The catalytic performance of Pd_1/C_3N_4 SACs with Pd loading of 0.18 wt% was demonstrated for various selective hydrogenation reactions and the hydrodechlorination reaction of 4-chlorophenol. Pd_1/C_3N_4 exhibited a high TOF value of 834 h^{-1} with 98% conversion for hydrogenating styrene to ethylbenzene. In comparison catalysts with nanoparticles of Pd (Pd NPs/C_3N_4) up to 11 wt% metal loading displayed the TOF values of 476 h^{-1} only. Alternatively, g-C_3N_4, single atom Pd dispersed in MWCNTs-NH_2 (Pd-MWCNTs-NH_2, 0.32 wt%) and nitrogen doped carbon (Pd_1/N–C, 0.82 wt%) showed negligible activity. The control sample of commercial Pd/C (5 wt%) and Na_2PdCl_4 salt exhibited TOF values of 333 h^{-1}.

Pd_1/C_3N_4 was also utilised for selectively hydrogenating furfural using H_2O as a solvent at 90 °C temperature and 1 atm H_2 pressure. Pd_1/C_3N_4 exhibited 64% conversion of furfural to furfuryl alcohol with a TOF of 146 h^{-1} and 99% product selectivity. In comparison Pd NPs/C_3N_4 exhibited only 39% of conversion with a TOF of 67 h^{-1} and 99% product selectivity. Furthermore, Pd1/C_3N_4 was also utilised for the hydrodechlorination of 4-chlorophenol at 80 °C using ammonium formate as the source of hydrogen. 99% conversion and 99% product selectivity towards phenol were achieved within 10 min and with an exceptionally high TOF of 13 333 h^{-1}. In contrast, Pd NPs/C_3N_4, Pd_1/MWCNTs-NH_2, Na_2PdCl_4 salt, and Pd_1/N–C yielded no product while Pd/C exhibited 35% of conversion along with 99% selectivity and a TOF value of 1527 h^{-1}.[113]

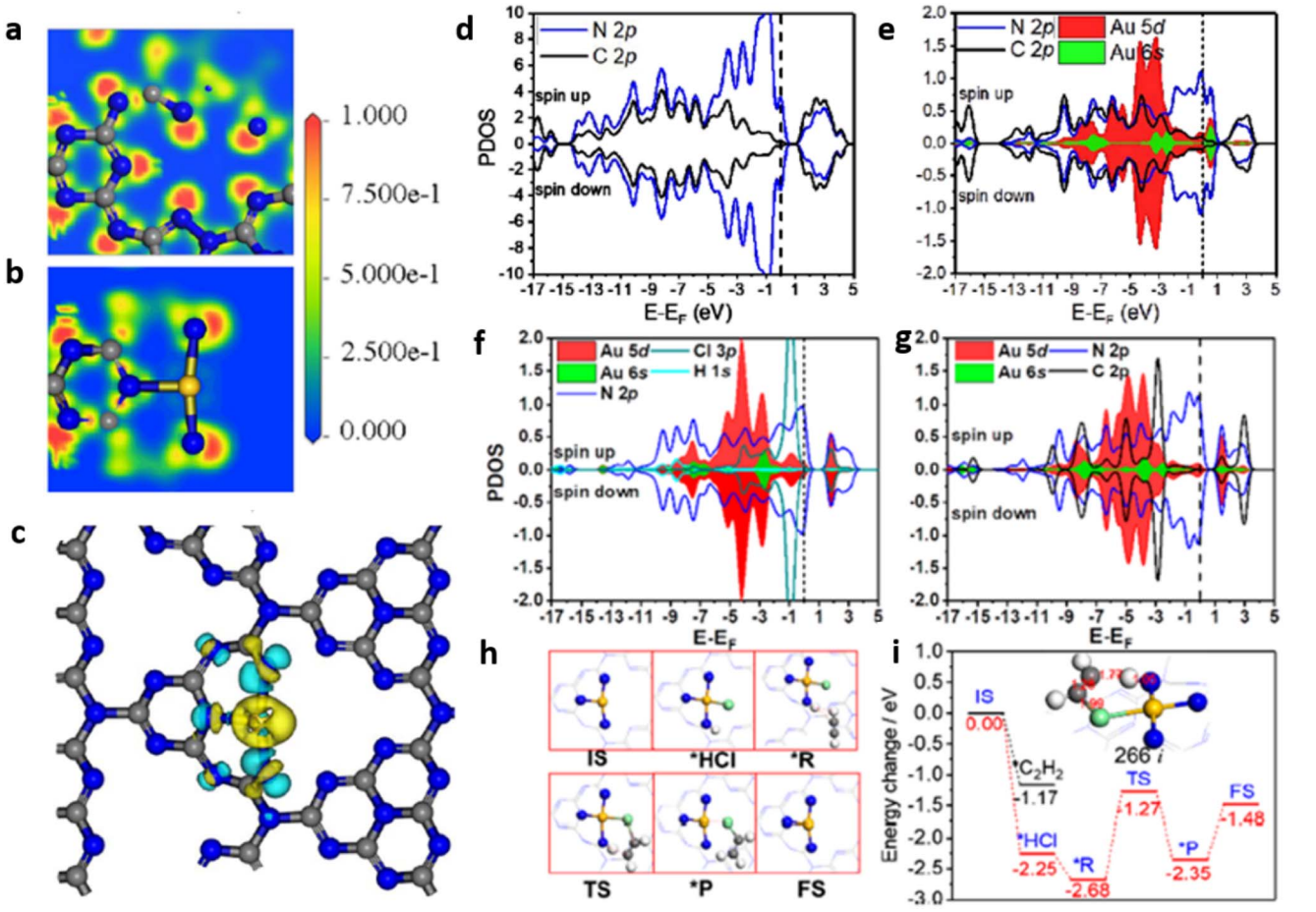

Fig. 26 ELF (electron localisation function) map of (a) carbon deficient g-C_3N_4, (b) Au_1/g-C_3N_4, (c) charge density differences for Au atom on the g-C_3N_4 (yellow for increasing and blue for decreasing charge density), PDOS of (d) one carbon deficient g-C_3N_4, (e) Au_1/g-C_3N_4, Au_1/g-C_3N_4 (f) after HCl adsorption (g) after acetylene adsorption, (h) reaction species configuration, (i) the reaction profile of hydrochlorination reaction on Au_1/g-C_3N_4 catalyst. Reproduced with permission from ref. 114. Copyright 2020 American Chemical Society.

Au SACs ($Au_1/g\text{-}C_3N_4$) synthesised by the calcination of $HAuCl_4/g\text{-}C_3N_4$ in N_2 atmosphere at 300 °C, was demonstrated for the acetylene hydrochlorination reaction to produce vinyl chloride which is an important monomer in polyvinyl chloride industry. Au exists in +1 oxidation state and forms Au^{I}–N_3 active sites through N coordination. DFT study indicated that Au^{I}–N_3 active sites preferentially coordinate with HCl than acetylene inhibiting Au^{I}–N_3 to Au^0 reduction and thereby sustaining the catalytic active sites for hydrochlorination reaction. In contrast, the conventional catalyst, $AuCl_3$ on carbon preferentially coordinates with acetylene leading to the reduction of Au^{III} ion to Au^0 thereby losing its catalytic activity. Au atom occupies the Cv2 defect site present in $g\text{-}C_3N_4$. The electron localisation function (ELF) maps revealed that the Au–N_3 sites are having a T-shape structure with lone-pair electrons (Fig. 26(a–c)). $Au_1/g\text{-}C_3N_4$ single atom catalyst exhibited 70% conversion of acetylene in 600 min without any loss of activity. In comparison, $HAuCl_4/g\text{-}C_3N_4$ catalyst exhibited a maximum conversion of 72.1%, but got significantly decreased to 14.5% in just over 500 min as a result of the reduction of Au^{III} to Au^0. However, the Au NPs/$g\text{-}C_3N_4$ catalyst showed only very weak activity confirming that Au^0 is catalytically inactive towards acetylene conversion. Au–N_3 active sites preferentially adsorb HCl by a dissociative mechanism with an adsorption energy (E_{ads}) of −2.25 eV which is higher than the E_{ads} of acetylene (−1.17 eV), preventing the reduction of Au^{I} to Au^0 by C_2H_2. But in the case of $AuCl_3/C$ catalyst, C_2H_2 has a higher adsorption energy of −1.04 eV than HCl (−0.74 eV). The interaction of HCl with $Au_1/g\text{-}C_3N_4$ weakens the Au–N bond as evident from the shifting of the d band center, associated with the Au 5d orbital, farther from the Fermi level in PDOS of HCl adsorbed catalyst. However, in the case of acetylene adsorbed catalyst, there is no shift of band center associated with the 5d and 6s orbital in the PDOS (Fig. 26(d–f)). The competitive HCl adsorption prevents Au^{I} to Au^0 reduction rendering enhanced stability for the catalyst. $g\text{-}C_3N_4$ as a support contributes towards the enhanced stability of the catalyst through π–π interaction of its electron-deficient heptazinic center with electron-rich C_2H_2. The HCl adsorbed on the active site interact with the acetylene following Langmuir–Hinshelwood (LH) mechanism. The DFT calculation supplements the improved performance of $Au_1/g\text{-}C_3N_4$ by predicting a small energy barrier for C–H and C–Cl bond formation (0.98 eV) along with small desorption energy of 0.87 eV for the product.[114]

The non-oxidative dehydrogenation of propane (denoted as PDH) is an effective synthetic route for the economical production of propylene. The mechanistic pathway for PDH involves C–H bond scission followed by propylene adsorption on the catalysts. Hence low values for C–H bond activation energy (ΔE) and propylene adsorption energies (E_{ad}) on catalysts are essential attributes. Additionally, the desorption energy of propylene should also be low compared to the energy required for breaking the C–H bond to realise higher selectivity towards propylene. Li *et al.* demonstrates that the sum of ΔE and E_{ad} can be used as a theoretical indicator to elucidate the catalyst efficiency. Thus, a positive value suggests that C–H bond dissociation is slower than propylene desorption while a negative value is an indicator of propylene being strongly adsorbed on TM/$g\text{-}C_3N_4$. Employing DFT calculations, the group screened the potential of 12 transition metals supported on $g\text{-}C_3N_4$ (V, Cr, Mn, Zr, Nb, Ru, Rh, Pd, Os, Ir, Pt, Au) as SACs for PDH. The study predicts that a single atom transition metal catalyst can be active and selective for PDH by virtue of its highly exposed d states that enable C–H bond activation and rapid desorption of propylene through weak propylene-π adsorption mode.

$g\text{-}C_3N_4$, being thermally stable up to T ~550 °C, can effectively perform the role of stable support for PDH catalysis which conventionally operates at 530 °C. Moreover, the support facilitates firm anchoring of single atoms, preventing agglomeration at high-temperature operating conditions. The adsorption energies of single metal atom should be similar to or higher than their cohesive energies for them to bond on $g\text{-}C_3N_4$. This selection rule is satisfied by five transition metals of V, Cr, Mn, Zr, and Nb. Together with conventionally active metals like Ag, Ru, Rh, Pd, Os, Ir, Pt, and Au, atomically dispersed SACs based on $g\text{-}C_3N_4$ were employed for PDH catalysis. Of the 12 systems studied, $Ag1/g\text{-}C_3N_4$ displayed poor PDH activity owing to its high reaction energy (ΔE) for the first C–H bond cleavage and high propylene adsorption energy (E_{ad}). On the other hand, the rate-limiting step of PDH was characterised by a low activation barrier of 1.11 eV for $V_1/g\text{-}C_3N_4$ catalyst. Moreover, high selectivity was also displayed by $V_1/g\text{-}C_3N4$ as the adsorption energy

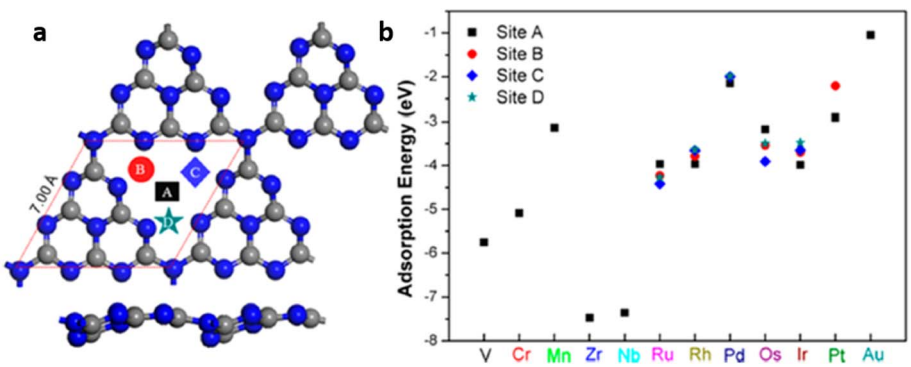

Fig. 27 (a) Possible adsorption sites for single metal atoms in $g\text{-}C_3N_4$ layer, (b) adsorption energies of various metal single atoms on available adsorption sites in the $g\text{-}C_3N_4$ surface. Reproduced with permission from ref. 115. Copyright 2020 American Chemical Society.

of propylene (−0.59 eV) was much lower compared to the activation barrier for deep dehydrogenation (1.97 eV).

In SACs based on C_3N_4, the lattice constant of the planar structure (7.14 Å) is slightly higher than the buckled C_3N_4 structure (7.00 Å). The buckled structure is more stable than the planar structure by 2.05 eV. The four possible adsorption sites (A, B, C, D in Fig. 27(a)) of the single metal atoms move from their initial positions on structural relaxations. The adsorption energies of various single metal atoms on the g-C_3N_4 surface are shown in Fig. 27(b). V, Cr, Mn, and Zr are g-anchored firmly on g-C_3N_4 as the cohesive energies are lower than their adsorption energies. Moreover, the Pd single atoms of synthesised Pd_1/g-C_3N_4 had adsorption energy smaller than the binding energies of above-mentioned TMs enabling the practical viability of TM based SACs for PDH.[115]

g-C_3N_4 containing single atom Cobalt (Co SACs) up to 23.58 wt% loading was demonstrated to be an excellent catalyst for oxidation of ethylbenzene in the air with a high turn-over frequency of 19.6 h^{-1} and 97% selectivity for acetophenone formation. The catalytic pathway involves the formation of Co–

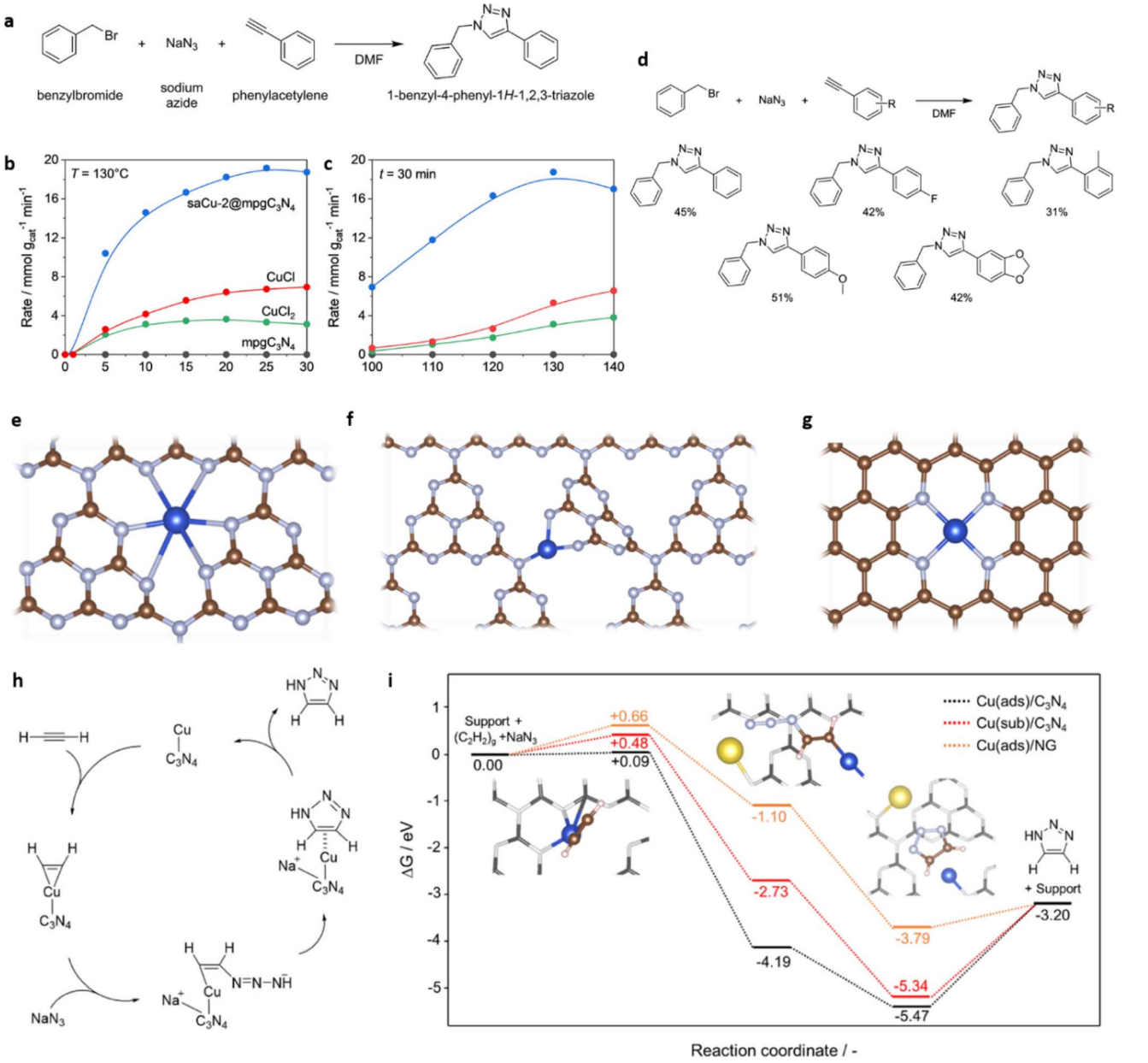

Fig. 28 (a) Reaction scheme of cycloaddition, (b and c) the comparison of catalytic performance of $mpgC_3N_4$, $CuCl_2$, CuCl, and saCu-2@$mpgC_3N_4$ with respect to (b) time and (c) temperature, (e–g) the structural model for the Cu coordination in Cu-based SACs (e) Cu adsorbed in the heptazinic pore of C_3N_4 (Cu(ads)/C_3N_4), (f) Cu substituted the carbon in C_3N_4 (Cu(sub)/C_3N_4), and (g) Cu adsorbed on N-doped graphene at its dicarbon vacancy (Cu(ads)/NG), (h) proposed reaction mechanism for click cycloaddition over supported Cu_1 active sites, (i) reaction free-energy profile for (Cu(ads)/C_3N_4), (Cu(sub)/C_3N_4), and (Cu(ads)/NG) at 130 °C (inset: structures of intermediates formed over (Cu(ads)/C_3N_4)). Reproduced with permission from ref. 117. Copyright 2022 the authors. Published by American Chemical Society.

Table 7 Summary of g-C_3N_4 SACs for thermal catalysis

System	Single atom & loading	Synthesis method	Catalytic application, product yield/rate/turnover frequency (TOF) & selectivity	Coordination site or structure & oxidation state	Ref.
[Pd]mpg-C_3N_4	Pd 0.5 wt%	Post synthesis-chemical reduction	Hydrogenation of alkynes & nitroarenes 1-hexyne to 1-hexene: rate 1.41×10^3 $mol_{product}$ mol_{Pd}^{-1} h^{-1} & selectivity 90%, 2-methyl-3-butyn-2-ol to 2-methyl-3-buten-2-ol, 3-hexyne to *cis*-3-hexene, nitrobenzene to aniline	Nitrogen	4
AgTCM-mpg-CN	Ag 1 wt%	Direct synthesis	Hydrogenation of 1-hexyne to 1-hexene, rate 100 mol_{alkyne} h^{-1} mol_{Ag}^{-1}, selectivity 100%	Carbon or nitrogen, +1	17
Au_1/mpg-C_3N_4	Au 519 ppm	Post synthesis-reduction under an inert atmosphere	Silane oxidation with water, $PhMe_2SiH$ to $PhMe_2SiOH$, yield 99%, 30 min, selectivity >99.9%, TOF 50200 h^{-1}	Carbon or nitrogen, +1	26
Pd-ECN	Pd 0.66 wt%	Microwave treatment (post synthesis)	Suzuki coupling of bromobenzene with phenylboronic acid pinacol ester to form biphenyl, 63% conversion, 90% selectivity, rate 0.57 $mmol_{product}$ min^{-1} g_{cat}^{-1}	Nitrogen, Pd^{2+}/Pd^{4+} ratio 0.82	111
PtRuSA-CN	Pt 0.51 wt% Ru 0.45 wt%	Post synthesis-photochemical reduction	CO oxidation 100% conversion at 150 °C	C–Pt–Ru–N	8
Cu1@HCNS	Cu 0.85 wt%	Supramolecular preorganisation assisted direct synthesis	Non-oxygenative coupling of amines to imines using H_2O & light, benzylamine to imine: 10 583 μmol g^{-1} h^{-1}, 96% selectivity	Cu_1N_3, +1	69
Cu–CN-*x*	Cu 8 wt%	Template free direct synthesis	Carboxylation of terminal alkynes using atmospheric CO_2; phenylacetylene to phenylpropiolic acid: yield 97%, TOF 9.7 h^{-1}	Nitrogen, +1	112
Pd_1/C_3N_4	Pd 0.18 wt%	Post synthesis-reduction under an inert atmosphere	(a) Hydrogenation; (i) styrene to ethylbenzene: 98% conversion in 1.5 h, TOF: 834 h^{-1}, (ii) furfural to furfuryl alcohol: 64% conversion in 4 h, TOF: 146 h^{-1}, (b) hydrodechlorination of 4-chlorophenol to phenol: 99% conversion in 10 min, TOF: 13 333 h^{-1}	Nitrogen, +1	113
Au_1/g-C_3N_4	Au 0.414 wt%	Post synthesis	Hydrochlorination of acetylene to vinyl chloride: 70% conversion in 600 min	$Au–N_3$, +1	114
TM/g-C_3N_4	V, Cr, Mn, Zr, Nb, Ru, Rh, Pd, Os, Ir, Pt, Au	DFT study	Non-oxidative dehydrogenation of propane to propylene, predicted highest activity & selectivity for V_1/g-C_3N_4	—	115
Co SAC (Co SACs/CN)	Co 23.58 wt%	Direct synthesis	Aerobic oxidation of ethylbenzene to acetophenone: 62% conversion, 40 h, 99% selectivity, TOF: 19.6 h^{-1}	$Co–N_2$, +2	116
UHD-Cu_1/PCN	Cu 23 wt%	Post synthesis – reduction under an inert atmosphere	Azide–Alkyne cycloaddition reaction: cycloaddition between benzyl azide & 4-ethynylanisole to form 1-benzyl-5-(4-methoxyphenyl)-1H-1,2,3-triazole, yield 92%, 12h	Nitrogen, +1	11
saCu@mpg C_3N_4	Cu1.6 wt%	Template assisted direct synthesis	Click cycloaddition between phenylacetylene and *in situ* formed benzyl azide (from benzyl bromide, & sodium azide) to form 1-benzyl-4-phenyl-1H-1,2,3-triazole, yield 45%, 30 min	Nitrogen, +1	117
Cu–P-g-C_3N_4	Cu 1.8 wt%	Template free direct synthesis	Oxidation of CO to CO_2 100% conversion	Nitrogen, 0	118
M@gt-C_3N_4	M = Mn, Fe, Co, Ni, Cu, and Mo	DFT study	CO_2 hydrogenation to HCOOH, CO, & CH_3OH, Co@gt-C3N4 was theoretically predicted to be the most efficient system	Nitrogen	119

O bond through O_2 adsorption while ethylbenzene adsorbs on the catalyst surface. The subsequent abstraction of the H atom from the CH_2 group of ethylbenzene produced acetophenone through the intermediates of phenylethyl radical and hydroperoxyl radical.[116]

The potential of g-C_3N_4 based ultra-high density copper single atom catalyst (UHD-Cu_1/PCN SAC) was demonstrated for catalysing the azide–alkyne cycloaddition reaction between benzyl azide and 4-ethynylanisole at 60 °C using water-*tert*-butanol (1 : 1) mixture as solvent. The effect of Cu content on the catalytic activity to yield 1-benzyl-5-(4-methoxyphenyl)-1H-1,2,3-triazole was investigated. As the Cu loading increased, the number of active sites as well as the site-specific activity for UHD-Cu1/PCN SAC also enhanced remarkably yielding 92% of 1,5-disubstituted triazole in 12 h. However, no explanation was provided for the selective formation of the 1,5-disubstituted triazole rather than the 1,4-regioisomer.[11]

Recently, single atom copper catalysts on mesoporous graphitic nitride (saCu-*x*@mpgC_3N_4), obtained by the template assisted direct synthesis involving sodium tricyanomethanide, $CuCl_2 \cdot 2H_2O$, cyanamide and SiO_2 particles, were demonstrated to catalyse click cycloaddition between various phenylacetylene derivatives and *in situ* formed azides (from benzyl bromide, and sodium azide) (Fig. 28(a)). Cu-2@mpgC_3N_4 catalyst with 1.6 wt% of Cu loading exhibited a yield of 45% for 1-benzyl-4-phenyl-1H-1,2,3-triazole in DMF solvent at 130 °C for 30 min (Fig. 28(b and c)). The reaction mechanism evolved from the three possible coordinating structures (Fig. 28(e–g)), involved acetylene activation by adsorption on Cu(ads)/C_3N_4 with a minimal thermodynamic barrier of +0.09 eV relative to Cu(sub)/C_3N_4 (+0.48 eV) and Cu(ads)/NG (+0.66 eV). Subsequently, sodium azide reacts with the C atom of acetylene forming a stable linear intermediate over Cu(ads)/C_3N_4 with a free energy change of −4.19 eV compared to Cu(ads)/NG and Cu(sub)/C_3N_4 with more positive free energy values of −1.10 eV and −2.73 eV respectively. A triazolate pentacyclic ion attached to the Cu SAC was formed on the completion of cyclisation with free energies of −3.79 eV, −5.34 eV, −5.47 eV for Cu(ads)/NG, Cu(sub)/C_3N_4, and Cu(ads)/C_3N_4 respectively. The final step of catalyst regeneration was by the desorption of sodium triazolate molecule where the desorption energy barrier was highest for Cu(ads)/C_3N_4 (2.27 eV) compared to Cu(ads)/NG (0.59 eV) and Cu(sub)/C_3N_4 (2.14 eV) (Fig. 28(h and i)).[117]

Sleim *et al.* demonstrated the complete conversion of CO to CO_2 by thermal oxidation at 184 °C utilising single atoms of Cu incorporated on ultra-thin sheets of porous C_3N_4 (Cu–P-g-C_3N_4). The SAC developed was characterised by a high surface area of 240 $m^2\ g^{-1}$ and contained 1.8 wt% of Cu atoms isolated through coordination with the nitrogen of C_3N_4. The Cu–N coordination sites bond weakly to the intermediates and products enabling faster reaction kinetics at relatively low temperature.[118]

The potential of metal embedded C_3N_4 catalysts (M@gt-C_3N_4, where M stands for Mo, Ni, Co, Cu, Mn and Fe) were evaluated through first principles calculations and *ab initio* molecular dynamics (AIMD) simulations, for the catalytic hydrogenation of CO_2 to HCOOH, CO, and CH_3OH. The p orbitals of pyridinic N atoms in s-triazine-based graphitic C_3N_4 (gt-C_3N_4), bond strongly with the d (p) orbitals of single metal atoms activating H_2 and CO_2. The co-adsorbed state, thus formed, acts as intermediates to the hydrogenation of CO_2 to different C_1 products, with the metals Mn, Fe, Mn and Co providing superior catalytic performance compared to others. The binding energy (ΔE_b) values of a metal single atom anchored on gt-C_3N_4 and the ΔE_b values for all the M@gt-C_3N_4 vary from −2.25 to −3.72 eV confirming the thermodynamic feasibility of metal incorporation on gt-C_3N_4. Furthermore, the thermal stability of the SACs was evaluated from AIMD simulations and estimating the energy barrier values for surface migration of metal atoms. Considering Co@gt-C_3N_4 as a representative example, it was established that the framework structure was retained without bond fission and metal migration even after 10 ps AIMD stimulation. A high energy barrier of 2.11 eV ruled out the possibility of Co atom migration. Additionally, the evaluation of electronic properties through band structure analysis, charge density difference and electron spin density calculations indicated that Cu@gt-C_3N_4 possessed metallic nature whereas all other metal atoms induced semiconducting properties. This was attributed to the availability of more valence electrons in Cu compared to the rest of the metals as well as to the strong hybridisation of Cu orbitals with neighbouring N orbitals resulting in a high Fermi level value of −2.02 eV relative to the range of −2.98 to −2.15 eV for other

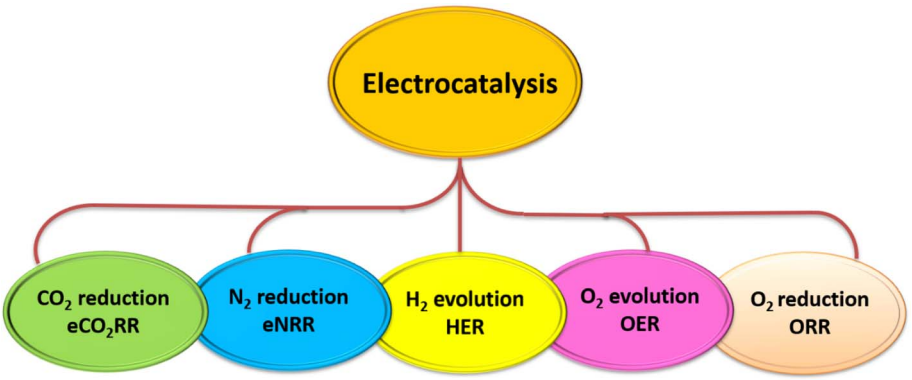

Fig. 29 Various electrocatalytic reactions catalysing by g-C_3N_4 based SACs.

metal SACs. The hydrogenation of CO_2 starts with the adsorption of CO_2 and H_2 molecules in bidentate configuration. The adsorption energies (E_{ads}) of CO_2 over the metal atom, vary between −0.33 to −1.25 eV whereas E_{ads} of H_2 lies between −0.70 and −1.21 eV. The co-adsorption of CO_2 and H_2 is energetically more favourable for all M@gt-C_3N_4, except for that of Mn. For the representative Co@gt-C_3N_4 system, H_2 adsorption proceeds exothermic route with an E_{ads} value of 1.13 eV followed by the adsorption of CO_2 whereas co-adsorption occurs with the release of energy of 0.19 eV. CO_2 hydrogenation follows the Langmuir–Hinshelwood (L–H) mechanism which starts with the coadsorption of CO_2 and H_2. The CO_2 hydrogenation process follows various pathways to produce various products. The HCOO* pathway led to HCOOH formation. A reverse water-gas shift (RWGS) reaction pathway produces CO, whereas a mixed reaction pathway involving CO intermediate hydrogenation (CO-hydro) and RWGS results in CH_3OH formation. The hydrogenation of CO_2 led to the formation of CO intermediate with high E_{ads} ranging from −2.07 to −2.61 eV which makes the desorption of CO difficult from the catalyst surface and thereby facilitates further hydrogenation to produce CH_3OH. In the case of Co@gt-C_3N_4 which was theoretically predicted to be the most efficient system for CO_2 hydrogenation, HCOOH formation occurs with the lowest energy barrier of 0.58 eV, whereas the formation of CO and CH_3OH occurs by overcoming an energy barrier of 0.67 eV and 0.95–1.19 eV respectively.[119] The SACs demonstrated for thermal catalysis with the salient outputs are presented in Table 7.

5.3 Electrocatalytic applications of g-C_3N_4 based SACs

Electrocatalysis is perceived to be a promising approach to meet the continuously increasing energy demand by employing various technologies, such as the electrolysis of water, CO_2 reduction, fuel cells, *etc.* The underlying electrochemical processes enable the sustainable utilisation of renewable electrical energy with appreciable energy conversion efficiencies. Precious metals (Pt, Ir, Ru, Rh, Pd, *etc.*) and their metal oxide-based catalysts are widely used in the field of electrocatalysis.[120] However less availability and high cost hinder their widespread application. The utilisation of single atom catalysts of precious & non-precious metals with high intrinsic activity, unique electronic structure, and high atom utilisation efficiency help to improve the electrocatalytic performance for various reactions (Fig. 29).[121]

5.3.1 Electrocatalytic CO_2 reduction. Electrocatalytic reduction of CO_2 (eCO2RR) to valuable feedstocks by utilising renewable electrical energy is an environmentally benign strategy to mitigate carbon emission, fossil fuel depletion, and reduce the climatic impact of the green-house effect.[119] CO_2 reduction proceeds *via* multi electron–proton transfer steps and converts it to various products like CO, HCOOH, CH_4, CH_3OH, C_2H_5OH, and C_2H_4 and higher hydrocarbon *etc*[122] as shown in the equations below.

$$CO_2 + 2H^+ + 2e^- \rightarrow HCOOH$$

$$CO_2 + 2H^+ + 2e^- \rightarrow CO + H_2O$$

$$CO_2 + 6H^+ + 6e^- \rightarrow CH_3OH + H_2O$$

$$CO_2 + 8H^+ + 8e^- \rightarrow CH_4 + 2H_2O$$

$$2CO_2 + 12H^+ + 12e^- \rightarrow C_2H_4 + 4H_2O$$

$$2CO_2 + 12H^+ + 12e^- \rightarrow C_2H_5OH + 3H_2O$$

Zhang *et al.* developed Mn based SACs through thermal treatment of a precursor mix containing manganese acetate, dicyandiamide (DCD), and CNT under an inert atmosphere of N_2 at 600 °C. SACs with Mn–N_3 sites embedded in the mixed matrix of g-C_3N_4 with carbon nanotubes (Mn–C_3N_4/CNT) exhibited excellent eCO2RR in aqueous electrolyte with 98.8% of faradaic efficiency (FE) and CO partial current density (j_{CO}) value of 14.0 mA cm^{-2}, at a low overpotential of 0.44 V. j_{CO} further improved to 18.6 and 29.7 mA cm^{-2} at an overpotential of 0.42 and 0.62 V, respectively by the usage of ionic liquid (IL) electrolyte. Theoretical studies and XAS analysis revealed that CO_2 can easily get adsorbed on Mn–N_3 active site which facilitated a low free energy barrier for COOH* intermediate formation.[123]

The potential of atomically dispersed Er atoms on g-C_3N_4 nanotubes described earlier for photocatalytic CO_2 reduction, has been evaluated for eCO2RR. HD-Er_1/CN-NT exhibited enhanced cathodic current compared to pure CN-NT and LD-Er_1/CN-NT.[9]

Yan Jiao *et al.* used DFT calculations to predict different C–C coupling pathways for the eCO2RR to C_2H_4 over Cu–C_3N_4 SACs utilising Cu/C or Cu/N dual active sites present in it. The reduction proceeded *via* 12 e^- and 12 proton transfer pathways at a potential of −0.764 V *vs.* SHE. The first in the process is the protonation of a CO_2 molecule to *COOH at any of the three active sites of Cu, C, N present in the catalyst. DFT study and associated ΔG calculations divulged that the Cu active site with a ΔE of 0.37 eV is preferred to N active site with 1.47 eV. Even though active sites of C possess the lowest ΔE of 0.37 eV, it is difficult to facilitate C–C coupling as the reaction proceeds. Based on the sites and intermediates involved in the formation of C_2H_4, 14 different pathways are suggested in two categories involving the Cu/N dual active sites and Cu/C dual active sites. The Cu/C pathway exhibited a better synergistic effect than Cu/N which is beneficial for possessing catalytic activity comparable to Cu (100).[124]

Electrochemical CO_2 reduction to formate was demonstrated in exfoliated g-C_3N_4 (GCN) containing atomic dispersions of Cu (Cu-GCN). XANES analysis indicated the presence of both Cu^{2+} and Cu^+ with an average oxidation state of +1.4 confirming different Cu–N co-ordinations, coupled with DFT calculations, the authors predicted a partially polymerised GCN that retained a few amino functional groups coordinated to Cu as the Cu atoms are expected to interact preferentially with pyridinic N atoms. The catalyst Cu-GCN(20) exhibited CO2RR activity in bicarbonate solution through the formation of formate as the only product in the liquid phase, with a faradaic efficiency of 12% and a current density of 14 mA mg_{cat}^{-1}. However, in the phosphate solution HER was predominant over CO2RR and hydrogen was obtained as a result of HER rather than CO2RR.[125]

Table 8 Summary of g-C_3N_4 SACs for electrocatalytic CO_2 reduction

System	Single atom & loading	Synthesis method	Products, FE, current density (j) & overpotential	Coordination site or structure & oxidation state	Ref.
Mn–C_3N_4/CNT	Mn 0.17 wt%	Template free direct synthesis	CO, FE 98.8%, j_{CO} 14.0 mA cm^{-2} at 0.44 V	Mn–N_3, +2	123
Er_1/CN-NT	Er 18.4 wt%	Freeze drying assisted direct synthesis	HD-Er_1/CN-NT exhibited higher cathodic current than LD-Er_1/CN-NT & CN-NT	Er–N_3, +1	9
Cu–C_3N_4	Cu	DFT study	C_2H_4, Predicted Cu/C active sites favours C_2H_4 formation than Cu/N	—	124
Cu-GCN(20)	Cu 20 wt%	Chemical reduction assisted post synthesis	Formate ($HCOO^-$), FE 12%	Nitrogen, +1 & +2	125
ZnSA–CN–G	Zn, 1.2 wt%	Freeze drying assisted direct synthesis	CO, FE 87.1% at −0.5 V	Nitrogen, oxidation state in between 0 & +2	126

Ge *et al.* successfully developed an efficient electrocatalyst (ZnSA–CN–G) for CO2RR by dispersing zinc single atoms (ZnSA) on graphitic carbon nitride nanosheets (CN) and graphene (G) through the pyrolysis of a precursor mix containing DCDA, graphene-oxide nanosheets (GO nanosheets) and $ZnCl_2$. During the pyrolysis process at 700 °C, the conversion of DCDA to CN facilitated the atomic level dispersion of Zn single atoms to CN matrix with Zn–N coordination and GO was reduced to graphene. ZnSA–CN–G catalyst with a metal loading of 1.2 wt%, exhibited excellent conversion of CO_2 to CO with 87.1% of FE at a potential of −0.5 V *vs.* RHE. The enhanced electrocatalytic activity is derived from the availability of abundant Zn single atoms as well as from the enhanced surface area & electrical conductivity of ZnSA–CN–G.[126]

The electrocatalytic CO_2 reduction capabilities demonstrated for g-C_3N_4 based SACs are presented in Table 8.

5.3.2 Electrocatalytic nitrogen reduction reaction (eNRR). The large-scale commercial synthesis of ammonia is currently realised through the traditional Haber Bosch process which is a high temperature, high pressure route and consequently is highly energy intensive and environmentally non-friendly.[127] The conversion of N_2 to NH_3 through electrochemical means is an attractive option by virtue of the milder conditions of operation and low energy requirements. Electrocatalytic nitrogen reduction reaction (eNRR), analogous to nitrogen fixation by nitrogenase enzymes, is the most sustainable pathway for ammonia production. Bulk catalysts like Fe and Rh are demonstrated for eNRR but with low efficiency, poor selectivity and slow kinetics.[128] Single atom catalysts with an optimal concentration of highly active metal sites have shown the potential to be highly effective for eNRR through improved selectivity, kinetics and efficiency.[87,129]

eNRR is a six-electron reaction progressing in both associative and dissociative mechanisms. The former involves the release of NH_3 simultaneously with N≡N bond cleavage and proceeds through the distal, alternating, and enzymatic pathways. In the dissociative route, N≡N cleaves into two separate N atoms before hydrogenation. The reduction process is initiated by the adsorption of N_2 to metal atoms and the adsorption energy calculations suggest that it proceeds preferably *via* an end on configuration.[130] Computing ΔG associated with the formation of possible species (N_2H^*, $N_2H_2^*$, $N_2H_3^*$, $N_2H_4^*$, N*, NH*, and NH_2^*) and identification of the potential determining step (PDS) through different pathways facilitate mechanisms to evaluate the efficiency of the catalyst.[131]

In one of the initial reports on SACs based on g-C_3N_4, Zhao and Chen employed DFT based computational studies to investigate the effectiveness of a variety of single atoms (Ag, Ru, Pd, Rh, Au, Pt, W, Ni, Ti, Mo Cr, Mn, Co, and Fe) on C_3N_4 for eNRR (Fig. 30(a)). The structural stabilities of the catalysts were computed from the energy of the adsorption of the metal atoms on g-C_3N_4 (Fig. 30(b)). Single atoms of Ti, Mn, Pd, Ag, Au and W were adsorbed on the six-fold cavity of g-C_3N_4 with metal–N bond lengths varying in the range of 2.28–2.51 Å. The group comprising of Cr, Ni, Fe, Co, Cu, Mo, Ru, Rh, and Pt were anchored favourably at the corner of the same cavity with metal–N bond lengths of 1.90–2.11 Å. The difference in adsorption sites was ascribed to the differences in atomic radii and electronegativity values. Electron transfer from metal atoms to C_3N_4 induces positive charges on metals facilitating eNRR and suppressing the competitive HER.[132]

Ding *et al.* compared the suitability of g-C_3N_4 and graphene, as support layers with differences in their coordination environment, for incorporating single atoms of V, Nb, and Ta (Fig. 30(c)). Their subsequent use as electrocatalysts for nitrogen reduction was evaluated based on the ability of the catalyst to adsorb nitrogen for the activation of N≡N, the creation of a stable N_2H^* adsorption on the catalyst and the destabilisation of NH_2^*. The reactivity screening revealed that V, Nb, and Ta anchored onto graphene support, could only weakly stabilise the NH_2^* species and hence were considered to be unsuitable for eNRR. The binding energy of single atoms on C_3N_4 was used to ascertain the structural stability of SACs. The values ranging from −6.48 to −7.58 eV confirmed that the C_3N_4 layers with the corner vacancy are best suited to facilitate the anchoring of TM atoms. The band gap and spin density distribution calculations indicated strong N_2 adsorption capacity for TMs on C_3N_4. The E_g of C_3N_4 lowered significantly from 2.84 eV to 1.36 eV (Ta/C_3N_4) and 1.35 eV (Nb/C_3N_4). Among the three

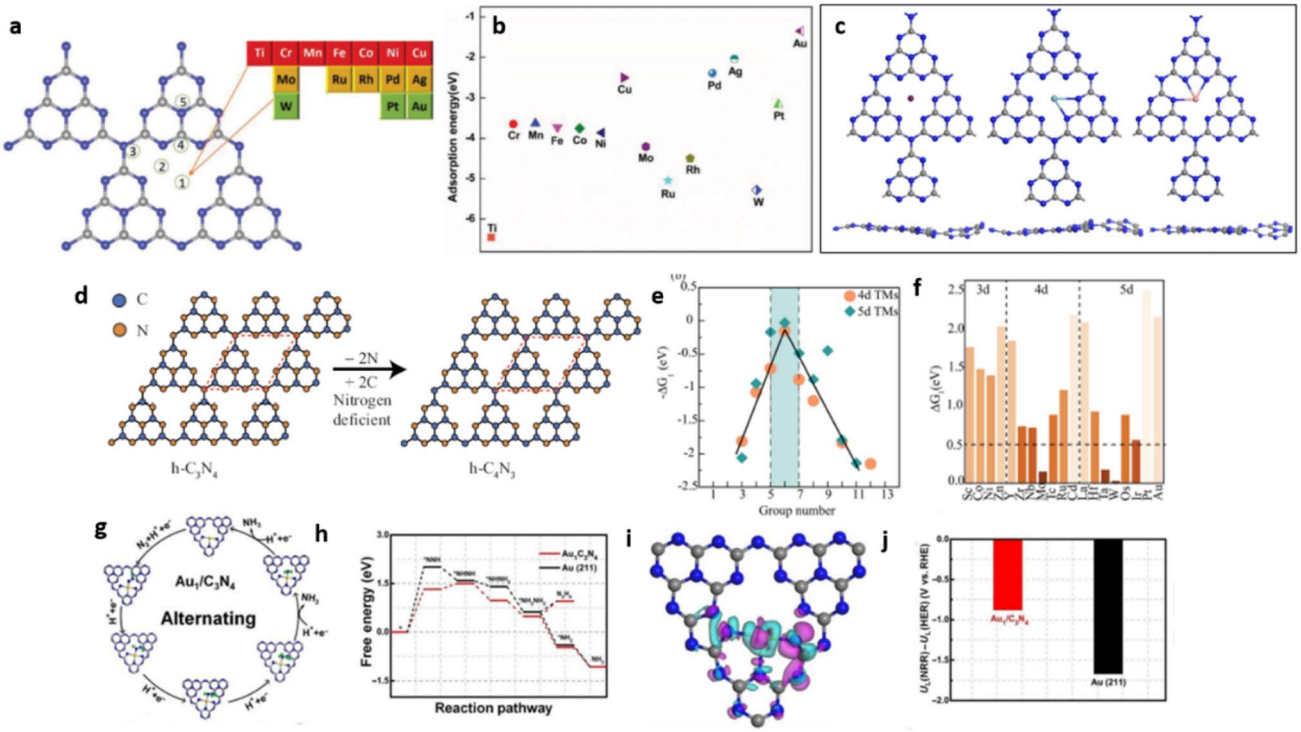

Fig. 30 (a) g-C_3N_4 monolayer structure with possible coordination sites for single metal atoms and their (b) adsorption energies (calculated) HER. Reproduced with permission from ref. 132. Copyright 2018 John Wiley and Sons. (c) Optimised monolayer g-C_3N_4 structure with V, Nb, Ta single atoms. Reproduced with permission from ref. 133. Copyright 2020 American Chemical Society. (d) Structural transformation of h-C_3N_4 to h-C_4N_3, (e) $-\Delta G_1$ *versus* group number for 4d and 5d TMs (f) ΔG_1 for the screened TM-SACs. Reproduced with permission from ref. 134. Copyright 2021 American Chemical Society. (g) Alternating mechanism of NRR on Au_1/C_3N_4 with optimised structures of various intermediates, (h) free energy profile of NRR using Au_1/C_3N_4 and Au (211), (i) change in electron density induced by anchored Au atom on g-C_3N_4 (cyan and pink colour indicate accumulation and depletion of electron density respectively), (j) limiting potential difference in NRR and HER. Reproduced with permission from ref. 135. Copyright 2018 Elsevier.

TMs evaluated, SACs based on Nb/C_3N_4 were shown to possess the highest catalytic efficiency with high selectivity for NRR compared to HER by virtue of the ΔG max of 0.05 eV realised through a distal mechanism.[133]

Singh *et al.* employed density functional theory for the design of transition metal (TM) anchored heptazine-derived graphitic C_4N_3 (h-C_4N_3) based SACs. The catalytic efficiency was gauged by the ability of a metal to facilitate HER through the adsorption and protonation of nitrogen. The number of valence electrons of TM was identified to be an indicator to predict the catalytic efficiency of SACs. Among the carbon nitrides, h-C_4N_3 formed by the replacement of two N atoms with C atoms was identified to be a better support than C_3N_4, as the former is metallic offering a free flow of electrons (Fig. 30(d)). 27 transition metals anchored SACs were investigated and the evaluation of N_2 adsorption energies qualified Sc, Co, Ni, Zr, Nb, Mo, Ru, Ta, W, and Os for eNRR (Fig. 30(e and f)). Subsequently, considering the feasibility of protonation of N_2^* to N_2H^* intermediate, only 3 of the 27 TMs namely Mo, W and Ta were found comparatively more effective. Among the three qualified, only Mo and W showed higher selectivity for eNRR and the highest efficiency was accorded to Mo based SACs by virtue of their extremely low overpotential of 0.02 eV *versus* SHE. The estimated faradaic efficiency was 97.3% for Mo-SAC. Thermodynamic analysis of the reduction pathways (distal, alternating and mixed) suggested that the most favourable mechanism for the conversion of N_2 to NH_3 by Mo-SAC is the mixed mode with a limiting potential of −0.18 eV *vs.* SHE. The potential limiting step (PLS) for this mechanism is the conversion of N_2H_2* to $NH - NH_2^*$ intermediate.[134]

Wang *et al.* evaluated the catalytic performance of atomically dispersed Au on C_3N_4 for the electrochemical reduction of N_2 to NH^{4+} in an aqueous sulphuric acid solution. A high ammonium yield rate of 1305 μg h^{-1} mg_{Au}^{-1} had been realised and the yield was roughly 22.5 times more than that obtained by employing Au nanoparticles as catalysts. The direct eNRR to NH^{4+} was thus demonstrated with an energy utilisation rate of 4.02 mmol kJ^{-1}. DFT calculations revealed that the mechanistic pathway involves an alternating mechanism with the reduction of N_2 to *NNH as the rate determining step with a positive ΔG value of 1.33 eV for Au–C_3N_4 SACs compared to a higher ΔG value of 2.01 eV for Au nanoparticles (Fig. 30(g and h)). The electron density difference due to the anchoring of Au on g-C_3N_4 also favoured stronger binding interaction between Au and *NNH (Fig. 30(i)). Bader charge population analysis confirmed charge transfer from Au to C_3N_4 leading to the shifting of the d-orbital position towards the Fermi level enabling enhanced interaction with intermediates. The selectivity of Au–C_3N_4 SACs towards

Table 9 Summary of g-C_3N_4 SACs for electrocatalytic nitrogen reduction reaction

System	Single atom & loading	Synthesis method	Rate, FE, limiting potential	Coordination site or structure & oxidation state	Ref.
TM@C_3N_4	TM = Ag, Ru, Pd, Rh, Au, Pt, W, Ni, Ti, Mo Cr, Mn, Co, Fe	DFT study	W@C_3N_4 is predicted to exhibit the highest NRR activity with a limiting potential of −0.35 V	Nitrogen	132
TM/CN	TM = V, Nb, Ta	DFT study	Nb/CN is predicted to exhibit highest NRR activity with a low ΔG_{max} (0.05 eV)	Nitrogen	133
TM-SAC (TM h^{-1}-C_4N_3)	TM = Sc, Co, Ni, Zr, Nb, Mo, Ru, Ta, W, and Os	DFT study	Mo-SAC is predicted to be the most effective eNRR catalyst with an ultralow overpotential value of 0.02 V & high FE	Nitrogen	134
Au–C_3N_4	Au 0.15%	Post synthesis – reduction under inert atmosphere	Rate: 1305 μg h^{-1} mg_{Au}^{-1}, FE: 11.1% at −0.10 V	Nitrogen, +1	135

NRR, compared to HER, was ascertained based on the thermodynamic limiting potentials which was computed to be −0.88 V for SACs relative to −1.67 for Au nanoparticles-based catalysts (Fig. 30(j)).[135] Table 9 summarises the g-C_3N_4 based SACs demonstrated for eNRR applications.

5.3.3 Electrocatalytic hydrogen evolution. Hydrogen is a clean source of energy with high energy density and is considered to be the fuel of the future. Green hydrogen produced through economically viable water electrolysis enables sustainable energy generation without carbon

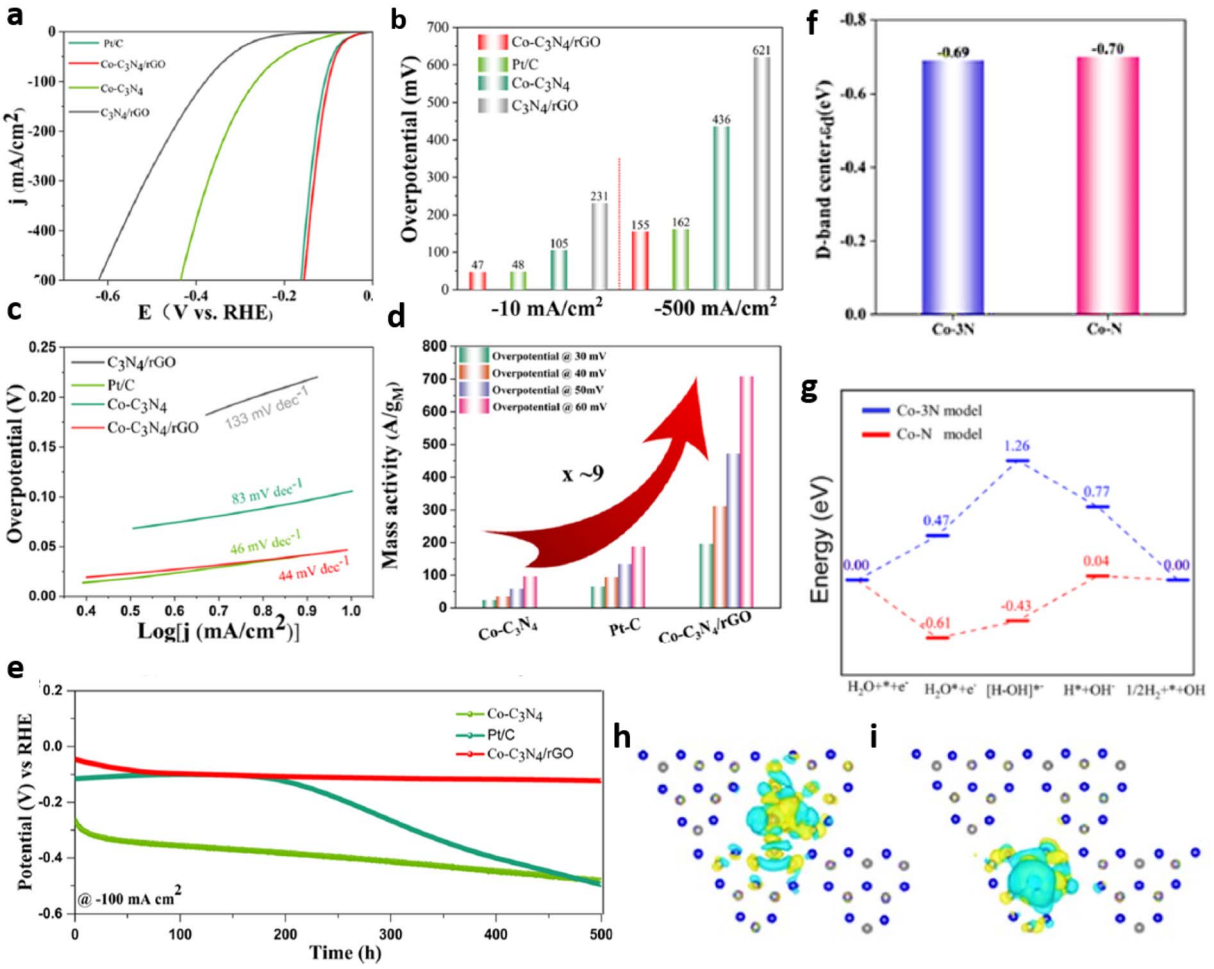

Fig. 31 Data elucidation of HER activity, (a) LSV curves in 1.0 m KOH, at a scan rate of 5 mV s^{-1} for Co–C_3N_4/rGO, Co–C_3N_4, C_3N_4/rGO, and Pt/C, (b) overpotential values of the developed catalysts for a current density of −10 and −500 mA cm^{-2}, (c) Tafel plots, (d) mass activity of the developed catalyst in comparison with Pt/C, at different overpotentials (e) time-dependent overpotential curves of Co–C_3N_4/rGO, Co–C_3N_4, in comparison with Pt/C. Co–N and Co–3N systems with (f) d-band centers, (g) energy profiles, charge density differences in structures of (h) Co–N3, (i) Co–N1. Reproduced with permission from ref. 138. Copyright 2022 American Chemical Society.

footprints. The efficient production of high-purity green hydrogen *via* electrocatalysis is being pursued by researchers worldwide. Electrocatalytic hydrogen evolution is thus a promising pathway in the efforts for affordable hydrogen generation. SACs have been recently demonstrated to be efficient HER electrocatalysts for hydrogen generation.[136]

Dai *et al.* employed computational studies to explore the potential of transition metal (TM = Ti, V, Cr, Mn, Fe, Co and Ni) based SACs on holey g-C_3N_4 (TM/g-CN) for overall water splitting (HER & OER). Among the various TM/g-CN SACs designed, Co_1/g-CN and Ni_1/g-CN were predicted to perform as the most efficient bifunctional electrocatalysts owing to the strong interaction between the intermediates and catalysts as governed by the d band centre of the metal atoms. The calculations indicated that Co_1/g-CN and Ni_1/g-CN SACs can attain overpotential values of 0.15 V and 0.12 V respectively for HER. Values are comparable with that of Pt reference catalyst with 0.09 V overpotential value.[137]

Single Atom Co dispersed over g-C_3N_4 matrix coupled with RGO and having a metal loading of 6 wt% (Co-g-C_3N_4/rGO SACs, Co-CNG) are shown to perform (10 mA cm^{-2}; ~47 mV) at par with commercial Pt/C catalysts for electrocatalytic HER (10 mA cm^{-2} at ~48 mV). The Co-CNG was better than the commercial Pt/C catalyst with 4 times higher mass activity with 500 h durability (Fig. 31(a–e)). DFT studies supplemented the experimental observations and the superior HER activity of Co-CNG was ascribed to the presence of 20% and 80% of Co–N and Co–3N type coordination structures respectively. Coordination engineering is thus promoted as a pathway to boost HER for Co–N site than Co–3N model by virtue of the unique electronic structure, downshift of d-band centres and low free energy barriers (Fig. 31(f–i)).[138]

The electrocatalytic hydrogen evolution reported for g-C_3N_4 based SACs is summarised in Table 10.

5.3.4 Electrocatalytic oxygen evolution reaction & oxygen reduction reaction (OER & ORR). Technologies for renewable energy sources such as fuel cells, hydrogen generation by water splitting, *etc.* rely on the fundamental reactions of oxygen evolution and oxygen reduction (OER and ORR). Conventionally noble metals (Pt) and oxides (RuO_2) are the benchmark catalyst for highly efficient ORR and OER.[139] However, the widespread use of such catalysts is largely hindered due to their unaffordable cost coupled with poor selectivity and stability. Additionally, as the reactions are of competing nature due to its reversibility, catalysing both by the use of a single catalyst is non-realisable.[140,141] It is therefore desirable to develop bifunctional catalysts with appreciable OER and ORR activities. SACs due to their desirable attributes in terms of structural and electronic properties can function to perform the dual roles of catalysing OER and ORR reactions.

In one of the earlier works, Park *et al.* developed molecularly dispersed nickel on C_3N_4 matrix (Ni–CN) by employing a direct synthetic methodology involving the precursors of melamine and Ni(II) chloride hexahydrate precursors. The optimised catalyst displayed OER activity with an onset potential of 1.54 V (*vs.* RHE) which was 80 mV less positive than g-C_3N_4. Atomic dispersions of Ni species on C_3N_4 through Ni–N bonding were confirmed by EXAFS analysis.[142]

Qiao *et al.* developed organometallic complexes of g-C_3N_4 with transition metals (M−C_3N_4) as electrocatalysts for both OER & ORR activities. Theoretical studies predicted that among the 3d transition metal centres, (M−C_3N_4, where M = Cr, Mn, Fe, Co, Ni, Cu, Zn) Fe, Ni and Co possess the potential to exhibit bifunctional activity toward reversible ORR/OER processes due to high stability of structures. The representative catalyst of Co–C_3N_4 with multi-walled carbon nanotubes (CNT) exhibited higher electrode conductivity exposing all the electrocatalytically active sites of Co–C_3N_4. An onset potential of 0.9 V and a diffusion limited current density of ~5 mA cm^{-2} in O_2-saturated 0.1 M KOH solution was obtained for the Co–C_3N_4/CNT catalyst *via* $4e^-$ dominated ORR pathway. The catalyst also showed an onset potential of ~1.5 V and an anodic current density of 10 mA cm^{-2} at 1.61 V for OER activity in N_2-saturated 1 M KOH solution. The excellent bifunctional performance of Co–C_3N_4/CNT catalysts was at par with precious metal benchmarks and was attributed to the presence of Co–N_2 active sites.[143]

Liu *et al.* developed SAC based electrocatalyst by stabilising Au_1N_x single-sites on g-C_3N_4 (Au_1N_x single-site/C_3N_4) *via* a post synthesis strategy involving electrostatic adsorption. Au_1N_x single-site/C_3N_4 exhibited excellent catalytic activity with good durability for ORR and OER with mass activity values of ~9000 A g_{Au}^{-1} and ~1500 A g_{Au}^{-1} at a half-wave potential ($E_{1/2}$) of 0.76 V and at an overpotential 0.45 V respectively. The catalytic performances were 20 and 26 times higher than the conventional Pt/C and RuO_2 benchmarks. DFT calculations coupled with analysis of the electronic structure revealed the injection of electrons from Au_1Nx site to g-C_3N_4 enabling the formation of

Table 10 Summary of g-C_3N_4 SACs for electrocatalytic hydrogen evolution

System	Single atom & loading	Synthesis method	Current density (j) & overpotential	Coordination site or structure & oxidation state	Ref.
TM/g-CN	TM = Ti, V, Cr, Mn, Fe, Co, Ni	DFT study	Co_1/g-CN & Ni_1/g-CN SACs are predicted to be the most effective HER catalysts with overpotential values of 0.15 V and 0.12 V respectively	Nitrogen	137
Co-gC_3N_4/rGO (Co-CNG)	Co 6 wt%	Template free direct synthesis	10 mA cm^{-2}, 47 mV	20% Co–N & 80% Co–3N type coordination	138

an additional energy level near the Fermi level. This promotes faster redox kinetics for highly efficient OER and ORR reactions. Moreover, the presence of mobile electrons near the Fermi level facilitated surface adsorption of the key intermediates *OO and *OH on Au_1N_x single-sites with a theoretical binding energy of 1.3 and 1.5 eV, close to that Pt and RuO_2 (1.4 eV and 1.7 eV).[22]

In a noteworthy contribution, Sun *et al.* prepared Fe, N doped hollow carbon catalyst (C-FeHZ8@g-C_3N_4) by the pyrolysis of a precursor mixture containing ZIF-8, C_3N_4 and ferric acetyl acetonate. The Fe–N_4 atomic level coordination was affected by C_3N_4 and ferric acetyl acetonate as N and Fe precursors respectively. The optimised catalyst exhibited high ORR activity with $E_{1/2}$ values of 0.18 and 0.845 V in acidic and alkaline conditions. The use of C_3N_4 prevented agglomeration of Fe during high-temperature pyrolysis and facilitated the formation of Fe–N*x* sites through its cyano products formed during decomposition at 950 °C. The incorporation of g-C_3N_4 during the synthesis provides an effective pathway for the stabilisation of single atoms in Fe–C–N catalyst.[144]

Wang and co-workers developed a hybrid ORR–OER electrocatalyst (NGM–CN–Fe) with atomic Fe–N_x between g-C_3N_4 and graphene and were utilised as a material for air electrode cathode in Zn–air battery (ZAB). Fe is atomically dispersed over g-C_3N_4 (bulk CN–Fe) through template free direct synthesis involving dicyandiamide (DCDA) and ferric chloride precursors. Exfoliated porous CN–Fe nanosheets derived from bulk CN–Fe through sonication were subjected to hydrothermal treatment in the presence of graphene nanomesh and annealed at 600 °C to form hybrid NGM–CN–Fe SAC. The catalyst exhibited superior ORR activity with a current density of -6.42 mA cm^{-2} at an improved onset potential of nearly 0.00 V which is 13 times larger than that of atomic Fe dispersed g-C_3N_4 (CN–Fe). Both pure g-C_3N_4 (CN) and CN–Fe displayed an onset potential around -0.26 V and the current density was -0.45 mA cm^{-2} at -0.5 V. In comparison with commercial Pt–C (20 wt%) catalyst, NGM–CN–Fe exhibited a comparable onset potential, better half-wave potential with 20 mV improvement & enhanced current density. The superior activity of NGM–CN–Fe SAC is attributed to the existence of Fe–$N_{4.1}$ coordination sites *via* atomic Fe-bridged coordination between g-C_3N_4 and nitrogen-doped graphene nanomesh.[145]

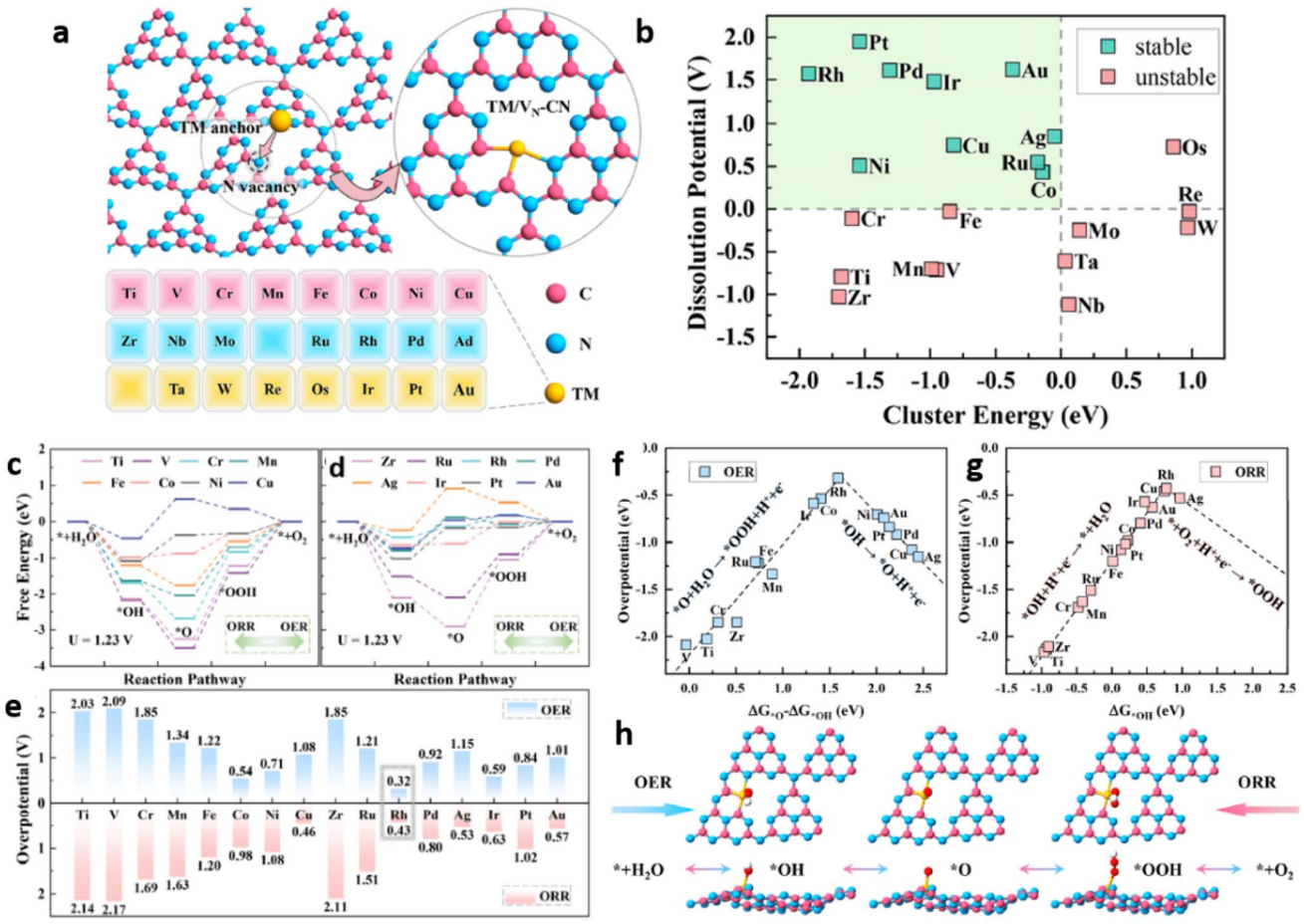

Fig. 32 (a) Schematic representation of various transition metals (TM) based SACs on VN-CN, (b) stability of TM/V_N-CN based on cluster energy (E_{Clus} < 0 eV) and dissolution potential (U_{diss} > 0 eV), the free energy diagrams of TM/VN-CN (c) from Ti to Cu and (d) from Zr to Au related to both OER and ORR at the equilibrium potential of 1.23, (e) The OER and ORR overpotentials of TM/VN-CN (from Ti to Au), the volcano plots of (f) OER ($-\eta$OER *vs.* ΔG*O − ΔG*OH) and (g) ORR ($-\eta$ORR *vs.* ΔG*OH) on TM/VN-CN, (h) OER and ORR intermediate structures adsorbed on Rh/VN-CN. Reproduced with permission from ref. 10. Copyright 2021 American Chemical Society.

Li *et al.* demonstrated the development of OER catalyst with highly dispersed Co atoms over the hierarchical structure of g-C_3N_4 and carbon spheres (C_3N_4@CS), where ultrathin g-C_3N_4 aided the atomic level dispersion of Co atoms. As the electrocatalytic performance of the SACs is influenced by the chemical bonding between the support and single atoms, catalysts with Co–O coordination (Co–O–C_3N_4@CS), and Co–N coordination (Co–C_3N_4@CS), were precisely synthesised by changing the calcination atmosphere from air to argon. Co–O–C_3N_4@CS and Co–C_3N_4@CS catalysts exhibited appreciable OER activity and delivered overpotentials of 0.23 V at 10 mA cm^{-2} and 0.47 V at 50 mA cm^{-2}, respectively in alkaline media. The Co–O–C_3N_4@CS exhibited higher OER performance, at low overpotentials, as the higher electronegativity of O, compared to N, accelerated the adsorption of oxygen species. However, at high overpotentials the activity worsened due to unfavourable desorption energies.[146]

Employing first principle calculations, Guo *et al.* established the suitability of a single transition metal atom dispersed g-C_3N_4 catalyst for ORR. The adsorption energy of the key intermediate OH (ΔE_{*OH}) and the d-band centres form the basis of predicting the overpotential for ORR. The study predicted that among the various TM/g-C_3N_4 catalyst, Pd/g-C_3N_4 exhibited a low overpotential value of 0.46 V qualifying it to be an effective substituent for the conventional Pt catalyst.[147]

N-doped porous carbon containing Fe atoms (Fe-g-C_3N_4/HPNCPs, 2.15 wt%) coordinated to C_3N_4 matrix was demonstrated to be an effective ORR electrocatalyst, with an $E_{1/2}$ of 0.902 V, outperforming the commercial Pt/C catalysts. The hierarchical structure characterised by a micro–mesoporous architecture enabled increased mass transport to the catalytically active single atomic Fe–N_2 sites favouring enhanced ORR activity with appreciable durability.[148]

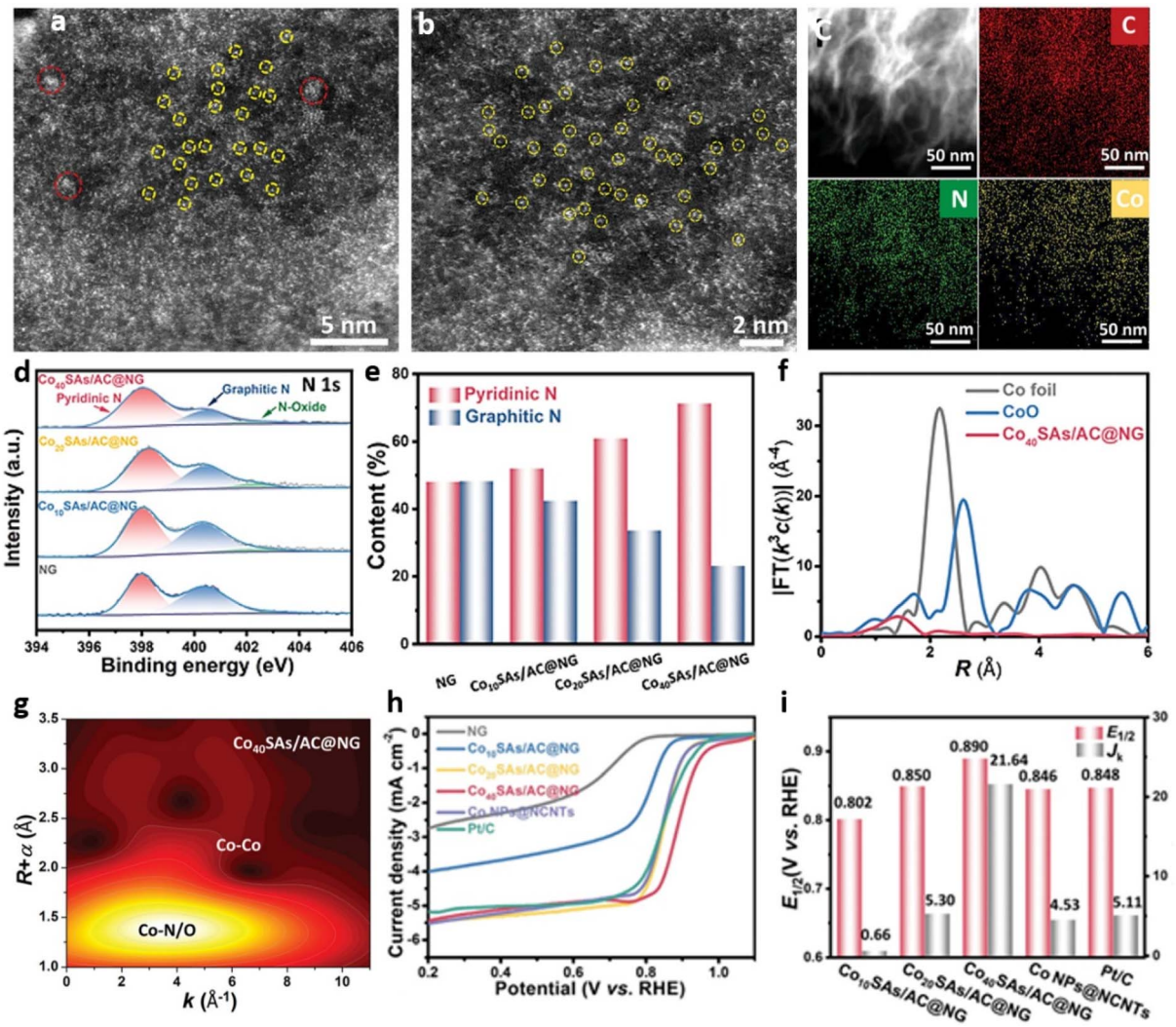

Fig. 33 (a and b) HAADF-STEM images of Co_{40}SAs/AC@NG catalyst (aberration-corrected), (c) EDS mappings of Co_{40}SAs/AC@NG by HAADF-STEM; yellow and red circles represent Co single atoms and Co clusters respectively, (d) XPS N 1s spectra of NG and CoSAs/AC@NG, (e) N content of NG and Co SAs/AC@NG, (f and g) EXAFS spectra and WT-EXAFS plots of Co_{40}SAs/AC@NG, (h and i) Comparison of RDE polarisation curves at a scan rate of 5 mV s at 1600 rpm, J_k values at 0.85 V & $E_{1/2}$ values of the samples for ORR activity in O_2-saturated 0.1 M KOH solution. Reproduced with permission from ref. 150. Copyright 2022 John Wiley and Sons.

Table 11 Summary of g-C_3N_4 SACs for electrocatalytic oxygen evolution reaction & oxygen reduction reaction (OER & ORR)

System	Single atom & loading	Synthesis method	OER & ORR activity (onset potential, $E_{1/2}$, current density, mass activity)	Coordination site or structure & oxidation state	Ref.
Ni–CN	Ni 2.4 at%	Template free direct synthesis	OER: onset potential 1.54 eV	Nitrogen	142
M-C_3N_4/CNT	M = Cr, Mn, Fe, Co, Ni, Cu, Zn; Co: 0.2 at%	Template free direct synthesis	Co–C_3N_4/CNT ORR: onset potential: 0.9 V, current density: 5 mA cm^{-2}, ORR: onset potential: 1.5 V, current density: 10 mA cm^{-2} at 1.6 V	Co–N_2, +2	143
Au_1N_x/C_3N_4	Au 0.7 wt%	Post synthesis-electrostatic adsorption	ORR: Mass activity of 9000 A g_{Au}^{-1} at $E_{1/2}$ of 0.76 V, OER: mass activity of 1500 A g_{Au}^{-1} at overpotential 0.45 V	Au_1N_x, +1	22
C-FeHZ8 @g-C_3N_4	Fe 3.17 wt%	g-C_3N_4 as a fugitive template	ORR: $E_{1/2}$: 0.18 V in acidic condition 0.845 V in alkaline condition	Fe–N_4, +2	144
NCM–CN–Fe	Fe	g-C_3N_4 as a fugitive template	ORR: Onset potential: 0.0 V current density −6.42 mA cm^{-2}	Fe–$N_{4.1}$	145
Co–O–C_3N_4@CS & Co–C_3N_4@CS	Co 0.13 & 0.09 wt%	Post synthesis	OER: Co–O–C_3N_4@CS: overpotential 0.23 V current density: 10 mA cm^{-2} Co–C_3N_4@CS: overpotential 0.47 V current density: 50 mA cm^{-2}	Co–O & Co–N	146
TM/g-C_3N_4	TM = Ti - Au	DFT study	Pd/g-C_3N_4 is predicted to exhibit good ORR activity with an overpotential of 0.46 V	—	147
Fe-g-C_3N_4/HPNCPs	Fe 2.15 wt%	g-C_3N_4 as a fugitive template	ORR: $E_{1/2:}$ 0.902 V	Fe–N_2, oxidation state in between 0 & +3	148
TM g^{-1}-CN	TM = Ti, V, Cr, Mn, Fe, Co, Ni	DFT study	Co_1/g-CN & Ni_1/g-CN SACs are predicted to be the most effective OER catalysts with overpotential values of 0.61 V and 0.40 V respectively	Nitrogen	137
TM/V_N-CN	TM = Ti to Au	DFT study	Rh/V_NCN is predicted to have optimal activity with overpotential values of 0.32 and 0.43 V for OER & ORR respectively	C/N	10
Fe/N/C	Fe 1.5 wt%	g-C_3N_4 as a fugitive template	ORR: onset potential: 0.972 V, $E_{1/2:}$ 0.89 V, mass specific activity: 9.103 mA mg^{-1} @ 0.9 V	Fe–N_4, +2	149
CoSAs/AC@NG	Co 14 wt%	g-C_3N_4 as a fugitive template	ORR: $E_{1/2}$: 0.890 V, kinetic current density (Jk):17.07 mA cm^{-2}, mass activity: 305 A g^{-1} at 0.85 V	Co–N_4, +2	150

The potential of Co_1/g-CN and Ni_1/g-CN SACs described earlier for overall water splitting, have been evaluated for OER. The theoretical calculations predicted that Co_1/g-CN and Ni_1/g-CN SACs can exhibit overpotential values of 0.61 V and 0.40 V respectively for OER reactions that are comparable with that of IrO_2 reference catalysts with 0.55 V overpotential value.[137]

By combining DFT with machine learning Guo *et al.* predicted the possibility of developing highly efficient OER and ORR bifunctional catalysts based on single atom transition metal (TM) dispersed over g-C_3N_4 (Fig. 32(a and b)). The defects induced by the nitrogen vacancies in g-C_3N_4 (VN–CN) facilitate a strong RMSI with TM single atoms providing stability for TM/VN-CN. Among various TMs, Rh/VN-CN indicated low overpotentials of 0.43 and 0.32 V for ORR and OER respectively (Fig. 32(c–h)).[10]

Peng *et al.* demonstrated the development of Fe, N co-doped carbon (Fe/N/C) using Fe coordinated g-C_3N_4 and glucose as precursors. The intense mixing of urea-derived g-C_3N_4, $FeCl_3 \cdot 6H_2O$ and glucose under ultrasonication resulted in the formation of Fe coordinated g-C_3N_4 matrix. The adsorbed glucose on hydrothermal treatment, formed linear and/or branchlike oligosaccharides. Carbonisation at 1100 °C resulted in the conversion of g-C_3N_4-coordinated Fe embedded in glucose-derived carbon to porous Fe/N/C. The pyridinic N atoms of heptazine rings (known as N pots) in the g-C_3N_4 matrix can prevent the aggregation of the metal species during high-temperature pyrolysis by realising coordination between lone pairs of electron and metal species. The negative adsorption energy values calculated *via* DFT studies for Fe^{3+} ion (−38.26 eV) and Fe atom (−3.54 eV) on the N pots further substantiated the role of g-C_3N_4 in realising atomic level dispersion of Fe on carbon matrix. Fe/N/C-575 A (Fe/N/C-575) sample after the ORR catalytic activation steps such as acid leaching and second annealing exhibited good ORR activity with large onset protectional ($E_{onset} = 0.972$ V) and half-wave potential ($E_{1/2} = 0.890$ V) with a mass specific activity (j_m) of 9.103 mA mg^{-1} at 0.9 V. The availability of a large number of Fe–N_4 active sites over the high surface area matrix, synergistic activity of Fe single atoms with N–C nanosheets, and the enhanced mass transfer due to high porosity collectively contributed towards the enhanced ORR performance of Fe/N/C-575-A catalyst.[149]

Xu *et al.* demonstrated a facile template strategy for the development of ORR electrocatalyst based on N-doped graphene containing up to 14.0 wt% of Co single atoms and atomic clusters. The catalyst CoSAs/AC@NG was obtained by the pyrolysis of dicyandiamide with the formation of layered g-C_3N_4 as the sacrificial template with abundant N anchoring sites to realise the single Co atom loading. The catalyst was synthesised by the low-temperature pyrolysis (550 °C) of a precursor mix of glucose, dicyandiamide (DCDA) and $CoCl_2 \cdot 6H_2O$ followed by a high-temperature annealing at 800 °C for the conversion of g-C_3N_4 to porous carbon. The numerous defective sites and high N content acted as the anchoring sites for Co single atoms and the transformation of intermediate products to conductive carbon led to the *in situ* formation of high-density cobalt single atoms in nitrogen-doped graphene (Co SAs/AC@NG). XANES analysis revealed that the valence state of cobalt is close to +2 as the Co K-edge absorption position of Co SAs/AC@NG varied with that of Co foil but was similar to that of CoO. The EXAFS spectral analysis of the catalyst confirmed Co–N(O) coordination through a major peak at ≈1.41 Å, and a weak peak at 2.22 Å, indicating the presence also of Co clusters. The EXAFS fittings suggested an average coordination number of 3.7 ± 0.3 for Co–N(O). It was inferred from the XPS and XAS analysis that the most dominant active sites in Co SAs/AC@NG are likely to be the Co–N_4 moiety (Fig. 33 (a–g)). Co_{40}SAs/AC@NG with $E_{1/2}$ of 0.890 V, kinetic current density (J_k) of 17.070 mA cm^{-2} and mass activity of 305 A g^{-1} at 0.85 V outperformed the commercial Pt/C (J_k of 4.845 and mass activity of 60.5 A g^{-1}) for ORR reaction (Fig. 33(h and i)). Additionally, Co_{40}SAs/AC@NG exhibited excellent performance in Zn–air battery as an air electrode material with a high-peak power density value of 221 mW cm^{-2} and with high cycling stability.[150]

Table 11 lists the OER and ORR applications of g-C_3N_4 based SACs.

6 Conclusion and future perspectives

Single atom catalysts have emerged as potential systems with attractive features for a multitude of applications. The use of g-C_3N_4 as an efficient matrix for the development of SACs has been hitherto established to a fair level of certainty. The ease of anchoring single atoms on the matrix through abundant nitrogen sites in g-C_3N_4 facilitated the development of a variety of SACs for applications in different domains of catalysis. Advanced analytical tools like EXAFS, XANES, aberration corrected HAADF-STEM and EELS are used to confirm the single atom formation with a positive (partial/full) oxidation state. Computational studies have also been employed to validate the geometrical and coordination structures as well as to elucidate and predict the catalytic mechanisms.

Conventional approaches of synthesising g-C_3N_4 based SACs like wet chemical reduction, high-temperature heat treatment of precursor mix under an inert atmosphere, and supramolecular self-assembly techniques are presumed to be advantageous over hardware intensive atomic layer deposition method (ALD). Even though precise control of single atom dispersion is possible in ALD, metal loading realisable is relatively low. The scale up possibilities in kilogram batches have been recently demonstrated in a multistep high temperature treatment under an inert atmosphere. Single atoms of 15 transition metals in ultra-high density have been developed on g-C_3N_4 support. The process is thus amenable for large-scale production in appreciable yields. Downsizing metal species to single atoms significantly improves metal utilisation efficiency imparting desirable catalytic properties. However, enhanced metal–support interaction, though beneficial for catalyst stability, often impedes catalytic activity due to unfavourable product desorption. A balance has to be thus established between catalyst stability and activity for which an in-depth analysis of the metal–support interaction and mechanistic reaction pathways are essential. Real-time analysis involving operando techniques has to be explored further for g-C_3N_4 based SACs.

The use of synchrotron based spectroscopic tools is an essential requirement to elucidate the metal oxidation state and

coordination structure in SACs. Apart from this catalyst characterisation, the study of the catalytic mechanism necessitates real-time analysis as mentioned before, the accessibility of which is scarce.

Of the reported systems thus far, g-C_3N_4 SACs are primarily based on single metal systems predominantly of precious metals. The techno-economic feasibility of such systems for large-scale applications is limited due to cost and availability. The shortcoming can presumably be circumvented by the use of dual or multiple metals as atomic dispersions over g-C_3N_4. This can be realised by substituting precious metals partly with non-precious ones to balance affordability with catalytic performance. This is particularly true for applications demanding multi-site synergism like CO_2 reduction and organic transformations. For example, in photocatalytic CO_2 reduction SAC with single sites normally facilitates the reduction of CO_2 to C_1 products like HCOOH, CO, CH_3OH, HCHO, CH_4, *etc.* The product selectivity mainly depends upon the stability of the intermediates formed during the multi-electron–proton transfer. SACs with multiple metal sites can offer better stability to the intermediates compared to single metal sites thereby promoting extended electron proton transfer as well as C–C coupling to produce higher hydrocarbons. Along with dual metal sites, it is also feasible to incorporate single atom alloy catalysts based on g-C_3N_4 for enhanced activity by tuning electron density distributions around the multi centers.

Researchers have already employed DFT calculations to prove the efficiency of g-C_3N_4 based SACs for electrocatalytic applications such as CO_2 reduction, N_2 reduction, *etc* but the experimental verification of the hypothesis is still required. The poor conductivity of g-C_3N_4 support may impede its electrocatalytic activity to a larger extent and it may be advantageous to develop hybrid matrices incorporating materials of high electrical conductivity and charge transfer capacity (graphene, N-doped carbon, *etc.*).

One area of high practical relevance for the use g-C_3N_4 based SACs is believed to be organic reaction catalysis as a majority of the industrially relevant reactions employ homogeneous catalysts for enhanced kinetics and high yield. Recovery of the catalyst, particularly of precious metal compositions is vital for recyclability and cost effectiveness. g-C_3N_4 SACs are affordable solutions to bridge this gap and are presumed to be of high practical viability even though most of the works reported still employ Pt, Pd, Au based SACs. However, the recent report on the large-scale synthesis of g-C_3N_4 Cu SAC and its demonstration for organic transformation opens up myriad possibilities for the industrial utilisation of SACs. Nevertheless, this would necessitate a thorough understanding of the underlying mechanisms leading to the regiospecificity and selectivity of products. This review comprehensively analysed the developments in g-C_3N_4 based SACs and overviewed the synthesis, characterisation, analysis and applications.

Conflicts of interest

There are no conflicts to declare.

Acknowledgements

One of the authors (SP) acknowledges University Grants Commission for research fellowship.

References

1 P. Suyana, P. Ganguly, B. N. Nair, S. C. Pillai and U. Hareesh, *Chem. Eng. J. Adv.*, 2021, **8**, 100148.
2 Z. Li, B. Li, Y. Hu, X. Liao, H. Yu and C. Yu, *Small Struct.*, 2022, **3**, 2200041.
3 B. Qiao, A. Wang, X. Yang, L. F. Allard, Z. Jiang, Y. Cui, J. Liu, J. Li and T. Zhang, *Nat. Chem.*, 2011, **3**, 634–641.
4 G. Vilé, D. Albani, M. Nachtegaal, Z. Chen, D. Dontsova, M. Antonietti, N. López and J. Pérez-Ramírez, *Angew. Chem., Int. Ed.*, 2015, **54**, 11265–11269.
5 G. Gao, Y. Jiao, E. R. Waclawik and A. Du, *J. Am. Chem. Soc.*, 2016, **138**, 6292–6297.
6 Z. Chen, S. Mitchell, E. Vorobyeva, R. K. Leary, R. Hauert, T. Furnival, Q. M. Ramasse, J. M. Thomas, P. A. Midgley, D. Dontsova and J. Pérez-Ramírez, *Adv. Funct. Mater.*, 2017, **27**, 1605785.
7 T. Tong, B. He, B. Zhu, B. Cheng and L. Zhang, *Appl. Surf. Sci.*, 2018, **459**, 385–392.
8 P. Zhou, X. Hou, Y. Chao, W. Yang, W. Zhang, Z. Mu, J. Lai, F. Lv, K. Yang, Y. Liu and S. Guo, *Chem. Sci.*, 2019, **10**, 5898–5905.
9 S. Ji, Y. Qu, T. Wang, Y. Chen, G. Wang, X. Li, J. Dong, Q. Chen, W. Zhang and Z. Zhang, *Angew. Chem., Int. Ed.*, 2020, **59**, 10651–10657.
10 H. Niu, X. Wan, X. Wang, C. Shao, J. Robertson, Z. Zhang and Y. Guo, *ACS Sustainable Chem. Eng.*, 2021, **9**, 3590–3599.
11 X. Hai, S. Xi, S. Mitchell, K. Harrath, H. Xu, D. F. Akl, D. Kong, J. Li, Z. Li and T. Sun, *Nat. Nanotechnol.*, 2022, **17**, 174–181.
12 R. Shibuya, T. Kondo and J. Nakamura, *Carbon-Based Metal-Free Catalysts: Design and Applications*, 2018, 1, pp. 227–249.
13 C. Gao, J. Low, R. Long, T. Kong, J. Zhu and Y. Xiong, *Chem. Rev.*, 2020, **120**, 12175–12216.
14 M. Kathiresan, in *Nanoscale Graphitic Carbon Nitride*, Elsevier, 2022, pp. 1–16.
15 S. Panneri, P. Ganguly, B. N. Nair, A. A. P. Mohamed, K. G. K. Warrier and U. N. S. Hareesh, *Environ. Sci. Pollut. Res.*, 2017, **24**, 8609–8618.
16 P. Chen, B. Lei, X. a. Dong, H. Wang, J. Sheng, W. Cui, J. Li, Y. Sun, Z. Wang and F. Dong, *ACS Nano*, 2020, **14**, 15841–15852.
17 Z. Chen, S. Pronkin, T.-P. Fellinger, K. Kailasam, G. Vilé, D. Albani, F. Krumeich, R. Leary, J. Barnard, J. M. Thomas and D. Dontsova, *ACS Nano*, 2016, **10**, 3166–3175.
18 Y. Li, B. Li, D. Zhang, L. Cheng and Q. Xiang, *ACS Nano*, 2020, **14**, 10552–10561.
19 W. Zhang, Y. Fu, Q. Peng, Q. Yao, X. Wang, A. Yu and Z. Chen, *Chem. Eng. J.*, 2020, **394**, 124822.

20 C. Chu, D. Huang, Q. Zhu, E. Stavitski, J. A. Spies, Z. Pan, J. Mao, H. L. Xin, C. A. Schmuttenmaer and S. Hu, *ACS Catal.*, 2018, **9**, 626–631.
21 P. Sharma, S. Kumar, O. Tomanec, M. Petr, J. Zhu Chen, J. T. Miller, R. S. Varma, M. B. Gawande and R. Zbořil, *Small*, 2021, **17**, 2006478.
22 L. Liu, H. Su, F. Tang, X. Zhao and Q. Liu, *Nano Energy*, 2018, **46**, 110–116.
23 H. Su, W. Che, F. Tang, W. Cheng, X. Zhao, H. Zhang and Q. Liu, *J. Phys. Chem. C*, 2018, **122**, 21108–21114.
24 Y. Cao, S. Chen, Q. Luo, H. Yan, Y. Lin, W. Liu, L. Cao, J. Lu, J. Yang and T. Yao, *Angew. Chem., Int. Ed.*, 2017, **56**, 12191–12196.
25 P. Zhou, F. Lv, N. Li, Y. Zhang, Z. Mu, Y. Tang, J. Lai, Y. Chao, M. Luo, F. Lin and S. Guo, *Nano Energy*, 2019, **56**, 127–137.
26 Z. Chen, Q. Zhang, W. Chen, J. Dong, H. Yao, X. Zhang, X. Tong, D. Wang, Q. Peng and C. Chen, *Adv. Mater.*, 2018, **30**, 1704720.
27 R. Zhang, P. Li, F. Wang, L. Ye, A. Gaur, Z. Huang, Z. Zhao, Y. Bai and Y. Zhou, *Appl. Catal., B*, 2019, **250**, 273–279.
28 D. Deng, X. Chen, L. Yu, X. Wu, Q. Liu, Y. Liu, H. Yang, H. Tian, Y. Hu and P. Du, *Sci. Adv.*, 2015, **1**, e1500462.
29 K. O'Connell and J. R. Regalbuto, *Catal. Lett.*, 2015, **145**, 777–783.
30 P. Suyana, P. Ganguly, B. N. Nair, A. P. Mohamed, K. Warrier and U. Hareesh, *Environ. Sci.: Nano*, 2017, **4**, 212–221.
31 M. Varela, A. Lupini, K. Van Benthem, A. Borisevich, M. Chisholm, N. Shibata, E. Abe and S. Pennycook, *Annu. Rev. Mater. Res.*, 2005, **35**, 539–569.
32 S. Pennycook, A. Lupini, M. Varela, A. Borisevich, Y. Peng, M. Oxley, K. V. Benthem and M. Chisholm, in *Scanning Microscopy for Nanotechnology*, Springer, 2006, pp. 152–191.
33 X. Xiao, L. Zhang, H. Meng, B. Jiang and H. Fu, *Sol. RRL*, 2021, **5**, 2000609.
34 R. Brydson and N. Hondow, *Aberration-Corrected Analytical Transmission Electron Microscopy*, 2011, pp. 163–210.
35 R. Brydson, *Electron Energy Loss Spectroscopy*, Garland Science, 2020.
36 T. Zhang, Z. Chen, A. G. Walsh, Y. Li and P. Zhang, *Adv. Mater.*, 2020, **32**, 2002910.
37 Y. Wang, J. Mao, X. Meng, L. Yu, D. Deng and X. Bao, *Chem. Rev.*, 2018, **119**, 1806–1854.
38 M. Kottwitz, Y. Li, H. Wang, A. I. Frenkel and R. G. Nuzzo, *Chem.: Methods*, 2021, **1**, 278–294.
39 B. Zhang, T. Fan, N. Xie, G. Nie and H. Zhang, *Adv. Sci.*, 2019, **6**, 1901787.
40 S. Qiao, Q. He, P. Zhang, Y. Zhou, S. Chen, L. Song and S. Wei, *J. Mater. Chem. A*, 2022, **10**, 5771–5791.
41 S. K. Dutta, S. K. Mehetor and N. Pradhan, *J. Phys. Chem. Lett.*, 2015, **6**, 936–944.
42 A. Kubacka, M. Fernandez-Garcia and G. Colon, *Chem. Rev.*, 2012, **112**, 1555–1614.
43 X.-S. Zhang, K. Tian, J.-Y. Hu and H. Jiang, *Chemosphere*, 2015, **141**, 127–133.
44 B. Zhu, L. Zhang, B. Cheng and J. Yu, *Appl. Catal., B*, 2018, **224**, 983–999.
45 Y. Wang, X. Wang and M. Antonietti, *Angew. Chem., Int. Ed.*, 2012, **51**, 68–89.
46 B. Xia, Y. Zhang, J. Ran, M. Jaroniec and S.-Z. Qiao, *ACS Cent. Sci.*, 2021, **7**, 39–54.
47 K. Li, B. Peng and T. Peng, *ACS Catal.*, 2016, **6**, 7485–7527.
48 R. Liu, Z. Chen, Y. Yao, Y. Li, W. A. Cheema, D. Wang and S. Zhu, *RSC Adv.*, 2020, **10**, 29408–29418.
49 W. Tu, Y. Zhou and Z. Zou, *Adv. Mater.*, 2014, **26**, 4607–4626.
50 M. Marszewski, S. Cao, J. Yu and M. Jaroniec, *Mater. Horiz.*, 2015, **2**, 261–278.
51 A. K. Singh, J. H. Montoya, J. M. Gregoire and K. A. Persson, *Nat. Commun.*, 2019, **10**, 1–9.
52 P. Huang, J. Huang, S. A. Pantovich, A. D. Carl, T. G. Fenton, C. A. Caputo, R. L. Grimm, A. I. Frenkel and G. Li, *J. Am. Chem. Soc.*, 2018, **140**, 16042–16047.
53 J. Wang, T. Heil, B. Zhu, C.-W. Tung, J. Yu, H. M. Chen, M. Antonietti and S. Cao, *ACS Nano*, 2020, **14**, 8584–8593.
54 L. Cheng, H. Yin, C. Cai, J. Fan and Q. Xiang, *Small*, 2020, **16**, 2002411.
55 Z. Zhao, W. Liu, Y. Shi, H. Zhang, X. Song, W. Shang and C. Hao, *Phys. Chem. Chem. Phys.*, 2021, **23**, 4690–4699.
56 B. Singh, V. Sharma, R. P. Gaikwad, P. Fornasiero, R. Zbořil and M. B. Gawande, *Small*, 2021, **17**, 2006473.
57 S. Wang, J. Zhang, B. Li, H. Sun and S. Wang, *Energy Fuels*, 2021, **35**, 6504–6526.
58 K. Villa, J. R. Galán-Mascarós, N. López and E. Palomares, *Sustainable Energy Fuels*, 2021, **5**, 4560–4569.
59 A. Mishra, A. Mehta, S. Basu, N. P. Shetti, K. R. Reddy and T. M. Aminabhavi, *Carbon*, 2019, **149**, 693–721.
60 A. Fujishima and K. Honda, *Nature*, 1972, **238**, 37–38.
61 X. Li, J. Yu, J. Low, Y. Fang, J. Xiao and X. Chen, *J. Mater. Chem. A*, 2015, **3**, 2485–2534.
62 A. Naseri, M. Samadi, A. Pourjavadi, A. Z. Moshfegh and S. Ramakrishna, *J. Mater. Chem. A*, 2017, **5**, 23406–23433.
63 S. Y. Tee, K. Y. Win, W. S. Teo, L. D. Koh, S. Liu, C. P. Teng and M. Y. Han, *Adv. Sci.*, 2017, **4**, 1600337.
64 X. Li, W. Bi, L. Zhang, S. Tao, W. Chu, Q. Zhang, Y. Luo, C. Wu and Y. Xie, *Adv. Mater.*, 2016, **28**, 2427–2431.
65 W. Liu, L. Cao, W. Cheng, Y. Cao, X. Liu, W. Zhang, X. Mou, L. Jin, X. Zheng, W. Che and S. Wei, *Angew. Chem.*, 2017, **129**, 9440–9445.
66 M. Ou, S. Wan, Q. Zhong, S. Zhang and Y. Wang, *Int. J. Hydrogen Energy*, 2017, **42**, 27043–27054.
67 W. Zhang, Q. Peng, L. Shi, Q. Yao, X. Wang, A. Yu, Z. Chen and Y. Fu, *Small*, 2019, **15**, 1905166.
68 Z. Zeng, Y. Su, X. Quan, W. Choi, G. Zhang, N. Liu, B. Kim, S. Chen, H. Yu and S. Zhang, *Nano Energy*, 2020, **69**, 104409.
69 G. Wang, T. Zhang, W. Yu, R. Si, Y. Liu and Z. Zhao, *ACS Catal.*, 2020, **10**, 5715–5722.
70 M. Ren, X. Zhang, Y. Liu, G. Yang, L. Qin, J. Meng, Y. Guo and Y. Yang, *ACS Catal.*, 2022, **12**, 5077–5093.
71 B.-B. Xu, X.-B. Fu, X.-M. You, E. Zhao, F.-F. Li, Z. Chen, Y.-X. Li, X. L. Wang and Y.-F. Yao, *ACS Catal.*, 2022, **12**, 6958–6967.

72 R. Shi, Y. Zhao, G. I. Waterhouse, S. Zhang and T. Zhang, *ACS Catal.*, 2019, **9**, 9739–9750.
73 S. Hu, X. Qu, J. Bai, P. Li, Q. Li, F. Wang and L. Song, *ACS Sustainable Chem. Eng.*, 2017, **5**, 6863–6872.
74 C. Ling, X. Niu, Q. Li, A. Du and J. Wang, *J. Am. Chem. Soc.*, 2018, **140**, 14161–14168.
75 X.-W. Guo, S.-M. Chen, H.-J. Wang, Z.-M. Zhang, H. Lin, L. Song and T.-B. Lu, *J. Mater. Chem. A*, 2019, **7**, 19831–19837.
76 L. Li, Y. Yu, S. Lin, W. Chu, D. Sun, Q. Su, S. Ma, G. Du and B. Xu, *Catal. Commun.*, 2021, **153**, 106294.
77 S. Dong, J. Feng, M. Fan, Y. Pi, L. Hu, X. Han, M. Liu, J. Sun and J. Sun, *RSC Adv.*, 2015, **5**, 14610–14630.
78 D. S. Bhatkhande, V. G. Pangarkar and A. A. C. M. Beenackers, *J. Chem. Technol. Biotechnol.*, 2002, **77**, 102–116.
79 M. M. Khan, D. Pradhan and Y. Sohn, *Nanocomposites for Visible Light-Induced Photocatalysis*, Springer, 2017.
80 D. Chatterjee and S. Dasgupta, *J. Photochem. Photobiol., C*, 2005, **6**, 186–205.
81 M. A. Fox and M. T. Dulay, *Chem. Rev.*, 1993, **93**, 341–357.
82 Y. Wang, X. Zhao, D. Cao, Y. Wang and Y. Zhu, *Appl. Catal., B*, 2017, **211**, 79–88.
83 F. Wang, Y. Wang, Y. Li, X. Cui, Q. Zhang, Z. Xie, H. Liu, Y. Feng, W. Lv and G. Liu, *Dalton Trans.*, 2018, **47**, 6924–6933.
84 S. An, G. Zhang, T. Wang, W. Zhang, K. Li, C. Song, J. T. Miller, S. Miao, J. Wang and X. Guo, *ACS Nano*, 2018, **12**, 9441–9450.
85 Z. Zhao, W. Zhang, W. Liu, Y. Li, J. Ye, J. Liang and M. Tong, *Sci. Total Environ.*, 2020, **742**, 140642.
86 L. Zhang, J. Zhang, M. Qi, X. Guo and X. Feng, *Energy Fuels*, 2020, **34**, 12792–12799.
87 Y. Yang, G. Zeng, D. Huang, C. Zhang, D. He, C. Zhou, W. Wang, W. Xiong, B. Song and H. Yi, *Small*, 2020, **16**, 2001634.
88 G. Vilé, P. Sharma, M. Nachtegaal, F. Tollini, D. Moscatelli, A. Sroka-Bartnicka, O. Tomanec, M. Petr, J. Filip, I. S. Pieta and M. B. Gawande, *Sol. RRL*, 2021, **5**, 2100176.
89 F. Chen, X. L. Wu, C. Shi, H. Lin, J. Chen, Y. Shi, S. Wang and X. Duan, *Adv. Funct. Mater.*, 2021, **31**, 2007877.
90 G. Liu, Y. Huang, H. Lv, H. Wang, Y. Zeng, M. Yuan, Q. Meng and C. Wang, *Appl. Catal., B*, 2021, **284**, 119683.
91 L. Wang, R. Tang, A. Kheradmand, Y. Jiang, H. Wang, W. Yang, Z. Chen, X. Zhong, S. P. Ringer and X. Liao, *Appl. Catal., B*, 2021, **284**, 119759.
92 K. P. Bryliakov, *Chem. Rev.*, 2017, **117**, 11406–11459.
93 H. Hou, X. Zeng and X. Zhang, *Angew. Chem., Int. Ed.*, 2020, **59**, 17356–17376.
94 C. Dong, Y. Yang, X. Hu, Y. Cho, G. Jang, Y. Ao, L. Wang, J. Shen, J. H. Park and K. Zhang, *Nat. Commun.*, 2022, **13**, 1–11.
95 Z. P. Ifkovits, J. M. Evans, M. C. Meier, K. M. Papadantonakis and N. S. Lewis, *Energy Environ. Sci.*, 2021, **14**, 4740–4759.
96 C. Wang, X. Zhang and Y. Liu, *Appl. Surf. Sci.*, 2015, **358**, 28–45.
97 J. Liu, Y. Zou, B. Jin, K. Zhang and J. H. Park, *ACS Energy Lett.*, 2019, **4**, 3018–3027.
98 X. Zeng, Y. Liu, X. Hu and X. Zhang, *Green Chem.*, 2021, **23**, 1466–1494.
99 Z. Chen, D. Yao, C. Chu and S. Mao, *Chem. Eng. J.*, 2022, 138489.
100 Z. Teng, Q. Zhang, H. Yang, K. Kato, W. Yang, Y.-R. Lu, S. Liu, C. Wang, A. Yamakata and C. Su, *Nat. Catal.*, 2021, **4**, 374–384.
101 Z. Teng, W. Cai, W. Sim, Q. Zhang, C. Wang, C. Su and T. Ohno, *Appl. Catal., B*, 2021, **282**, 119589.
102 H. Arnold, F. Dobert, J. Gaube, G. Ertl, H. Knozinger and J. Weitkempl, *Handbook of heterogeneous catalysis*, ed. G. Ertl, H. Knoezinger and J. Weitkamp, 2008, pp. 2165–2186.
103 J. C. Védrine, *Catalysts*, 2017, **7**, 341.
104 X. Liu, L. He, Y.-M. Liu and Y. Cao, *Acc. Chem. Res.*, 2014, **47**, 793–804.
105 F. Zhang, Y. Zhu, Q. Lin, L. Zhang, X. Zhang and H. Wang, *Energy Environ. Sci.*, 2021, **14**, 2954–3009.
106 C. Bolm and M. Beller, *Transition Metals for Organic Synthesis*, Wiley-VCH, Weinheim, 2004.
107 Y. Chen, S. Ji, C. Chen, Q. Peng, D. Wang and Y. Li, *Joule*, 2018, **2**, 1242–1264.
108 H. Zhang, G. Liu, L. Shi and J. Ye, *Adv. Energy Mater.*, 2018, **8**, 1701343.
109 L. Liu and A. Corma, *Chem. Rev.*, 2018, **118**, 4981–5079.
110 J. Li, M. F. Stephanopoulos and Y. Xia, *Chem. Rev.*, 2020, **120**, 11699–11702.
111 Z. Chen, E. Vorobyeva, S. Mitchell, E. Fako, M. A. Ortuño, N. López, S. M. Collins, P. A. Midgley, S. Richard and G. Vilé, *Nat. Nanotechnol.*, 2018, **13**, 702–707.
112 P. Yang, S. Zuo, F. Zhang, B. Yu, S. Guo, X. Yu, Y. Zhao, J. Zhang and Z. Liu, *Ind. Eng. Chem. Res.*, 2020, **59**, 7327–7335.
113 F. Hu, L. Leng, M. Zhang, W. Chen, Y. Yu, J. Wang, J. H. Horton and Z. Li, *ACS Appl. Mater. Interfaces*, 2020, **12**, 54146–54154.
114 Z. Chen, Y. Chen, S. Chao, X. Dong, W. Chen, J. Luo, C. Liu, D. Wang, C. Chen and W. Li, *ACS Catal.*, 2020, **10**, 1865–1870.
115 N. Kong, X. Fan, F. Liu, L. Wang, H. Lin, Y. Li and S.-T. Lee, *ACS Nano*, 2020, **14**, 5772–5779.
116 Y. Xiong, W. Sun, Y. Han, P. Xin, X. Zheng, W. Yan, J. Dong, J. Zhang, D. Wang and Y. Li, *Nano Res.*, 2021, **14**, 2418–2423.
117 G. Vilé, G. Di Liberto, S. Tosoni, A. Sivo, V. Ruta, M. Nachtegaal, A. H. Clark, S. Agnoli, Y. Zou and A. Savateev, *ACS Catal.*, 2022, **12**, 2947–2958.
118 K. Eid, M. H. Sliem, M. Al-Ejji, A. M. Abdullah, M. Harfouche and R. S. Varma, *ACS Appl. Mater. Interfaces*, 2022, **14**, 40749–40760.
119 Y. Zhang, X. Cao and Z. Cao, *ACS Appl. Mater. Interfaces*, 2022, **14**, 35844–35853.
120 H. Zhang, W. Cheng, D. Luan and X. W. Lou, *Angew. Chem., Int. Ed.*, 2021, **60**, 13177–13196.
121 H. Hu, J. Wang, P. Tao, C. Song, W. Shang, T. Deng and J. Wu, *J. Mater. Chem. A*, 2022, **10**, 5835–5849.

122 W. Zhang, Y. Hu, L. Ma, G. Zhu, Y. Wang, X. Xue, R. Chen, S. Yang and Z. Jin, *Adv. Sci.*, 2018, **5**, 1700275.
123 J. Feng, H. Gao, L. Zheng, Z. Chen, S. Zeng, C. Jiang, H. Dong, L. Liu, S. Zhang and X. Zhang, *Nat. Commun.*, 2020, **11**, 1–8.
124 S. Fu, X. Liu, J. Ran, Y. Jiao and S.-Z. Qiao, *Appl. Surf. Sci.*, 2021, **540**, 148293.
125 C. Cometto, A. Ugolotti, E. Grazietti, A. Moretto, G. Bottaro, L. Armelao, C. Di Valentin, L. Calvillo and G. Granozzi, *npj 2D Mater. Appl.*, 2021, **5**, 63.
126 N. Zhang, M. I. Hussain, M. Xia and C. Ge, *Nano*, 2021, **16**, 2150016.
127 X. Wen and J. Guan, *Nanoscale*, 2020, **12**, 8065–8094.
128 G. F. Chen, S. Ren, L. Zhang, H. Cheng, Y. Luo, K. Zhu, L. X. Ding and H. Wang, *Small Methods*, 2019, **3**, 1800337.
129 X. Yan, D. Liu, H. Cao, F. Hou, J. Liang and S. X. Dou, *Small Methods*, 2019, **3**, 1800501.
130 X. Cui, C. Tang and Q. Zhang, *Adv. Energy Mater.*, 2018, **8**, 1800369.
131 W. Song, K. Xie, J. Wang, Y. Guo, C. He and L. Fu, *Phys. Chem. Chem. Phys.*, 2021, **23**, 10418–10428.
132 Z. Chen, J. Zhao, C. R. Cabrera and Z. Chen, *Small Methods*, 2019, **3**, 1800368.
133 C. Ren, Q. Jiang, W. Lin, Y. Zhang, S. Huang and K. Ding, *ACS Appl. Nano Mater.*, 2020, **3**, 5149–5159.
134 S. Agarwal, R. Kumar, R. Arya and A. K. Singh, *J. Phys. Chem. C*, 2021, **125**, 12585–12593.
135 X. Wang, W. Wang, M. Qiao, G. Wu, W. Chen, T. Yuan, Q. Xu, M. Chen, Y. Zhang and X. Wang, *Sci. Bull.*, 2018, **63**, 1246–1253.
136 H. Liu, X. Peng and X. Liu, *ChemElectroChem*, 2018, **5**, 2963–2974.
137 X. Lv, W. Wei, H. Wang, B. Huang and Y. Dai, *Appl. Catal., B*, 2020, **264**, 118521.
138 X. Liu, Y. Deng, L. Zheng, M. R. Kesama, C. Tang and Y. Zhu, *ACS Catal.*, 2022, **12**, 5517–5526.
139 M. Tahir, L. Pan, F. Idrees, X. Zhang, L. Wang, J.-J. Zou and Z. L. Wang, *Nano Energy*, 2017, **37**, 136–157.
140 T. He, S. K. Matta, G. Will and A. Du, *Small Methods*, 2019, **3**, 1800419.
141 Z. Xue, X. Zhang, J. Qin and R. Liu, *J. Energy Chem.*, 2021, **55**, 437–443.
142 S. Ohn, S. Y. Kim, S. K. Mun, J. Oh, Y. J. Sa, S. Park, S. H. Joo, S. J. Kwon and S. Park, *Carbon*, 2017, **124**, 180–187.
143 Y. Zheng, Y. Jiao, Y. Zhu, Q. Cai, A. Vasileff, L. H. Li, Y. Han, Y. Chen and S.-Z. Qiao, *J. Am. Chem. Soc.*, 2017, **139**, 3336–3339.
144 Y. Deng, B. Chi, X. Tian, Z. Cui, E. Liu, Q. Jia, W. Fan, G. Wang, D. Dang, M. Li and X. Sun, *J. Mater. Chem. A*, 2019, **7**, 5020–5030.
145 C. Wang, H. Zhao, J. Wang, Z. Zhao, M. Cheng, X. Duan, Q. Zhang, J. Wang and J. Wang, *J. Mater. Chem. A*, 2019, **7**, 1451–1458.
146 Q. Song, J. Li, L. Wang, L. Pang and H. Liu, *Inorg. Chem.*, 2019, **58**, 10802–10811.
147 H. Niu, X. Wang, C. Shao, Y. Liu, Z. Zhang and Y. Guo, *J. Mater. Chem. A*, 2020, **8**, 6555–6563.
148 T. Sun, P. Zhang, W. Chen, K. Wang, X. Fu, T. Zheng and J. Jiang, *Chem. Commun.*, 2020, **56**, 798–801.
149 X.-B. Ding, L. Zhang, Y.-H. Qin, L. Yang, C. Wang and C. Peng, *Chem. Commun.*, 2021, **57**, 6935–6938.
150 M. Zhang, H. Li, J. Chen, F. X. Ma, L. Zhen, Z. Wen and C. Y. Xu, *Adv. Funct. Mater.*, 2023, **33**, 2209726.